Year XXXIII Nº 46 June 2025

UNDERGROUND MINING ENGINEERING

Podzemni radovi

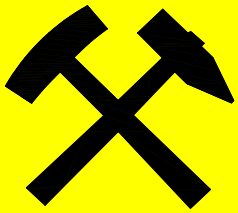

University of Belgrade – Faculty of Mining and Geology

UDK 62

eISSN 2560-3337

UNDERGROUND MINING ENGINEERING

PODZEMNI

RADOVI N°46

http://ume.rgf.bg.ac.rs
e-mail: editor.ume@rgf.bg.ac.rs

Belgrade, June 2025.

UNDERGROUND MINING ENGINEERING 46 (2025) UDK 62
UNIVERSITY OF BELGRADE - FACULTY OF MINING AND GEOLOGY eISSN 2560-3337

UNDERGROUND MINING ENGINEERING - PODZEMNI RADOVI

Publishing supported by: University of Belgrade – Faculty of Mining and Geology, Mining Section

Publisher: University of Belgrade - Faculty of Mining and Geology

For publisher: D.Sc. Aleksandar Cvjetić, Dean of Faculty of Mining and Geology

Available online: https://ume.rgf.bg.ac.rs/index.php/ume

The first issue of the journal "Podzemni radovi" (Underground Mining Engineering) was published back in 1982. Its founders were: Business Association Rudis - Trbovlje and the Faculty of Mining and Geology Belgrade. After publishing only four issues, however, the publication of the journal ceased in the same year.

Ten years later, in 1992, on the initiative of the Chair for the Construction of Underground Roadways, the Faculty of mining and Geology as the publisher, has launched journal "Podzemni radovi". The initial concept of the journal was, primarily, to enable that experts in the field of underground works and disciplines directly connected with those activities get information and present their experiences and suggestions for solution of various problems in this scientific field.

Development of science and technique requires even larger multi-disciplinarity of underground works, but also of the entire mining as industrial sector as well. This has also determined the change in editorial policy of the journal. Today, papers in all fields of mining are published in the "Underground Mining Engineering", fields that are not so strictly in connection with underground works, such as: surface mining, mine surveying, mineral processing, mining machinery, environmental protection and safety at work, oil and gas engineering and many others.

Extended themes covered by this journal have resulted in higher quality of published papers, which have considerably added to the mining theory and practice in Serbia, and which were very useful reading material for technical and scientific community.

A wish of editors is to extend themes being published in the "Underground Mining Engineering" even more and to include papers in the field of geology and other geo-sciences, but also in the field of other scientific and technical disciplines having direct or indirect application in mining.

The journal "Underground Mining Engineering" is published twice a year, in English language. Papers are subject to review.

This information represents the invitation for cooperation to all of those who have the need to publish their scientific, technical or research results in the field of mining, but also in the field of geology and other related scientific and technical disciplines having their application in mining.

Editors

TABLE OF CONTENTS

UNDERGROUND MINING ENGINEERING 46 (2025) 1-15 UDK 62
UNIVERSITY OF BELGRADE - FACULTY OF MINING AND GEOLOGY EISSN 2560-3337

Original scientific paper

INTERPRETATION OF TRANSIENT CAVING DUST PATTERNS DURING SEQUENTIAL CAVING OPERATION IN LTCC FACE

Krishna Tanguturi[1], Rao Balusu[1], Johnny Qin[1], Bharath Belle[234]

Received: May 30, 2024 **Accepted:** June 10, 2025

Abstract: Longwall top coal caving (LTCC) is a mining technology introduced for enhancing the coal production rate by using the top coal caving (TCC) operations for thick seams. LTCC mine increases coal production rates but at the expense of high dust exposure and may create hazardous conditions for mine operators. It is vital for the introduction of advanced dust control technologies as well as strategies during LTCC operations for dust reduction. For developing LTCC dust control strategies, fundamental understanding of transient caving dust flow pattern across the face is necessary. Note, region above the rear armored face conveyor (AFC) is difficult to access for carrying out field measurements and hence numerical approach is the only option left for determining the dust and flow fields. In this paper, an attempt is made to predict respirable dust flow patterns during sequential caving operations in the mid face region using computational fluid dynamics (CFD) techniques. Results predicted caving dust sources entering the downstream chock and dispersing into the walkway region within 5 seconds. Respirable dust in the first downstream walkway remains below 2mg/m³ whereas in the second downstream chock in the sequence is above 2.5mg/m³. Interpreting the results, it can be inferred that caving dust controls using water sprays need to be activated in not only in the caving chock but also in the immediate downstream chock from the start of the sequence caving for preventing the migration respirable dust into the walkway regions of the downstream chocks until the completion of the sequential caving operation in all the five chocks.

Keywords: Respirable dust; top coal caving; sequential caving

[1] CSIRO Mineral Resources BU, Mine Safety and Environment Group, QCAT, QLD, Australia, 4069
[2] School of Mechanical and Mining Engineering, UQ, Australia, 4072; Adjunct Associate Professor
[3] University of Pretoria, Hatfield, Pretoria 0002, South Africa
[4] SIMTARS Australia

E-mails: krishna.tanguturi@csiro.au, ORCID: 0000-0003-4789-3259; rao.balusu@csiro.au, ORCID: 0000-0001-5495-8220; johnny.qin@csiro.au, ORCID: 0000-0001-5495-8220
bharath.belle@simtars.com.au, ORCID: 0000-0002-2467-948X

1 INTRODUCTION

LTCC method is based on the "Soutirage" longwall caving method originally developed in the French underground coal industry. The essential features of the soutirage method are that a conventional height longwall face operates at the base of a thick coal seam. The top coal is mined by allowing it to cave above and immediately behind the rear chock canopy. LTCC chocks are specially designed with various types of hatches or draw point in each, through which the caved coal can pass. Different soutirage methods either passed the caved coal directly onto a second conveyor located within the rear of the chocks, or via a chute between the legs, through to the front AFC (Quang, 2010). LTCC method offers a viable means of extracting up to 75% to 80% of seams in the 5m to 9m thickness range. This method has improved control over spontaneous combustion in thick seams, through removal of most of the top coal from the face (Cai, 2004).

In 2001, CSIRO and University of New South Whales carried out a pre-feasibility study of introduction of LTCC technology for Australian underground coal mines. As part of the study, a risk assessment is carried out on the application of LTCC in Australian condition. In fact, LTCC is viewed to have many advantages compared to high reach single pass longwalls. Some of the points that came out of the risk assessment are poor ventilation for rear AFC resulting in an accumulation of dust and gases, the rear AFC drives exposed to gas made from caving coal with limited ventilation and large dust exposure in the face due to additional caving dust source. CSIRO at QCAT carried out extensive studies on gas modelling in LTCC face and investigated the effects gas distribution in LTCC mines. Various gas control options are investigated using numerical techniques that would successfully eliminate or minimize the methane gas concentrations at the rear AFC regions (Greg, 2007). The modifications and improvements to the LTCC equipment are being carried out and will no doubt result in an industry-leading extraction system capable of maximizing the value of the operation (Greg, 2007). Understanding dust and airflow patterns is crucial for developing effective dust control measures, particularly for managing dust generated by caving at the LTCC face. In recent years, many numerical studies were carried out on dust monitoring and dust dispersion in longwall panels (Ren, 2023), and in gate road development (CRC Press, 2023). Studies focusing exclusively on dust dispersion in LTCC faces are scarce and have yet to be thoroughly investigated, both in the field and through numerical simulations.

Dusts are small solid particles, conventionally taken as those particles below 75μm in diameter, which settle out under their own weight and may remain suspended for some time. Dust particles are frequently found with dimensions considerably below 1 μm and, their settlement due to gravity is negligible. The terminal velocity of a 1 μm particle is about 0.03mm/sec, so movement of the air is more important than sedimentation through it (WHO, 1999). The experimental studies in mines and laboratories indicate that only a very small portion of the dust that is generated gets airborne, which are approximately

0.001 to 0.08 percentages in the respirable dust size range, and 0.01 to 0.12 percentages for the inhalable dust size range (WHO, 1999). The primary dust sources in LTCC face are air intake, stage loader/crusher, front AFC and rear AFC transfer points, shearer, chocks advancement and caving. Of these, three major dust sources are shearer, chocks advancement and caving operations. With the introduction of top coal caving in the longwall face, the numbers of dust sources shoot up to seven. These primary dust source locations along a LTCC face have been accounted for dust generation, as shown in Figure 1.

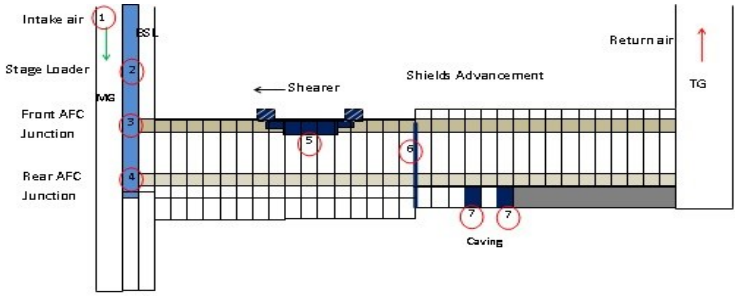

Figure 1 LTCC dust sources at various locations across the face

2 GEOMETRY - MODEL DEVELOPMENT

ANSYS design modeler is used for developing the replication of the LTCC mine. Figure 2 presents an isometric view of the CFD model showing the MG side equipment i.e., beam stage loader (BSL), MG transitional chocks and the main chocks in the LTCC face. In this model, the LTCC face width is 320m, cutting height is 3.6m and the roadway width is 5.6m. For accumulating the respirable dust dispersion into the LTCC goaf, a goaf length of 100m was used in the CFD model.

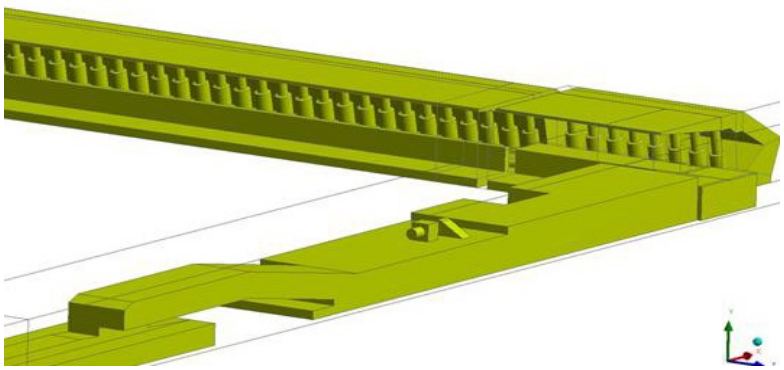

Figure 2 CFD model of the LTCC face

On the MG side of the longwall panel, key components include the BSL, front and rear AFC transfer points, and their corresponding driver units integrated into the first two sets of MG transition chocks. The main chocks (#145) span most of the LTCC face, succeeded by three TG side transitional chocks. The initial two chocks (1-2) primarily reside in the goaf region, housing the rear AFC junction and drive unit. Subsequently, chocks 3-5 of the second MG transition set accommodate the front AFC and its drive unit. The sequence continues with normal chocks 6-149, extending through majority of face region, as illustrated in the cross-sectional view in Figure 3.

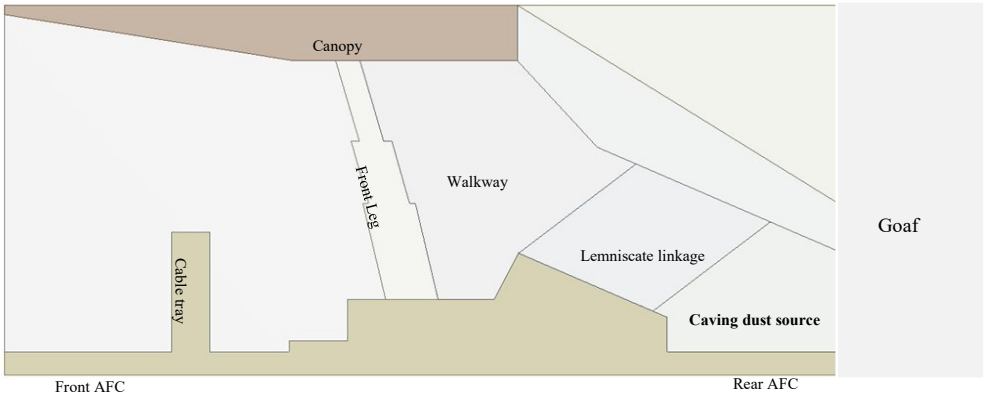

Figure 3 Schematic representation of cross section of the face with the caving dust source

3 CFD - MODEL SETUP

At the MG inlet, velocity inlet boundary condition is specified which corresponds to volume flow rate of 60 m^3/s, while a zero-pressure boundary condition is applied at the tailgate return. Turbulent airflow modelling across the LTCC face is carried out using k-epsilon model. The primary focus of the simulation is to emulate the dispersion patterns of dust particles originating from the caving process. In Ansys Fluent, Discrete Element Model (DEM) (ANSYS, 2023) is activated and respirable particle size distribution ranging between 0.1 to 10µm, with a mean particle size diameter of 5µm is specified. Various forces acting on the particle, i.e., drag force, lift force, and virtual mass force are incorporated in the discrete model. In this numerical model, specifying dust sources is a challenging task, several numerical trials are carried out before the caving dust source is fixed. An approximate dust emission during top coal caving operation is assumed amounting to be 500 mg/s, with a specific allocation of 150 mg/s attributed to respirable dust, a quantity maintained at the caving source continuously for a duration of 10 seconds. At this stage of the project, it is very difficult to quantify the exact caving dust source. It is to be noted here that the caving dust quantity used in the model is just an

assumption and assumes that caving dust could be one third of the shearer dust sources generated during shearer cutting operations.

4 CAVING SEQUENCE

A dynamic modeling approach is employed to simulate the transient flow of dust particles during the top coal caving process in the LTCC face. The specific caving sequence adopted in the LTCC mine is visually represented in Figure 4. The caving operation unfolds successively at five chocks, with each chock facilitating caving for a duration of 10 seconds. The initiation of caving at each chock occurs 5 seconds after the onset of the sequence. Notably, a 5-second overlap is observed, during which caving concurrently takes place at two consecutive chocks. The overall sequence of caving operations across all five chocks extends for a total duration of 30 seconds.

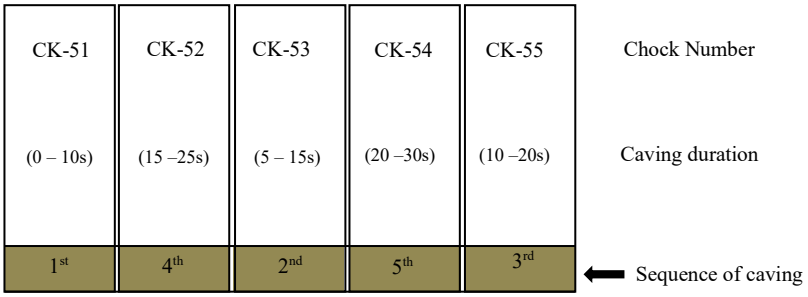

Figure 4 LTCC sequence from chock CK#51 to chock CK#55

5 MODEL VALIDATION

Air velocities and dust profile surveys are carried out using real time airflow and dust readings during normal production conditions at various locations along the face line using thermo scientific personal dust monitor 3700 (PDM 3700), vane anemometer, kestrel 1000 intrinsically air velocity safe meters and gravimetric personal dust samplers. The dust and ventilation data are used as inputs to validate the modelling results.

Figure 5 shows the snapshot of the field measurements containing air velocities, respirable dust and the location of the shearer at the time of measurement.

Location	Sample Point	Date & Time	Air Velocity @Sample Points (m/s)	PDM #1996 @Sample Points (mg/m³)	PDM #0877 @MG Chock 1-2 (mg/m³)	Shearer Position (Chock No.)	Comments
5m up stream of MG Corner (Shearer at mid-face area)	1	23/07/2019 13:10	3.50	0.87	0.98	40	Points 1 to 3 were taken on the top of BSL structure; Point 4 was taken at mid height of the side passage way (about 1-1.2m wide)
	2	23/07/2019 13:12	3.84	0.76	0.94	66	
	3	23/07/2019 13:14	4.24	0.65	0.88	85	
	4	23/07/2019 13:16	3.60	0.57	0.80	93	
10m inbye of MG (Chock #7) 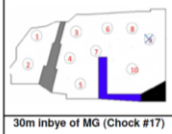	8	23/07/2019 13:19	2.72	0.44	0.64	105	PDM 591 (#0877) fixed at MG Chock #2; Point #9 can't be reached; LW face lost power @13:28; Power back on 13:40
	10	23/07/2019 13:21	4.08	0.32	0.59	117	
	6	23/07/2019 13:23	2.32	0.38	0.48	123	
	7	23/07/2019 13:25	3.35	0.43	0.38	129	
	3	23/07/2019 13:27	4.21	0.48	0.33	134	
	4	23/07/2019 13:28	3.30	0.48	0.32	137	
	5	23/07/2019 13:43	3.14	0.61	0.43	137	
	1	23/07/2019 13:44	1.65	0.49	0.45	137	
	2	23/07/2019 13:45	1.79	0.33	0.46	137	
30m inbye of MG (Chock #17) 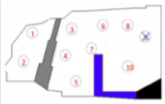	8	23/07/2019 13:48	4.80	0.67	0.52	143	Chock #12 Spray on AFC; Chock #14 Spray from Chock Top to AFC; there are a number of this type of set up along the LW face.
	10	23/07/2019 13:50	4.00	0.78	0.47	144	
	6	23/07/2019 13:52	0.84	0.94	0.43	140	
	7	23/07/2019 13:54	3.70	0.90	0.41	128	
	3	23/07/2019 13:56	3.05	0.77	0.46	127	
	4	23/07/2019 13:58	3.36	0.63	0.48	127	
	5	23/07/2019 13:59	3.48	0.54	0.49	127	
	1	23/07/2019 14:00	1.16	0.47	0.49	127	
	2	23/07/2019 14:02	2.33	0.40	0.49	127	

Figure 5 A Snapshot of field measurements

Figure 6 shows a comparison of field measurements and simulated results at 17th chock, i.e., at approximately 30m from the MG corner. Simulated respirable dust are around 0.4 – 0.9 mg/m³ at this location, which are in close agreement with the field measurements. In walkway, the respirable dust is around 0.7 – 0.9 mg/m³. Both CFD simulation results and the field measured data are in close agreement in various regions of the longwall face at this location.

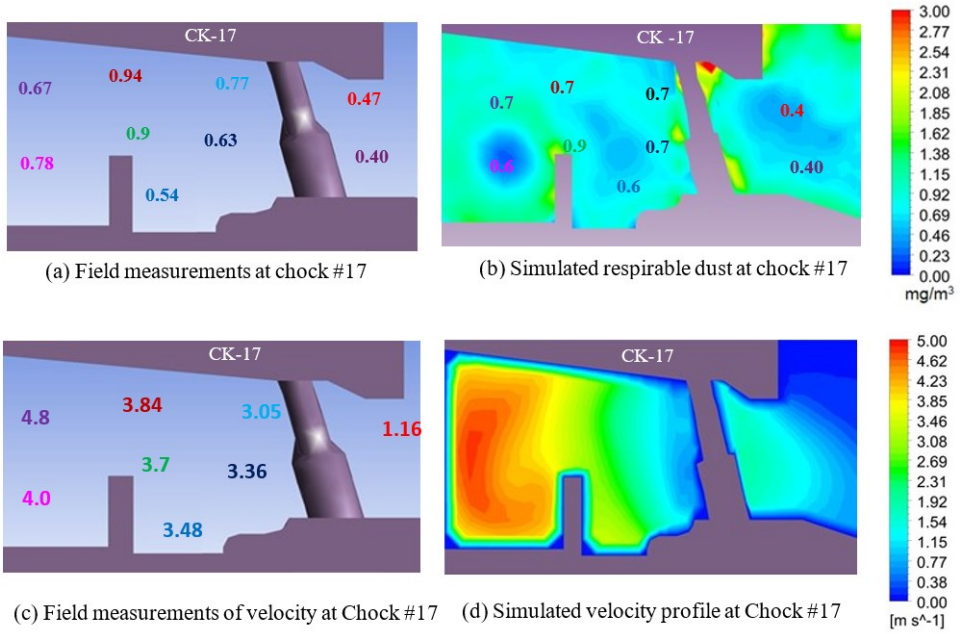

(a) Field measurements at chock #17 (b) Simulated respirable dust at chock #17

(c) Field measurements of velocity at Chock #17 (d) Simulated velocity profile at Chock #17

Figure 6 Field measurements and simulated dust distributions at chock #17

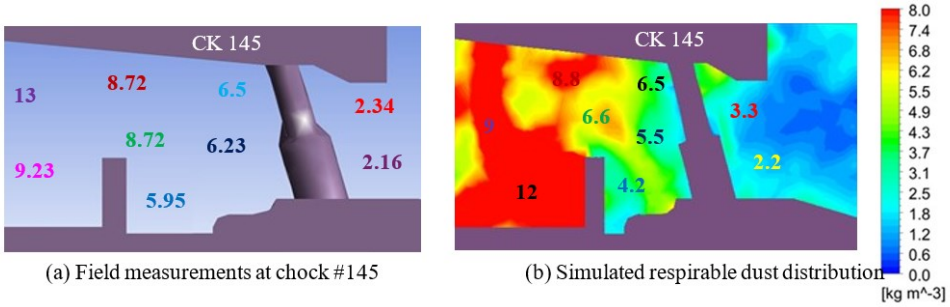

(a) Field measurements at chock #145 (b) Simulated respirable dust distribution

Figure 7 Field measurements and simulated dust distributions at chock #145

Figure 7 illustrates a comparison between field measurements and simulation results in chock145 located at a position 20m from the TG corner. In Figure 7 (a), field measurements reveal elevated respirable dust ranging from 6.0 to 13.0 mg/m³. In the walkway region, respirable dust concentrations hover around 6.0 – 9.0 mg/m³. Concurrently, the modeling indicates that respirable dust in these areas ranges from 4.0 mg/m³ to 12.0 mg/m³. Here, it is crucial to emphasize that the field measurements used for validation originate from the longwall face not from LTTC. The validation process involved conducting simulations that encompass all longwall dust sources within the numerical models.

6 RESULTS AND DISCUSSION

0-10s

Figure 8(a) illustrates the aerial view of the dust particle flow pattern five seconds after the initiation of the first caving sequence at chock 51, with the second caving sequence commencing at chock 53. The results show that the particles spread across the rear AFC of three consecutive chocks and the walkway of four successive downstream chocks. Notably, the movement of dust particles in the low-velocity rear AFC region is slower compared to their motion in the high-velocity walkway region.

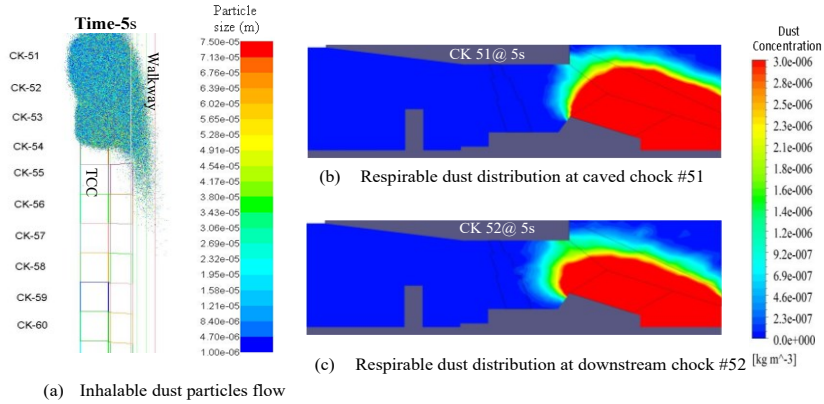

(a) Inhalable dust particles flow

(b) Respirable dust distribution at caved chock #51

(c) Respirable dust distribution at downstream chock #52

Figure 8 Caving dust flow pattern and dust distribution at 5s

Figure 7(b) illustrates the respirable dust at caved chock 51, five seconds into the caving operation. At this location, the walkway is partially covered by dust particles, showing respirable dust of approximately 1.5 mg/m3. A respirable dust cloud originating from the rear AFC region reaches a height of about 2 meters and continues to disperse in all directions.

Figure 8(c) reveals respirable dust at the downstream chock 52. The walkway is predominantly filled with both respirable and inhalable dust particles, and specific regions of the walkway exhibit respirable concentrations surpassing 1.5 mg/m^3. Above the rear AFC region of downstream chock 52, dust completely occupies the space, indicating elevated respirable concentrations exceeding 3 mg/m^3. This underscores the importance of activating dust controls within 5 seconds of initiating the caving sequence in the downstream chock to prevent the migration of dust particles in the walkway region.

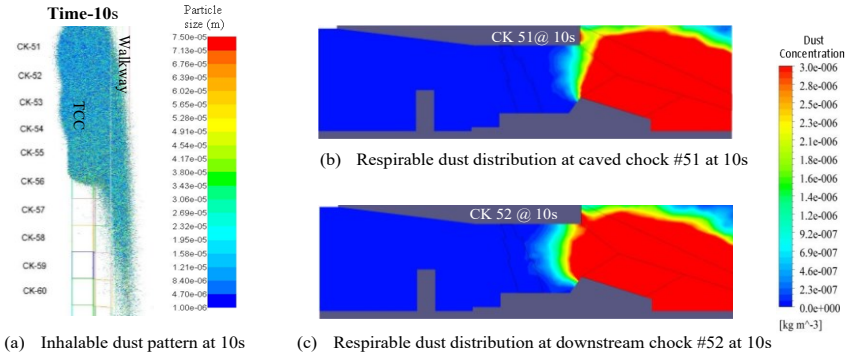

(a) Inhalable dust pattern at 10s

(b) Respirable dust distribution at caved chock #51 at 10s

(c) Respirable dust distribution at downstream chock #52 at 10s

Figure 9 Caving dust flow pattern and dust distribution at 10s

After 10 seconds, marking the conclusion of the caving operation in chock 51, the first chock in the sequential caving sequence, dust particles now envelop the rear AFC in downstream chocks 52-56 and the walkway of downstream supports 52-59, as illustrated in Figure 9 (a). In the caved chock 51, only a segment of the walkway is covered by dust particles, and the respirable dust are below 1.5 mg/m^3, as depicted in Figure 9 (b). From these results, it can be inferred that dust particles enter the caving chock only partially, considering it is the initial chock in the sequential caving operation.

From Figure 9, it can be inferred that dust particles infiltrate the walkway of the immediate downstream chock 52 and the subsequent downstream chocks 53, 54, and 55, exhibiting high respirable dust surpassing 2 mg/m^3 in the walkway. Figure 9 illustrates the dust distributions in downstream chock 55, indicating respirable dust above 2 mg/m^3 in the walkway region. This suggests that respirable dust particles completely migrate into the walkway, while larger particles settle in the rear AFC region of the downstream chocks preceding it.

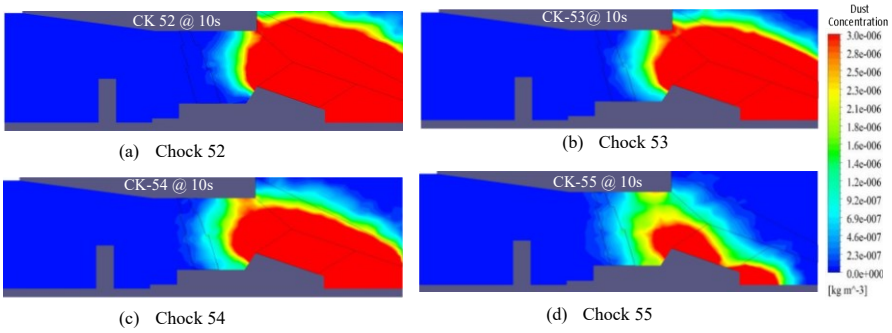

(a) Chock 52 (b) Chock 53

(c) Chock 54 (d) Chock 55

Figure 10 Caving dust distribution at downstream chocks at 10s

11-20s

The third chock in the caving sequence commences at chock #55 and lasts for 10 seconds. At the 15-second mark, the fourth caving chock initiates at chock #52 and continues for 10 seconds. Concurrently, the second chock in the caving sequence at chock #53 persists for an additional 5 seconds, concluding at the 15-second mark. Figure 10(a) illustrates the dust particle flow pattern at 15 seconds, capturing the operation of two consecutive caving chocks at chocks #53 and #55. In addition to the dust induced from the upstream caved chock #51, further dust is generated from the caving chocks #53 and #55, covering the rear AFC regions of chocks #51-57 and the walkway of chocks #52-60.

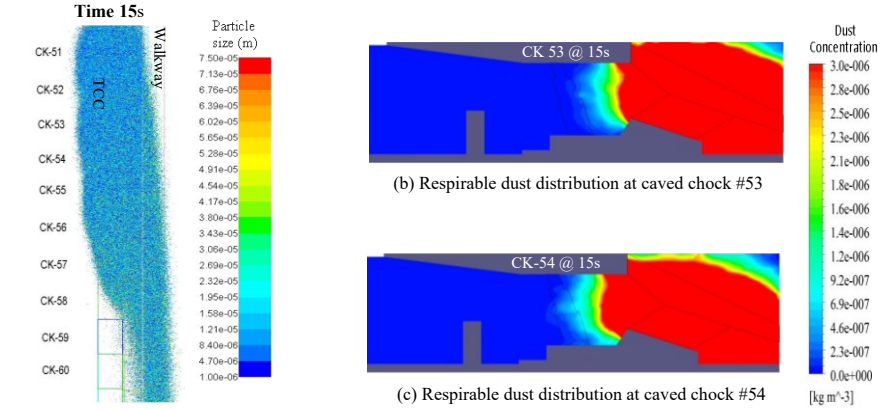

(a)Inhalable dust particle flow pattern at 15s

(b) Respirable dust distribution at caved chock #53

(c) Respirable dust distribution at caved chock #54

Figure 11 Caving dust flow pattern and dust distribution at 15s

Respirable dust above rear AFC reach the face height and small size particles starts to move in normal to the flow direction at chock #53, #54 and #55 which can be observed from the dust distribution indicated in Figure 11 (b), and Figure 12 the respirable dust reach above 2.5mg/m³ in the walkway.

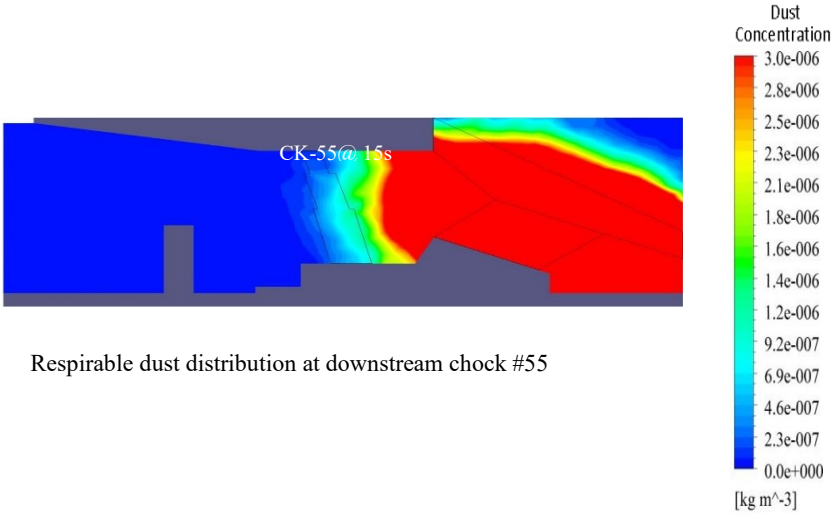

Respirable dust distribution at downstream chock #55

Figure 12 Caving dust distribution at downstream chocks at 15s

In Figure 13, the patterns of dust flow and distribution are depicted at the 20-second mark, coinciding with the initiation of the fourth caving in the sequence at chock 52 for a duration of 5 seconds, and the completion of the third caving in the sequence at chock

55. Figure 13 (a) clearly shows that dust particles blanket the walkway of downstream chocks 53-61, while particles are left in the rear AFC regions of these chocks. Notably, at caving chock 52, there is no caving operation on the upstream side, and the walkway of chock 52 is partially covered with dust, displaying very low respirable dust, as depicted in Figure 13 (b).

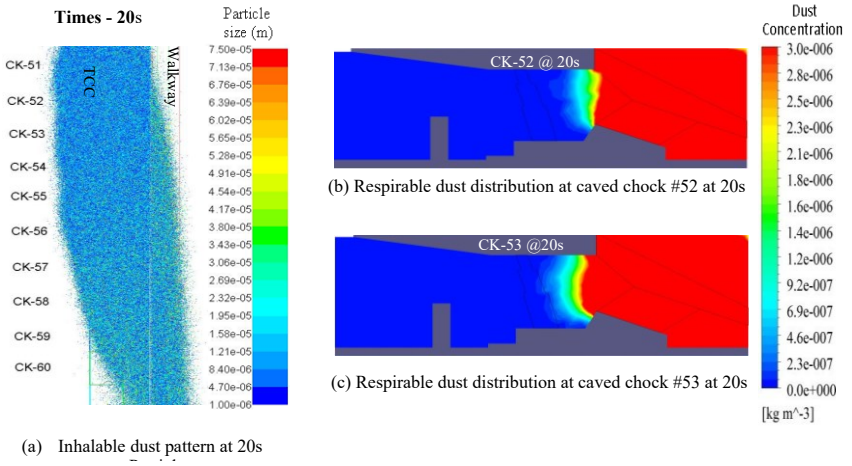

(a) Inhalable dust pattern at 20s

(b) Respirable dust distribution at caved chock #52 at 20s

(c) Respirable dust distribution at caved chock #53 at 20s

Figure 13 Caving dust flow pattern and distributions at caved chock #52 at 20s

In Figure 14(a), the walkway of the caving chock 55 is completely filled with high concentrations of 3mg/m^3 and the concentrations in the walkway of the 3rd caving chock in sequence chock 55 is due to migration of particles from the upstream side of the 2nd and 4th caving supports 52 and 53.

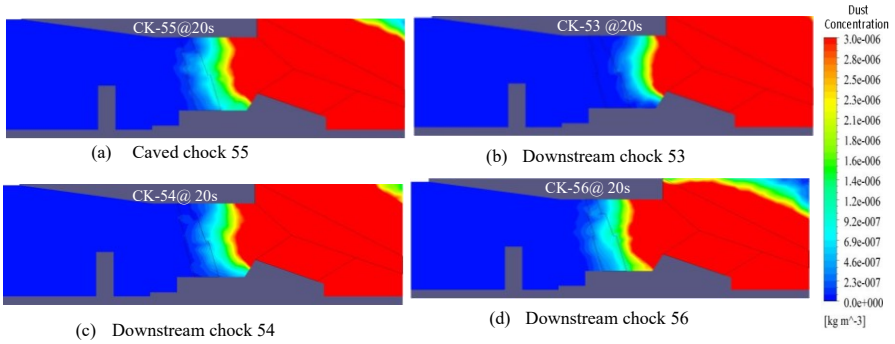

(a) Caved chock 55

(b) Downstream chock 53

(c) Downstream chock 54

(d) Downstream chock 56

Figure 14 Caving dust flow patterns at caved and downstream chocks

21-30s

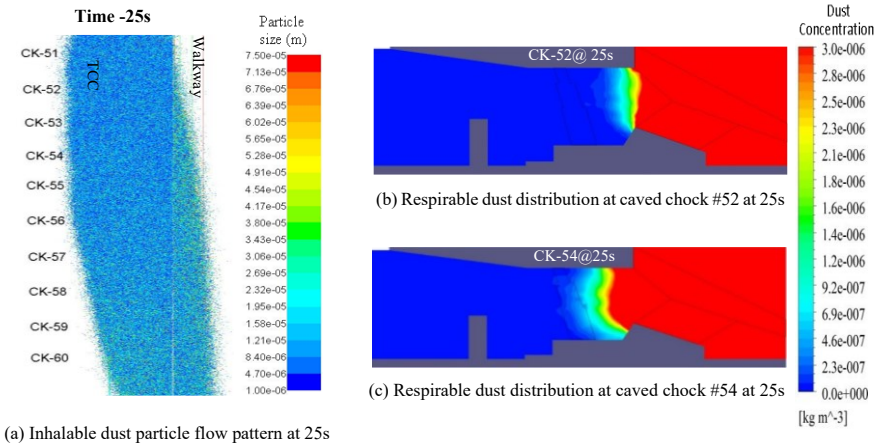

(a) Inhalable dust particle flow pattern at 25s

(b) Respirable dust distribution at caved chock #52 at 25s

(c) Respirable dust distribution at caved chock #54 at 25s

Figure 15 Caving dust flow pattern and dust distributions at caved chock#52 and #54 at 25s

During 21-30s, 4th caving in sequence at chock #52 continues to cave till 25ths. From 20th s, 5th caving in sequence initiates at the chock #54 and caves for 10s. This completes one full caving cycle involving five chocks #51, #52, #53, #54 and #55. Figure 15(a) indicates dust particles cover the walkway and the rear AFC of the downstream chocks 53-60 and Figure 15(b) indicates respirable dust concentration in the walkway of the caved chock #52 with concentrations below 1mg/m³ and only a fraction of the walkway exposed to respirable dust. Figure 15(c) indicates high respirable dust of 2.5mg/m³ in the walkway of the caving chock #54.

At 25s, high respirable dust above 3mg/m³ is observed in most of the walkway regions of the downstream chocks #55, #56 and #58 as indicated in Figure 16. At 30s, high dust concentration above 3mg/m³ is observed in the walkway region of the downstream chocks 55-60 as indicated in Figure 17 and Figure 18.

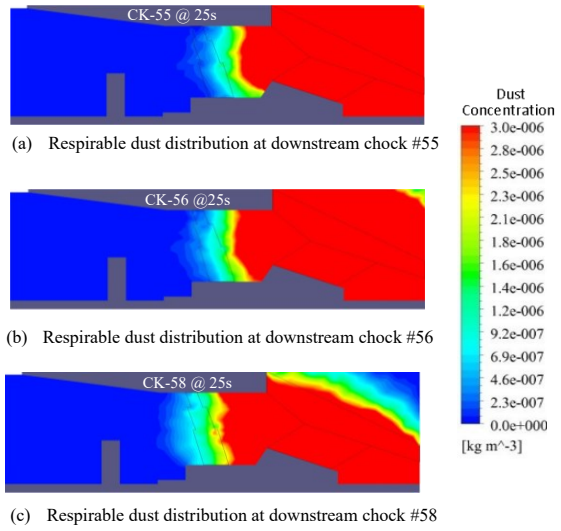

Figure 16 Caving dust distribution at downstream chocks at 25s

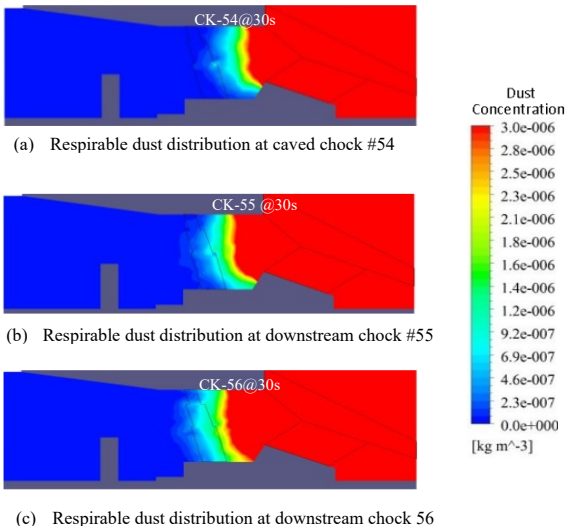

Figure 17 Caving dust distribution at caved chock 54 at 30s

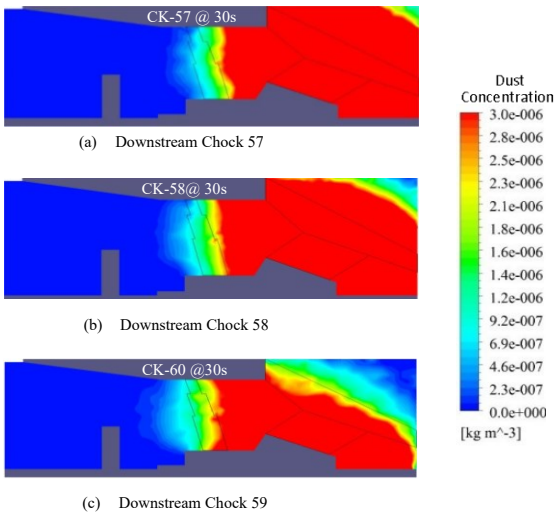

Figure 18 Caving dust distribution at downstream chock 60 at 30s

7 CONCLUSION

In summary, the investigation into transient caving dust modeling aimed to understand the flow patterns of dust during the sequential caving operation across the LTCC face over a 30-second duration. The analysis, conducted at 5-second intervals during the caving operation, focused on the caved chock and its downstream counterparts. Results revealed that respirable dust would partially cover the walkway of the first two chocks (51 and 52), with concentrations remaining below 2mg/m³. Notably, elevated respirable dust of 2.5mg/m³ are consistently observed in the walkway regions of the 3rd, 4th, and 5th caved chocks (53, 54, and 55) throughout the entire 30-second caving cycle.

Furthermore, the study highlighted the migration of respirable dust particles from the rear AFC into the walkway of downstream chocks. Chocks 56 to 60 are found to contain high respirable dust above 3mg/m³. The analysis also pointed out that the ventilation air carried respirable dust over long distances to the downstream chocks, emphasizing the need for comprehensive dust control strategies beyond the caving chock. It is noted that during a single caving cycle, the rear AFC experienced high respirable dust exceeding 3mg/m³, with limited dispersion due to low air velocities in these areas.

The findings underscore the importance of implementing effective dust control measures not only at the caving chock but also at the downstream chocks to prevent air contamination in the walkway. Overall, this study provides valuable insights into the dynamics of respirable dust dispersion during LTCC face caving operations, offering a

foundation for developing targeted strategies to mitigate potential health and safety risks associated with dust exposure.

Airflow patterns in the LTTC face vary significantly at the MG entrance, mid face, and in the TG exit region. This has a significant impact on the caving dust flow patterns. Future work could extend this model to account for variable airflow patterns by incorporating the effects of the caving sequence near the main gate (MG) region and the tailgate (TG) corner areas.

REFERENCES

QUANG, D.H., 2010. The effect of seam dip on the application of the longwall top coal caving method for inclined thick seams. PhD thesis. University of New South Wales.

CAI, Y., BRUCE, B., HEBBLEWHITE, U., ORNDER, B., XU, M., KELLY, M. and WRIGHT, B., 2004. Application of Longwall Top Coal Caving to Australian Operations. ACARP Project C11040.

TANGUTURI, K., BALUSU, R. and MORLA, R., 2014. CFD modelling of methane gas distribution and its control strategies at the tailgate region. Journal of Computational Multiphase Flows, 6(1), pp.65–77.

GREG, D., GLENN, S. and TIM, C., 2007. Top coal caving longwall maximizes thick seam recovery. World of Mining Professionals. Available at: http://www.womp-int.com/story/2007vol5/story025.htm [Accessed 11 Jul. 2025].

REN, T., QIAO, M., ROBERTS, J. AND HINES, J., 2023. Monitoring and computational modelling of ventilation and dust flow in development panel. In: 2023 Resource Operator Conference. University of Wollongong, Wollongong.

CRC Press, 2023. Development of VR-CFD-based training tool for dust control in gateroad development. In: Proceedings of the 19th North American Mine Ventilation Symposium, pp.330–337.

REN, T. and BALUSU, R., 2008. Innovative CFD modelling to improve dust control in longwalls. In: Proceedings of the Underground Coal Operators Conference, pp.137–142.

WORLD HEALTH ORGANIZATION (WHO), 1999. Hazard prevention and control in the work environment: Airborne dust. WHO/SDE/OEH/99.14. Geneva: WHO. Available at: http://www.who.int/occupational_health/publications/en/oehairborne dust.pdf [Accessed 11 Jul. 2025].

ANSYS, 2023. ANSYS 23.0 User Reference Manual.

UNDERGROUND MINING ENGINEERING 46 (2025) 17-40 UDK 62
UNIVERSITY OF BELGRADE - FACULTY OF MINING AND GEOLOGY EISSN 2560-3337

Original scientific paper

DELIQUIFICATION TECHNIQUES AND PREVENTION: A CASE STUDY FOR THE SOUTHERN PANNONIAN BASIN

Ana Ponoćko[1], Bojan Martinović[1], Dino Jovanović Sovtić[2], Miroslav Crnogorac[2], Dušan Danilović[2]

Received: November 29, 2024 **Accepted:** May 15, 2025

Abstract: Liquid loading in gas wells leads to production challenges and decreases the overall recovery from these wells. Gas wells affected by liquid loading struggle to eliminate the liquid that accompanies the produced gas from the wellbore. The primary cause of liquid loading is a low gas flow rate or gas velocity. When the gas velocity falls below the critical threshold needed to transport liquid to the surface, the liquid begins to accumulate in the vertical section of a well, the lateral section of a horizontal well, and even within hydraulic fractures. Another indication of liquid loading is the high casing over tubing pressure. The focus of the case study on an onshore gas well is addressing the issue of liquid loading in Southern Pannonian Basin conditions. A well was selected that experienced a gradual decline in production and head pressure. A model was created using PipeSim software, followed by a sensitivity analysis under various operational scenarios. The significance of this study lies in optimizing the well parameters to prevent the occurrence of liquid loading. The paper is structured around relevant works, background, case study, methodology, results, and conclusions.

Keywords: Gas Well, Liquid Loading, Well Modeling, Well Performance Optimization, Southern Pannonian Basin, Gas Rate, Gas Velocity

1 INTRODUCTION

Gas-phase hydrocarbons produced from underground reservoirs often coexist with liquid-phase materials, which can impact the well's flowing characteristics. These liquids may originate from the condensation of hydrocarbon gas (condensate) or from interstitial water within the reservoir matrix. Since the higher-density liquid phase is typically discontinuous, it must be transported to the surface by the gas. If the gas phase does not generate enough transport energy to lift the liquids, they will accumulate in the wellbore. This accumulation creates additional back pressure on the formation, which can

[1] NTC NIS Naftagas doo, Narodnog fronta 12, 21000 Novi Sad
[2] University of Belgrade - Faculty of Mining and Geology, Djusina 7, Belgrade, Serbia

E-mails: ana.ponocko@nis.rs; bojan.martinovic@nis.rs; dino.jovanovic@nis.rs miroslav.crnogorac@rgf.bg.ac.rs, ORCID 0000-0002-8078-2684 dusan.danilovic@rgf.bg.ac.rs, ORCID 0000-0002-2969-040X

significantly reduce the well's production capacity. In low-pressure wells, liquid accumulation may completely kill the well, while in higher-pressure wells, it can cause varying degrees of slugging or churning, complicating routine well test calculations (Turner RG, Hubbard MG, Dukler AE 1969).

Liquid loading in gas wells can be challenging to detect and manage. A comprehensive diagnostic analysis of well data is essential to predict how quickly liquids will accumulate. Researchers have focused on determining the minimum gas flow rate needed to prevent this issue, considering various influencing factors. One significant factor is the water content of wet gas. As the wellbore temperature decreases, the water-gas ratio tends to decline, affecting the likelihood of liquid accumulation. Despite extensive studies on this topic, existing models in the industry still exhibit considerable inaccuracies, particularly regarding the prediction of the minimum gas flow rate necessary to avert liquid loading in the wellbore. Improving these predictive models is crucial for effective well management and operational efficiency (Nawankwo I. Abaku G. Kinate B.B. 2020).

The aim of this paper is to present a case study of an onshore gas well that is facing recurring issues related to liquid loading. Using PipeSim software, a base model of the well was meticulously developed. This was followed by a sensitivity analysis focusing on the formation of liquid loading under various operational scenarios. The study further explores and analyzes different strategies, including adjustments to the tubing diameter and choke settings. Understanding and predicting liquid loading is crucial for the safe production of gas fields (Ješić M. Martinović B. 2023).

This study is significant as it aims to optimize the well's performance and mitigate the risks associated with liquid loading. The findings of this study will provide practical solutions for industry practitioners and researchers dealing with onshore gas wells (Ješić M. Martinović B. 2023).

The remainder of the paper is structured as follows Section 2 is theoretical background and section 3 highlights related work. The experimental setup and its results from real-world applications are detailed in Sections 4 and 5, respectively. Finally, conclusions are presented in Section 6 (Ješić M. Martinović B. 2023).

2 THEORETICAL BACKGROUND

Liquid loading is the primary cause of production impairment in gas wells, leading to erratic slug flow and reduced output. If liquids are not continuously removed, the well may eventually become nonproductive or operate below its potential. Therefore, it is crucial to identify the causes of liquid loading and implement appropriate remedial actions. This usually happens when the production rate and reservoir pressure drop. Liquid loading can eventually cause the well to fail by causing irregular gas production and a drop in generated liquids.

2.1 Flow regimes

To understand the impact of liquids in a gas well, it's essential to examine the interaction between the liquid and gas phases under flowing conditions. Multiphase flow in a vertical conduit is typically characterized by four fundamental flow regimes, as illustrated in Figure 1. At any point in a well's operational history, one or more of these regimes may be present. The flow regime is influenced by the velocities of the gas and liquid phases as well as the relative proportions of gas and liquid at any specific location within the flow stream.

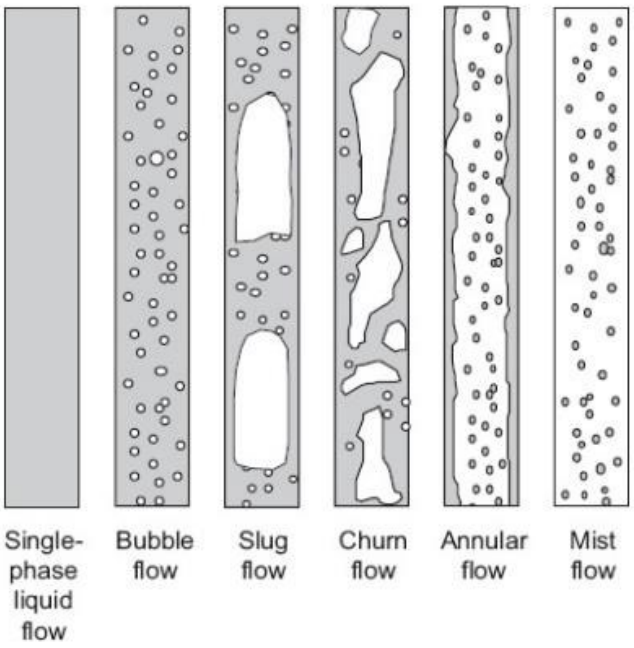

Figure 1 Flow regimes (Jan-Dirk J. 2017)

Bubble Flow: The tubing is nearly entirely filled with liquid, with free gas existing as small bubbles that rise through the liquid. The liquid makes contact with the wall surface, while the bubbles primarily serve to lower the overall density (Sankar, S., & Karthi, S. A., 2019).

Slug Flow: As gas bubbles rise, they expand and merge into larger bubbles and eventually form slugs. The liquid phase remains continuous, but the liquid film surrounding the slugs may descend. Both gas and liquid phases have a substantial impact on the pressure gradient (Sankar, S., & Karthi, S. A., 2019).

Slug-Annular Transition: The flow shifts from a continuous liquid phase to a continuous gas phase. Some liquid may be carried as droplets within the gas. Although

gas influences the pressure gradient more significantly, the presence of liquid is still significant (Sankar, S., & Karthi, S. A., 2019).

Generally, most oil wells operate in the bubble flow and slug flow regimes along most of their length, while most gas wells function in the annular flow regime. Solving the equations based on the physical laws governing these flow types is a complex task. There are numerical simulators designed for sensitive industrial processes that require meticulous modeling. However, within the oil industry, a simpler approach is often taken. Empirical correlations have been developed through extensive experimentation. Some of these correlations are published, while others remain proprietary to oil or service companies.

The complexity of these correlations varies. Some are applicable across all flow regimes, while others have distinct correlations for each regime. Some methods incorporate basic physics, such as modeling gas/liquid interface behavior, while others rely entirely on empirical data. For an overview, we refer to Brill and Mukherjee (1999), Beggs and Brill Original, Govier and Aziz (2008). Many of these correlations are integrated into modern well simulators, but caution is warranted, as they are often only suitable for specific types of wells. It's important to note that the correlations used for oil properties can influence the results and may lead to inaccuracies. (Jan-Dirk, 2017)

Liquid loading in a gas well can be identified by various symptoms. If detected early and addressed promptly, appropriate actions can significantly reduce losses in gas production.

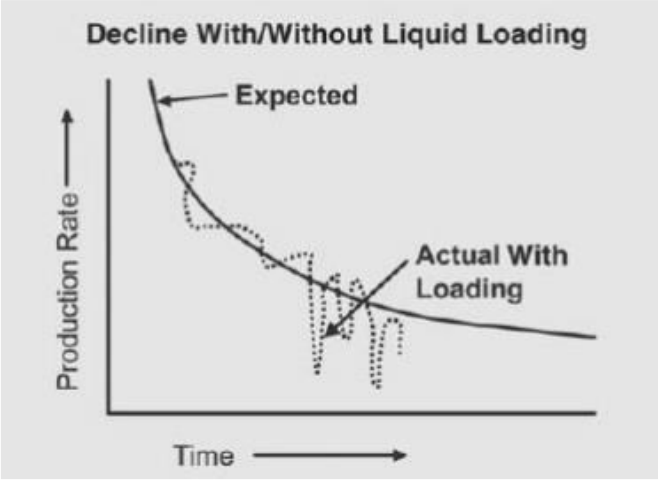

Figure 2 Decline curve showing onset of liquid loading (Lea, 2004)

2.2 NODAL analysis

In Nodal analysis, the system is divided into two subsystems at a specific location known as the nodal point. The first subsystem considers the inflow from the reservoir to the nodal point (Inflow Performance Relationship, or IPR), while the second subsystem addresses the outflow from the nodal point to the surface (Vertical Lift Performance, or VLP). The curves generated by these relationships on a pressure-rate graph are referred to as the inflow curve and the outflow curve, respectively. The intersection of these two curves indicates the optimum operating point, where pressure and flow rate are equal for both curves.

NODAL analysis is used as the primary approach. By employing nodal analysis, researchers can identify and analyze numerous factors that influence well performance, providing valuable insights into how the well is expected to behave under various scenarios. This method offers a comprehensive view of the entire well system, enabling precise predictions and targeted optimizations to enhance overall performance (Ješić M. Martinović B. 2023).

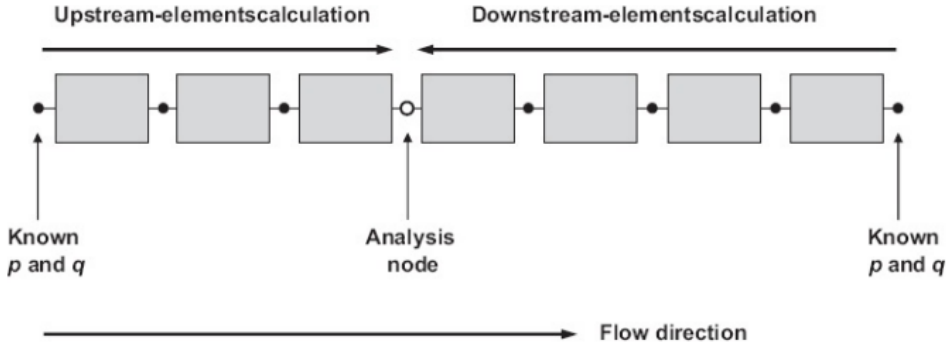

Figure 3 Procedure for Nodal analysis (Jan-Dirk J. 2017)

IPR Curve (Inflow Performance Relationship): The IPR curve represents the relationship between the reservoir pressure and the production rate of a well. It describes the ability of the reservoir to deliver fluids to the wellbore at different production rates. The difference between the reservoir pressure and the flowing bottomhole pressure of a well is the driving force for inflow into the wellbore. (Golan & Whitson, 1991)

VLP Curve (Vertical Lift Performance): The VLP curve represents the relationship between the tubing intake pressure (or flowing bottomhole pressure) and the production rate. It describes the ability of the production tubing to transport fluids from the wellbore to the surface at different rates. The intersection of the IPR and VLP curves is utilized to establish the rate of stable natural flow for an oil well. At this point of intersection, the reservoir's capacity to deliver fluids aligns with the tubing's capacity to transport those fluids to the surface, leading to a stable and balanced flow condition. This represents the

rate at which the well can flow naturally while sustaining a consistent flowing bottomhole pressure (Ješić, Martinović, 2023).

A common method for analyzing well performance is through a Nodal Analysis plot, which enables a visual assessment of the impact of various system components (PipeSim, 2017).

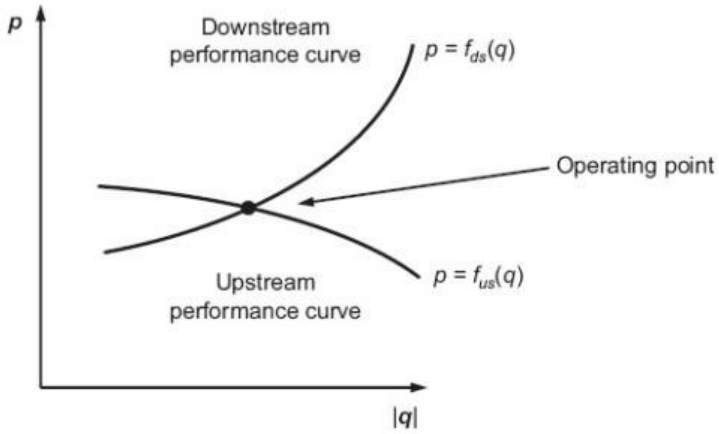

Figure 4 The intersection between the downstream and upstream performance curves defines the operating point (Jan-Dirk J. 2017)

1. The two curves do not intersect, indicating that the system cannot operate under the assumed conditions (i.e., the specified reservoir and manifold pressures).

2. The curves intersect at one or more points. Typically, we identify a single intersection, known as the operating point or working point. The desired flow rate can be obtained from the horizontal axis, while the corresponding pressure can be read from the vertical axis. (Jan-Dirk J. 2017).

Productivity index represents the ratio of the total liquid flow rate at the surface to the pressure drawdown at the midpoint of the producing intervals and represents the simplest equation within the IPR framework, as shown in Equation 1 (Golan & Whitson, 1991)

$$J = \frac{Q}{P_r - P_{wf}} \tag{1}$$

Where:

J – Productivity index, m³/d/bar

Q- Surface flowrate at standard conditions, m³/d

P_r – Static bottom hole pressure, bar

P_{wf} – Flowing bottom hole pressure, bar

Vogel gives the second available method in Eq. 2 (Vogel, 1968).

$$Q = Q_b + (Q_{max} - Q_b)(1 - 0.2\frac{P_{wf}}{P_b} - 0.8\frac{P_{wf}^2}{P^2}) \quad (2)$$

Where:

Q – Production rate, m³/d

Pb – Bubble point pressure, bar

Qmax – Maximum vogel rate, m³/d

Qb – Measured rate at bubble point, m³/d

We use this method when we have one measurement.

In traditional Nodal analysis, common locations for the analysis node correspond to various types of pressures, including:

- Flowing bottomhole pressure (Figure 5)
- Flowing tubing head pressure (just upstream of the wellhead choke)
- Flowline pressure, at the entrance of the flowline just downstream of the wellhead choke
- Manifold pressure, at the end of the flowline

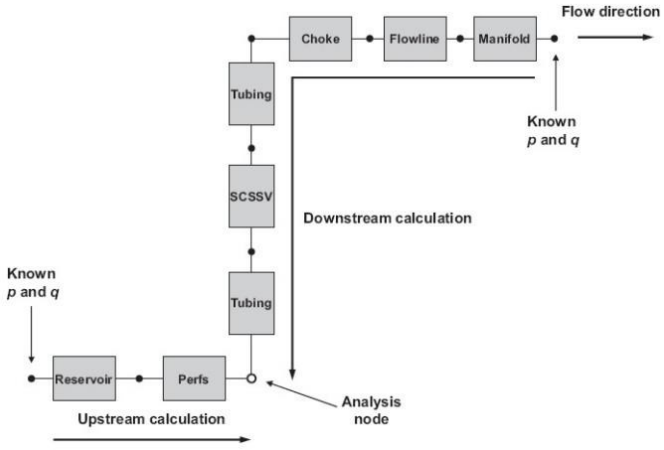

Figure 5 Nodal analysis configuration with analysis node at the well bottom (Jan-Dirk J. 2017)

3 RELATED WORK

Nwankwo (2019) Liquid loading in gas wells creates production challenges and decreases overall recovery. This issue arises when the upward gas velocity drops below a critical threshold, leading to liquid accumulation at the bottom of the well. This accumulation can reduce production rates and, in extreme cases, render the well inactive. While various methods have been suggested to predict the onset of liquid loading, understanding the impact of flow parameters is crucial for addressing this problem.

This study analyzes key flow parameters—including tubing wellhead pressure, water-gas ratio (WGR), condensate-gas ratio (CGR), tubing size, and flow regimes—using PROSPER software. The goal is to assess how these parameters influence liquid loading and optimize gas well production through effective selection and management of flow conditions. By varying and inputting flow and PVT parameters, results indicate that increased tubing wellhead pressure enhances the likelihood of liquid loading due to a corresponding rise in the minimum unloading flow rate.

James J. Sheng presented the project employed a combination of surfactant injection and gas lift to reduce liquid density and enhance flow. The project achieved a significant increase in overall recovery rates, showcasing the successful application of deliquification techniques in a multi-phase production environment.

Gool et al. (2008) developed a model that aligns well with real-life data to predict the gradual decline in well production rates caused by liquid loading. Their research focuses on identifying the key parameters that influence liquid accumulation and the subsequent impact on gas production, providing valuable insights for managing and mitigating liquid loading in gas wells. This model can be particularly useful for operators looking to optimize production strategies and reduce downtime associated with liquid loading issues.

Turner et al. (1969) researched the analysis and prediction of the minimum flowrate for the continuous removal of liquid from gas wells where they analysed the equation used for calculating the minimum flowrate from physical properties which was proposed by Jones (1947) and Duckler (1960).

A study by Joseph A. considers a broad perspective of how liquid loading has been managed over the years and develops classifications for liquid loading problems based on the sources of the liquids, the severity of the problem, the preventive measures and the treatment strategies available in the industry. A comparative analysis of some of the predictive models was made along with a new model using Matlab. The result shows that at pressures below 2500psi and pressures above 5000psia; the modified model perform better than Turner et al's model whereas at pressures between 2500 and 5000psia, Turner et al's model performed better than other models.

Schlumberger made attempt to address liquid loading issues using an integrated approach. Their report indicates that they analyzed available well data, assessed the current status and performance of the well, diagnosed its condition, selected the most suitable production system, managed the data, and optimized operations. To define the well model and align actual production data with simulated behavior, they employed composite system NODAL analysis using PipeSim software. Once the well model was validated, system analysis was used to evaluate future well performance and to select appropriate production systems by comparing results from various input parameters and conditions. Additionally, this analysis helped diagnose the causes of decreased gas production.

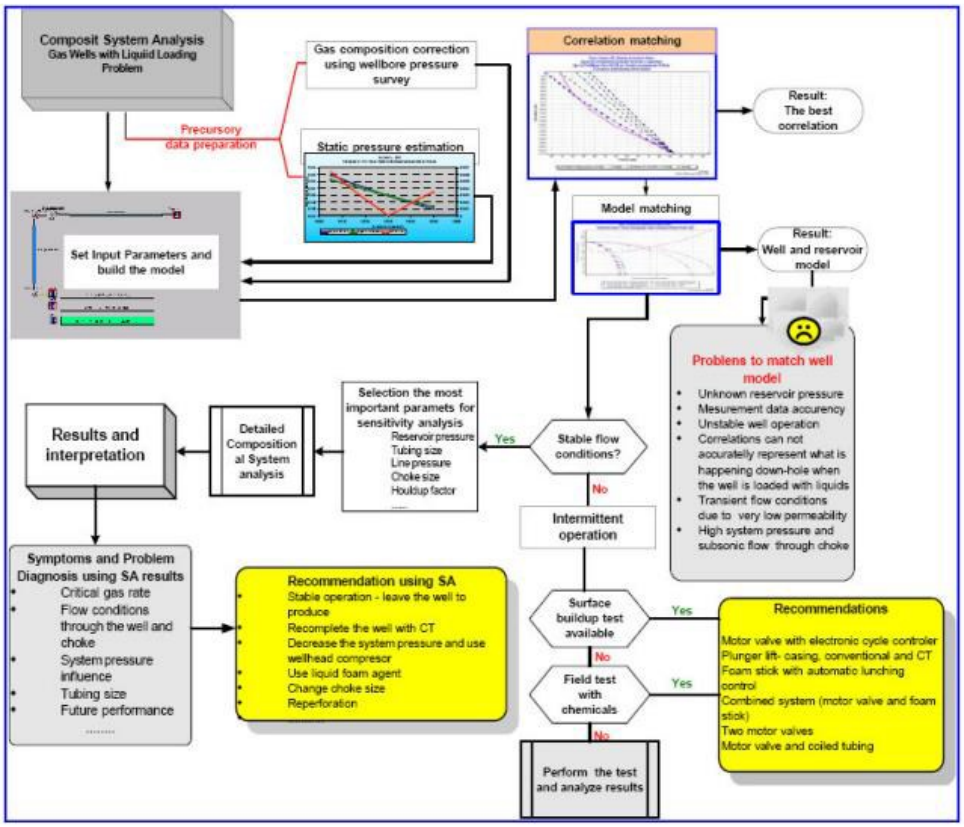

Figure 6 Well performance model for gas wells with liquid loading problem (Schlumberger, 2006)

In Figure 6 the flow chart of the procedure for defining well performance is shown.

4 CASE STUDY

Figure 7 shows the production profile created based on the data provided in section 4.2 (Data collection). Analyzing the production profile, we can conclude that the well was stopped in February 2024, due to issues related to liquid loading. On the production profile, it is observed that the well produces approximately 12,000 m³/day after the workover. There is a gradual decrease in production over time. In April, production was recorded at 11,000 m³/day, and it continued to decline, reaching 9,000 m³/day in August. The well is produced with a surface choke that has a diameter of 3.3 mm. The goal is to determine the reasons for the decline in production and the decrease in the wellhead pressure.

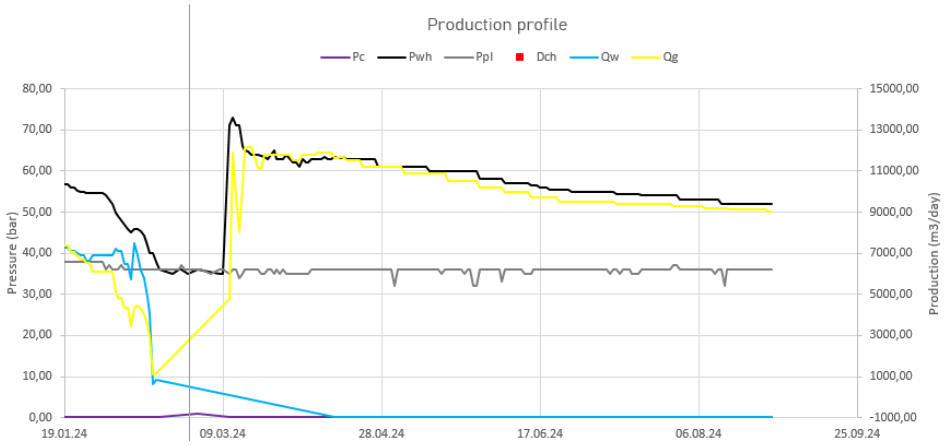

Figure 7 Production profile

4.1 Methodology

In this study, a methodology was used that consists of several steps providing a systematic approach to achieving our research objectives. In the following sections, these sequential phases are described in detail: Data Collection, Data Validation, Model Creation and Matching, Sensitivity Analysis, and Finalization of Results. Each step is clearly defined and aims to facilitate the understanding and interpretation of the data. Figure 8 illustrates the methodology which ultimately aims to provide solutions based on the results of the sensitivity analyses obtained (Ješić M. Martinović B. 2023).

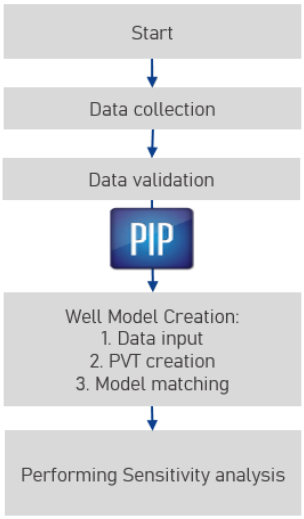

Figure 8 Schematic representation of methodology

The creation of a well model during NODAL analyses consists of the following steps:

1. Input Well completion details: Tubing size, casing size, completion type, and any artificial lift methods if applicable.
2. PVT data Input information such as fluid composition, density, viscosity, and components and value.
3. Define IPR: Establish the relationship between wellbore pressure and production rate.
4. Definition HD measurements: Data from the results of the last relevant measurements of dynamic pressure profiles in the well are entered.
5. Define VLP: Define the VLP models to characterize the well's response to changes in tubing and casing pressures
6. Run Nodal Analysis: PipeSim will calculate pressures, temperatures, and flow rates at different points in the well and production system (Ješić M. Martinović B. 2023).
7. Review Results: Analyze the simulation results, focusing on parameters such as wellhead pressure, tubing and casing pressures, flow rates, and temperature profiles. Evaluate the well's performance under different operating conditions (Ješić M. Martinović B. 2023).

8. Optimization: If necessary, adjust parameters such as choke size, completion design, or artificial lift settings to optimize well performance (Ješić M. Martinović B. 2023).

4.2 Data Collection

The data collected for this well was obtained from an onshore gas well that is facing issues with liquid loading. In Table 1, we can see the well facts and data obtained from the model, where we can conclude that the created model aligns with the actual data. Table 2 contains the data used to create the PVT dataset. Table 3 includes the data for hydrodynamic measurements, while Table 4 presents the input well completion details. Table 5 was used for entering information about the surface equipment

Table 1 Input data

Parameter	Pres [bar]	Pbh [bar]	Pwh [bar]	Ppl [m³/day]	Qg [m/day]	Qf [bar]
Input data	95	92,8	65	35	12312	0,4
Model results	95	92,9	66,9	35	12301	0,4

Table 2 PVT data

Serial number	Components	Unit of measure	Value
1.	Methane	mol %	97.91
2.	Ethane	mol %	0.14
3.	Propane	mol %	0.04
4.	Isobutane	mol %	0.00
5.	Butane	mol %	0.00
6.	Isopentane	mol %	0.00
7.	Pentane	mol %	0.00
8.	Hexane	mol %	0.00
9.	Nitrogen	mol %	1.49
10.	Carbon Dioxide	mol %	0.39
11.	Average molecular weight	g/mol	16.37
12.	Density relative to air	/	0.5660
13.	Density	kg/m3	0.6936

14.	Wobbe's index (bottom)	MJ/m3	44.44
15.	Lower heating value	MJ/m3	33.43

Table 3 HD measurements

Depth m	Pressure (kPa) – Level (m) Staircase Dynamic kPa	Dynamic Grad. kPa/m
0	6502	
200	6838	1,18
400	7127	1,45
600	7516	1,95
800	7998	2,41
900	8208	2,10
1000	8448	2,40
1100	8676	2,28
1200	8898	2,22
1250	9009	2,22
1300	9120	2,22
1345	9245	2,78

Table 4 Data on production equipment

Data on production equipment			
1	Inside diameter of column	124,26	[mm]
2	Column outer diameter	139,7	[mm]
3	Column section length	1469,39	[m]
4	Column grade	K-55	
5	Tubing inner diameter	62	[mm]
6	Tubing outer diameter	73,02	[mm]
7	Tubing section length	1342,4	[m]
8	Tubing grade	J-55	
9	Packer installation depth	1344,49	[m]
10	Special equipment (description, characteristics, installation depth)	✓	
11	Perforation top	1360	[m]

12	Perforated interval length	1	[m]	
13	Inclinometer data	✓		
14	Geothermal gradient	[°C/m]	[°C/m],	Not necessary, preferred

Table 5 Surface equipment data

Data on surface equpment			
1	Pipeline length	8600	[m]
2	Internal diameter of the pipeline	73	[mm]
3	Pipe wall thickness	7	[mm]
4	Coefficient of thermal conductivity of pipelines	X	[W/mK]
5	Absolute roughness of the inner wall of the pipeline	X	[mm]
6	Average digging depth	0,8 - 1 m	[m]
7	Soil temperature at the depth of burial	X	[°C]
8	Thermal conductivity coefficient of the soil	X	[W/mK]
9	Thermal conductivity coefficient of polyurethane foam insulation	X	[W/mK]
10	Separator pressure	36	[kPa]
11	Separator temperature	X	[°C]

4.3 Model creating

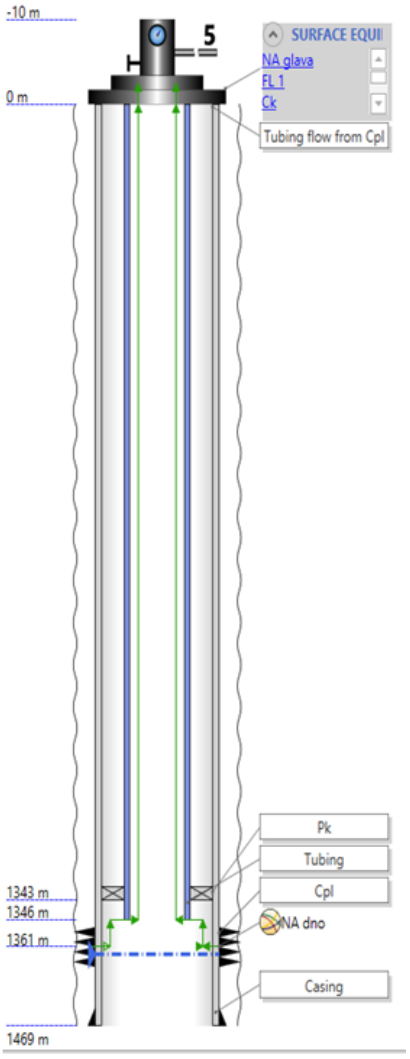

Figure 9 Sketch of well

When creating a model, the first step is to define the fluid characteristics, well construction, production, and pressures at Nodal points. The first Nodal point is defined at the bottom of the well, and the second at the wellhead. The correlations used in the model creation for Vertical Lift Performance are the Beggs and Brill Original, while the Inflow Performance Relationship is determined using the PI method (Beggs, 2008).

5 RESULTS AND DISCUSSION

In section 4.2 (Data Collection), Table 1 (Input Data) presents the actual data for the well. The results of the baseline model (the solution at the bottom and the solution at the top) are analyzed. The results indicate values that are approximately the same as those in the input data from Table 1, suggesting that the model is well constructed, that the data used for model execution is accurate and well validated, and that the model accurately represents the real behavior of the well in the virtual world. With an accurate model established, sensitivity analyses can be performed. The following section will conduct these sensitivity analyses and provide suggestions for addressing the issue of liquid loading.

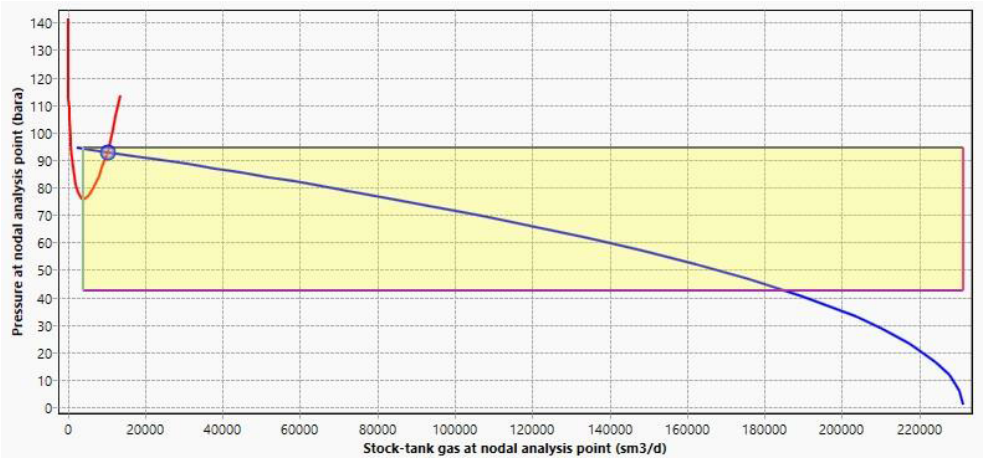

Figure 10 Nodal point at the bottom

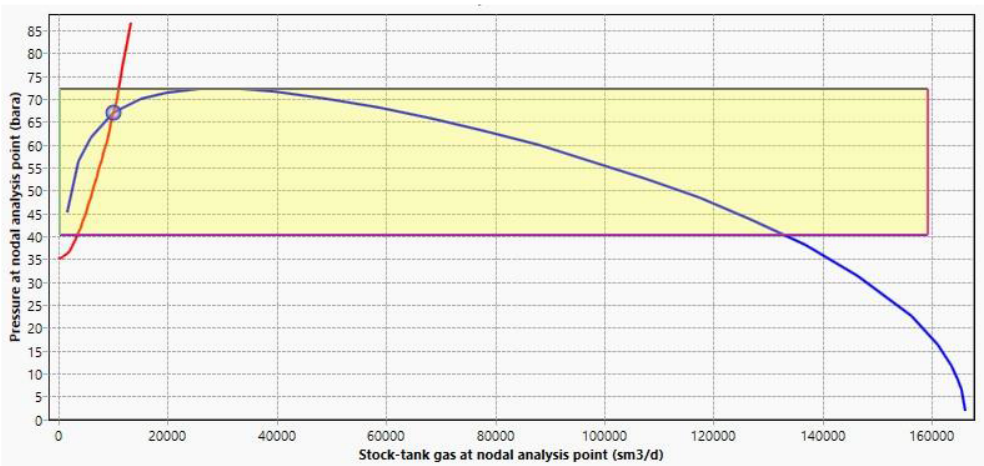

Figure 11 Nodal point at the head

Sensitivity analysis of the surface choke diameter

A sensitivity analysis of the surface choke diameter has been performed on the baseline well model. The choke diameter varied from the current diameter of 3.3 mm to 7 mm.

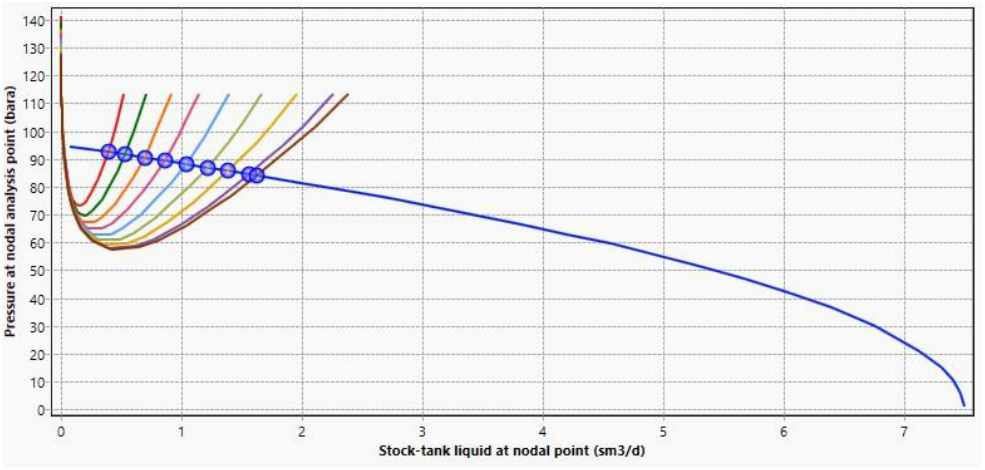

Figure 12 The solution at the bottom

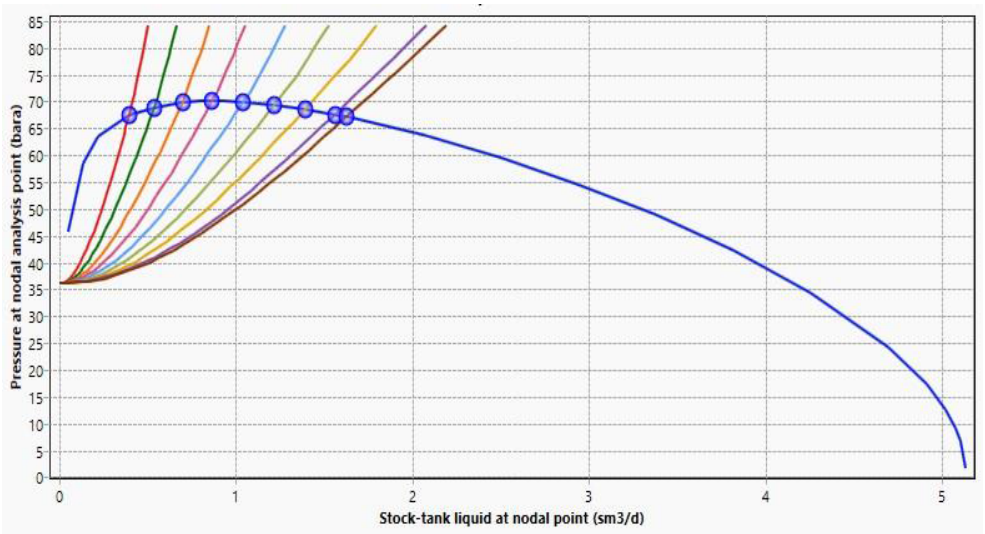

Figure 13 The solution at the head

What can be concluded from Figures 12 and 13 is that an increase in the diameter of the choke leads to a rise in gas production and a gradual decrease in bottom pressure. In further interpretations, a more detailed account of the results obtained from the sensitivity analysis of the surface choke will be provided.

Table 5 Results of the sensitivity analysis for the diameters of the surface choke

Diameter	**3.3 mm**	3.8 mm	4.3 mm	5.3 mm	5.8 mm	6.3 mm	6.8 mm	7 mm
Qg m³/d	**12301**	16624	21598	26798	32172	37609	42985	48198
Pwh bar	**67,4**	68,7	69,8	70,1	69,9	69,4	68,5	67,5
Pbh bar	**92.4**	91.5	90.5	89.3	88.1	86.9	85.7	84.5

In the previously mentioned data from section 4.2, the gas production at the well is 12,312 m³/day. Therefore, we can conclude that the choke installed at the well, which is 3.3 mm, is appropriate. The production we obtain with the 3.3 mm is 12,301 m³/day.

Through sensitivity analysis of choke diameter changes, we have provided possible suggestions for addressing the issue of liquid loading. It is important to note that when deciding on the choke diameter, geological conditions and system conditions must be taken into account.

Sensitivity analysis of the liquid loading

Due to the intermittent production of water, an analysis of the liquid phase removal was conducted to determine the conditions for stable well operation. The analysis results show that the well is at risk of liquid phase retention. (Figure 14) The necessary critical gas velocity was obtained, as well as the production that needs to be achieved to avoid this risk.

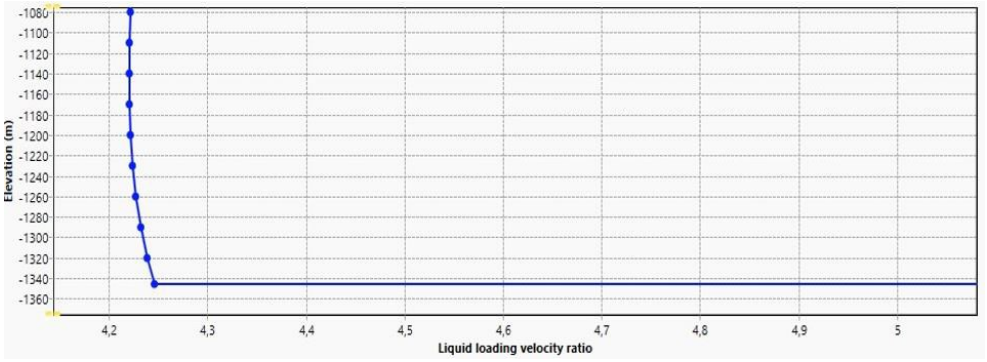

Figure 14 Liquid loading velocity ratio

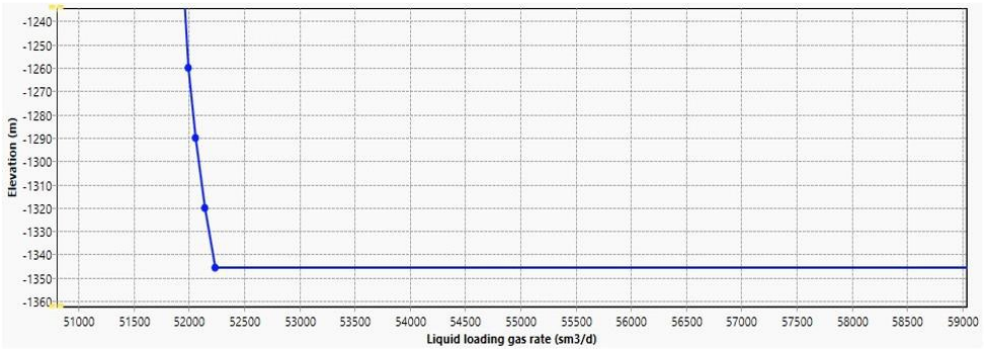

Figure 15 Liquid loading gas rate

In Figure 14, it can be concluded that the liquid loading velocity ratio is 4.25, while Figure 15 indicates a liquid loading gas ratio of 52,300 m³/d. Given that the liquid loading velocity ratio and liquid loading gas ratio have not been achieved, the well is at risk of liquid loading and is therefore a suitable candidate for chemical dosing. The initial solution to address the issue of liquid loading involves the dosing of chemicals. Under the specified conditions of this well type, the recommended practice is to administer the chemical foamers bi-monthly. Since PipeSim does not have the option for dosing the foamer, dosing is suggested based on the analysis of similar conditions in the well.

Sensitivity analysis of the tubing diameter

In the sensitivity analysis of tubing, several diameters were considered: 62 mm, 50.67 mm, 31.29 mm, and 26.21 mm. The objective of this sensitivity analysis is to identify the tubing diameter that achieves the most optimal conditions for mitigating the issue of liquid loading. It is essential to ensure that the liquid loading velocity ratio (LLVR) remains below 1, while also meeting the production requirements associated with the well.

	Operating point	ST Liq. at NA	P at NA	ST Gas at NA	BHP	P at WH
		sm3/d	bara	sm3/d	bara	bara
1	IDIAMETER=61.99...	0.3986104	92.44161	12302.77	92.44161	67.45001
2	IDIAMETER=50.67...	0.4134558	92.34484	12760.96	92.34484	69.39623
3	IDIAMETER=31.29...	0.3849366	92.53064	11880.74	92.53064	66.14021
4	IDIAMETER=26.21...	0.3319073	92.87512	10244.03	92.87512	59.85454

Figure 16 Output

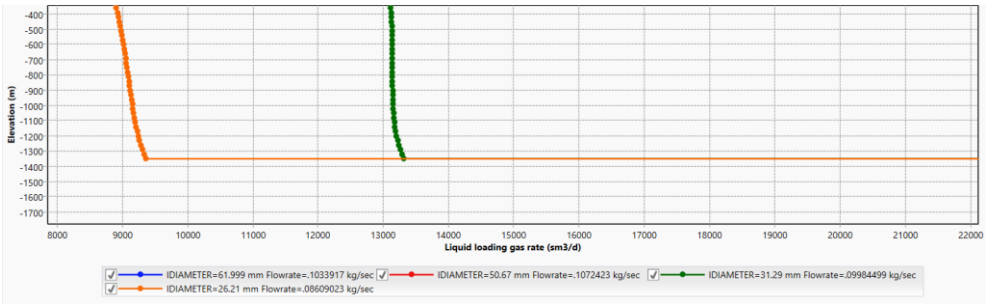

Figure 17 Liquid loading gas rate

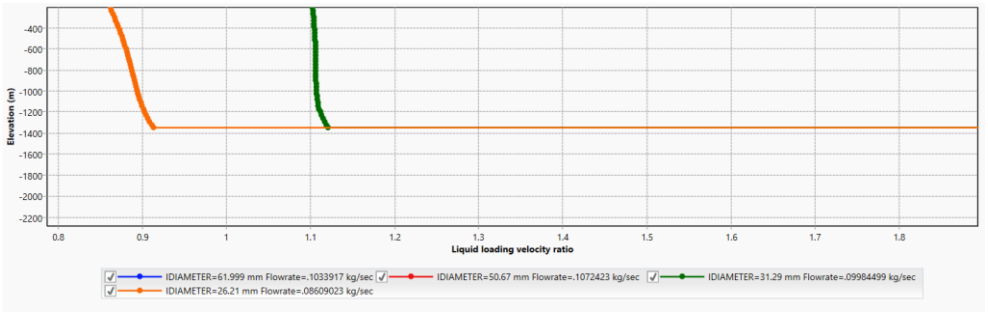

Figure 18 Liquid loading velocity ratio

The optimal solution indicates a tubing diameter of 26.21 mm if production conditions are not considered. The next step is to include both the tubing diameter and the choke diameter in the analysis to achieve better results that correspond to production conditions. LLVR=0,91 and LLGR=9300 m³/d.

Sensitivity analysis of the tubing diameter and choke diameter

In the analysis of tubing with different diameters and choke diameters (3.3 mm to 7 mm), it was found that better results were obtained compared to the analysis of tubing diameter alone. The optimal tubing diameter is 31.29 mm, with a choke diameter of 3.8 mm. This combination yields optimal production while successfully addressing the issue of liquid loading. The liquid loading gas rate (LLGR) is 13,400 m³/d, and the liquid loading vapor ratio (LLVR) is 0.9.

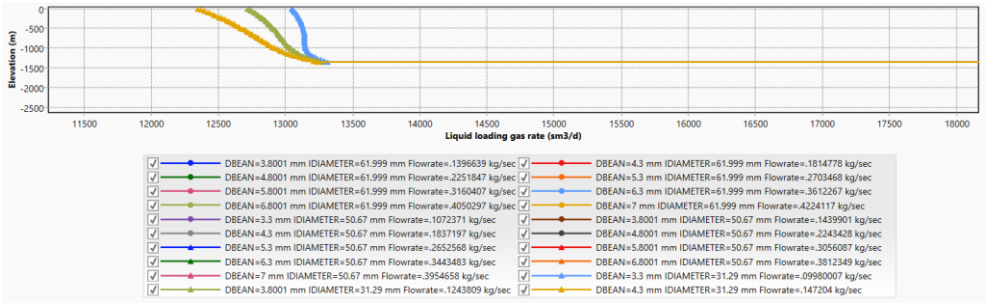

Figure 19 Liquid loading gas rate

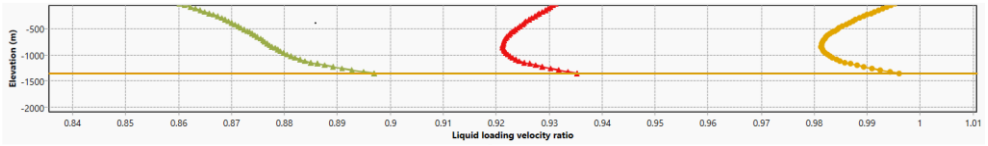

Figure 20 Liquid loading velocity ratio

	Operating point	P at NA	ST Gas at NA	BHP
		bara	sm3/d	bara
1	DBEAN=3.3 mm IDIAMETER=61.999 mm...	67.45001	12302.77	92.44161
2	DBEAN=3.8001 mm IDIAMETER=61.999...	68.63148	16618.87	91.52608
3	DBEAN=4.3 mm IDIAMETER=61.999 mm...	69.77052	21594.38	90.45917
4	DBEAN=4.8001 mm IDIAMETER=61.999...	70.11162	26795.14	89.33035
5	DBEAN=5.3 mm IDIAMETER=61.999 mm...	69.92023	32169.07	88.14876
6	DBEAN=5.8001 mm IDIAMETER=61.999...	69.35022	37606.27	86.93692
7	DBEAN=6.3 mm IDIAMETER=61.999 mm...	68.51661	42983.04	85.72169
8	DBEAN=6.8001 mm IDIAMETER=61.999...	67.50916	48195.23	84.52699
9	DBEAN=7 mm IDIAMETER=61.999 mm FI...	67.06297	50263.54	84.0482
10	DBEAN=3.3 mm IDIAMETER=50.67 mm F...	69.39596	12760.34	92.34498
11	DBEAN=3.8001 mm IDIAMETER=50.67 m...	70.54523	17133.65	91.41627
12	DBEAN=4.3 mm IDIAMETER=50.67 mm F...	70.67652	21861.15	90.40161
13	DBEAN=4.8001 mm IDIAMETER=50.67 m...	70.14454	26694.96	89.35223
14	DBEAN=5.3 mm IDIAMETER=50.67 mm F...	69.1659	31563.4	88.28272
15	DBEAN=5.8001 mm IDIAMETER=50.67 m...	67.8838	36364.95	87.21507
16	DBEAN=6.3 mm IDIAMETER=50.67 mm F...	66.41798	40974.64	86.17762
17	DBEAN=6.8001 mm IDIAMETER=50.67 m...	64.84157	45363.85	85.17806
18	DBEAN=7 mm IDIAMETER=50.67 mm FI...	64.19014	47057.21	84.78928
19	DBEAN=3.3 mm IDIAMETER=31.29 mm F...	66.14396	11875.39	92.53177
20	DBEAN=3.8001 mm IDIAMETER=31.29...	63.64419	14800.32	91.91294
21	DBEAN=4.3 mm IDIAMETER=31.29 mm F...	60.6571	17516.08	91.33461
22	DBEAN=4.8001 mm IDIAMETER=31.29 m...	57.56934	19910.72	90.8216
23	DBEAN=5.3 mm IDIAMETER=31.29 mm F...	54.57709	21977.62	90.37647
24	DBEAN=5.8001 mm IDIAMETER=31.29 m...	51.85046	23697.79	90.00433
25	DBEAN=6.3 mm IDIAMETER=31.29 mm F...	49.46865	25094.97	89.70094
26	DBEAN=6.8001 mm IDIAMETER=31.29 m...	47.42622	26224.02	89.45501
27	DBEAN=7 mm IDIAMETER=31.29 mm FI...	46.7555	26581.89	89.37692
28	DBEAN=3.3 mm IDIAMETER=26.21 mm F...	59.84484	10249.71	92.87393

Figure 21 Output

In Figure 21 (Output) the depiction shows the optimal solution with the pressures given at the wellhead and bottom, as well as the production rate.

Results of Different Analyses

Diameters of the surface choke										Tubing diameter					Model matching					
Diameter	**3,3**	3,8	4,3	4,8	5,3	5,8	6,3	6,8	7	Diameter	62	50,67	31,3	**26,2**	INPUT DATA			MODEL RESULTS		
	mm	mm	mm	mm	mm	mm	mm	mm	mm		mm	mm	mm	**mm**						
Qg m^3/d	**12301**	16624	21598	26798	32172	37609	42985	48198	50267	Qg m^3/d	12302	12760	11880	**10244**	Qg m3/d	12312		Qg m3/d	12301	
Pwh bar	**67,4**	68,7	69,8	70,1	69,9	69,4	68,5	67,5	67,1	Pwh bar	67,45	69,39	66,14	**59,85**	Pwh bar	65		Pwh bar	66,9	
Pbh bar	**92.4**	91.5	90.5	89.3	88.1	86.9	85.7	84.5	84,1	Pbh bar	92,44	93,34	92,53	**92,87**	Pbh bar	92,8		Pbh bar	92,9	

Diameters of the surface choke and tubing diameter																			
Diameter	3,3	3,8	4,3	4,8	5,3	5,8	6,3	6,8	7	3,3	3,8	4,3	4,8	5,3	5,8	6,3	6,8	7	3,3	**3,8**
	61,9	61,9	61,9	61,9	61,9	61,9	61,9	61,9	61,9	50,67	50,67	50,67	50,67	50,67	50,67	50,67	50,67	50,67	31,29	**31,29**
Qg m^3/d	12302	16618	21594	26795	32169	37606	42983	48195	50263	12760	17133	21861	26694	31563	36364	40947	45363	47057	11875	**14800**
Pwh bar	67,45	68,63	69,77	70,11	69,92	69,35	68,51	67,5	67,06	69,39	70,54	70,67	70,14	69,16	67,88	66,41	64,84	64,19	66,14	**64**
Pbh bar	92,44	91,52	90,46	89,33	88,14	86,94	85,72	84,52	84,04	92,34	91,41	90,4	89,35	88,28	87,21	86,17	85,17	84,78	92,53	**92**

Figure 22 Results of different analyses

Considering that this is a business project, the task is to select the optimal and profitable solution that would address the issue of liquid loading, maintain consistent production, and keep the bottom pressure stable.

6 CONCLUSION

The occurrence of liquid loading in gas wells is one of the most common and challenging problems encountered during exploitation. In this paper, we present possible solutions to the issue of liquid loading using the PipeSim program, which allows us to prevent or address the problem at the well through Nodal analysis.

The solutions outlined showcase various options, each with its own limitations or inadequacies for the specific conditions at the well. Therefore, this paper details all potential solutions for addressing the issue and ultimately identifies the most accessible and effective solution for resolving the problem. The first option defined as a possible solution for the liquid loading issue involves changing the diameter of the surface choke, but with the caveat of the system's limitations and the indication of reduced pressure at the bottom, which must be taken into account when selecting the choke diameter. The second option involves analyzing liquid loading to define LLGR and LLVR, addressing the liquid loading issue through chemical dosing. The third and fourth options suggest installing a tubing diameter of 31.29 mm and a choke diameter of 3.8 mm to resolve the liquid loading problem while maintaining production levels. Considering that this is a business project, the client has decided that the best option is to install a smaller diameter tubing and a larger diameter choke. As stated in the proposed analysis, the tubing diameter will be 31.29 mm, with the choke being 3.8 mm. With this combination of equipment, the well will no longer experience the issue of liquid loading.

REFERENCES

ABHULIMEN K.E. OLADIPUPO A. D (2022) Modelling of liquid loading in gas wells using a software-based

BEGGS H. D. 2008. “Production Optimization Using NodalTM Analysis”, 2nd ed. Columbia, Maryland, USA: Oil & Gas Consultants International.

GOOl VF, CURRIE PK (2008) “An improved model for liquid loading process in gas wells.” SPE Prod Oper. An Improved Model for the Liquid-Loading Process in Gas Wells | SPE Production & Operations | OnePetro

GOLAN M. WHITSON H. C. (1995) “Well Performance 2nd Edition”, Department of Petroleum Technology and Applied Geophysics, Norwegian University of Science and Technology.

GRAY, H. E. (1974) "Vertical Flow Correlation in Gas Wells". User manual for API 14B, Subsurface controlled safety valve sizing computer program. API.

IKPEKA P.M., OKOLO M.O. (2018) “Li and Turer Modified model for Predicting Liquid Loading in Gas Wells” Journal of Petroleum Exploration and Production Technology https://doi.org/10.1007/s13202-018-0585-6

HAN-YOUNG PARK, (2008) “Decision matrix for liquid loading in gas wells for cost/benefit analysis of lifting options” Submitted to the Office Graduate Studies of Texas A&M University

JOSEPH A. (2013) “Classification and Management of Liquid Loading in Gas Wells”, University of Port Harcourt

JAN-DIRK J. (2017) “Nodal Analysis of Oil and Gas Production Systems”, Society of Petroleum Engineers

JEŠIĆ M., MARTINOVIĆ B., STANČIĆ S., CRNOGORAC M., DANILOVIĆ D., (2023) “Mitigating hydrate formation in onshore gas wells”, Underground Mining Engineering

LEA, J.F., Bearden, J.L. (1999) On and Offshore Problems and Solutions. Paper SPE 52159 Mid-Continent Operations Symposium, Oklahoma City, Oklahoma, 28-31 March.

LEA, J., NICKENS, H., and WELLS, M. (2003) “Gas Well Deliquification“, Burlington, Massachusetts: Gulf Professional Publishing.

NALLAPARAJU YD., PANDIT D. (2012) “Prediction of Liquid loading in gas wells” SPE 155356, presented at the SPE annual technical conference and exhibition, San Antonio Texas. https://doi.org/10.2118/155356-MS

NWANKWO I. ABAKU G. KINATE B.B. (2020), "The Effect of Flow Parameters on Liquid Loading and Tubing Lift Performance in a Gas Condensate Well" International Journal of Recent Engineering Science (IJRES)

PIPESIM Version 2017.2 User Guide. PIPESIM User Guide. Copyright © 2017 Schlumberger

SOLESA, M., MARTINEZ, J.L., MARTINEZ, O.M. (2006) "Integrated Solution for Managing Liquid Loading Problem in Gas Wells of Burgos Fields." Schlumberger Private Report

SANKAR, S., & KARTHI, S. A. (2019). Study of identifying liquid loading in gas wells and deliquification techniques. *International Journal of Engineering Research and Technology (IJERT)*, *8*(6).

TURNER RG., HUBBARD MG., DUKLER AE. (1969) "Analysis and prediction of minimum low rate for the continuous removal of liquids from gas wells." J Petrol Technol. https://doi.org/10.2118/2198-PA (SPE–S219)

UNDERGROUND MINING ENGINEERING 46 (2025) 41-66 UDK 62
UNIVERSITY OF BELGRADE - FACULTY OF MINING AND GEOLOGY EISSN 2560-3337

Original scientific paper

COMPARATIVE ANALYSIS OF SURFACE INFRASTRUCTURE MODELS FOR AN OIL FIELD IN THE PANNONIAN BASIN: EVALUATION OF ASPEN HYSYS AND GAP SOFTWARE

Jelena Marković[1], Bojan Martinović[1], Nikola Zorić[1], Milica Ješić[1], Miroslav Crnogorac[2], Dušan Danilović[2]

Received: November 29, 2024 **Accepted:** January 10, 2025

Abstract: The Integrated Production Model (IPM) acts as a digital twin of the actual field, representing reservoir behavior, all wells and their equipment, as well as the entire surface infrastructure. This model allows for changes in parameters within the virtual environment, enabling the simulation of various scenarios to determine how these changes affect the entire system. Consequently, it is possible to select the most optimal scenario and validate its impacts. The development of the surface infrastructure model represents the final step in integrated production modeling, and this study focuses on creating a surface infrastructure model of an oil field in the Pannonian Basin using two software tools: Aspen HYSYS and Petroleum Experts - GAP. The goal is to compare the results obtained and identify the advantages and limitations of these software solutions. This analysis offers valuable insights into the capabilities of each program in simulating and optimizing oil operations. Engineers use a range of computational strategies and mathematical models to design and operate processing facilities. Aspen HYSYS is a widely recognized tool in the oil and gas industry for process simulation, allowing engineers to model various operational scenarios in detail and assess their impact on system performance. Aspen HYSYS is used for modeling the entire production process, including oil and gas processing, refining, and chemical plants, while GAP specializes in integrated asset modeling (IAM), modeling wells, flowlines, risers, and surface facilities, optimizing the entire production system from the reservoir to the processing plant. This paper first provides the theoretical background relevant to the research topic, including the basic concepts of process simulation in Aspen HYSYS and GAP. Following that, the research methodology is presented, including the steps of simulation and analysis. Finally, the simulation results are discussed, and conclusions are drawn regarding the applicability of both software tools for modeling surface infrastructure in oil fields.

Keywords: Integration Production Modeling, Oil and Gas Gathering and Stabilization, Aspen HYSYS, GAP – Petroleum Experts, Surface infrastructure

[1] STC NIS Naftagas doo, Narodnog fronta 12, 21000 Novi Sad
[2] University of Belgrade – Faculty of Mining and Geology, Djusina 7, Belgrade, Serbia

E-mails: jelena.dr.markovic@nis.rs; bojan.martinovic@nis.rs; nikola.n.zoric@nis.rs; milica.jesic@nis.rs; miroslav.crnogorac@rgf.bg.ac.rs, ORCID 0000-0002-8078-2684; dusan.danilovic@rgf.bg.ac.rs, ORCID 0000-0002-2969-040X

1 INTRODUCTION

The gathering station is one production facility at the oil field that serves as a gathering place for several liquids produced from production wells to measure the production flow rate (Madonna et al., 2022). The development of surface infrastructure models in the oil and gas industry is a crucial step toward process optimization, increasing efficiency, and reducing costs. The application of software tools such as HYSYS and GAP enables engineers to simulate various operational scenarios, analyze performance, and identify potential issues before they arise in actual operations.

HYSYS enables precise modeling of various phases in the production cycle, particularly the separation of oil, gas, and water. Based on simulations, it is possible to reduce costs and increase efficiency (Elkamel et al., 2003). GAP software integrates surface gathering system components with subsurface simulations and enables the optimization of oil and gas transport, which is particularly useful in complex production systems (Petroleum Experts, 2010).

Aspen HYSYS is used as an integrated process simulator in both steady-state and dynamic modes. The simulation models created in HYSYS are utilized for various purposes: plant design, performance monitoring, problem-solving, operational process improvement, business planning, and asset management. The software offers an integrated set of intuitive and interactive tools for simulation and analysis, as well as real-time applications. It provides rapid evaluations of safe and reliable designs through the quick creation of interactive models for "what-if" studies and sensitivity analyses (Guo et al., 2007).

GAP's robust calculation engine can optimize highly complex networks consisting of thousands of components, such as wells, pipelines, compressors, pumps, heat exchangers, and more, interconnected in any configuration, including intricate loops with multiple control points throughout the system. This flexibility is complemented by GAP's state-of-the-art optimization engine, which is considered the most powerful and fastest in the industry, utilizing advanced non-linear optimization techniques (Petroleum Experts, IPM13).

The development of the surface infrastructure model in GAP requires the prior creation of the reservoir model in MBAL and the models of all wells in the observed oil field using PROSPER. All of these software tools belong to the group of Petex software for integrated modeling. The first step involves the preparation and verification of input data on pipelines and the creation of a custom database in Excel, which facilitates the automatic generation of the GAP model. Using a Python script developed through OPENSERVER, the automatic creation of the GAP model is enabled, significantly simplifying the process of building the surface infrastructure model compared to the model in HYSYS. The created script allows for the connection of multiple objects, pipe

trimming and positioning, entry of data on wells and pipelines, pipe matching, and selection of the best correlation.

The following section provides a detailed description of the model development process in both software tools, including specific steps and methods used to optimize performance. Additionally, the results of the simulations are presented, offering insights into the efficiency and accuracy of each model, as well as an analysis that considers the advantages and disadvantages of the software solutions employed. Finally, conclusions are drawn that summarize the key findings and provide recommendations for future research and improvement of surface infrastructure models in the oil and gas industry.

2 METHODOLOGY

The analysis began with the development of a base model for the existing state of the surface infrastructure at oil field X using Aspen HYSYS and GAP software. When modeling surface infrastructure, it is crucial to accurately model the fluid, with the precision of the PVT model and the selection of the appropriate equation of state being the most important factors. To achieve alignment between the measured field data and the model data, the proper selection of correlations that describe pressure loss through the pipeline is essential.

The physical and chemical properties of crude oil vary significantly depending on the concentration of different types of hydrocarbons and minor constituents, as well as temperature and pressure. Accurate values of oil's physical properties and their changes during flow from the bottom of the well to the surface are essential as input data for fluid and heat transfer modeling (Martinović, 2022).

PVT properties of reservoir fluid are very important in petroleum engineering calculations, therefore, the accuracy of the calculations depends on the exactness of PVT properties. Ideally these properties are determined from laboratory analysis, of the samples (Kazemi, 2011).

A good PVT fluid model is crucial for successful modeling and simulation in the oil and gas industry.

In today's oil and gas industry, using a composite model and equation of state is increasingly important for accurately modeling the behavior of oil fluids. Black Oil correlations are typically used when limited information is available about the oil and gas in the system. The properties of oil and gas fluids are calculated from correlations with their specific weights, as well as several other easily measurable parameters (Honeywell, 2009).

The Black Oil fluid model assumes that the fluids consist only of liquid and gas phases, with the amount of gas dissolved in the oil depending on thermobaric conditions. The data necessary for creating the Black Oil fluid model includes: 1. oil density, 2. gas

density, 3. gas-to-oil ratio (GOR), and 4. water saturation. This data must be obtained from laboratory flash analysis—analysis of multi-stage evaporation (usually three phases). The sum of the gases released from each phase of the laboratory evaporation is known as the production GOR. The density of oil produced from the last stage of evaporation defines the density of oil in the reservoir. The analysis should be conducted under conditions closely related to the operating conditions in the field (Zhao Y., 2016; Al-Safran Eissa & Brill P. James, 2017).

Compositional PVT models are developed based on reservoir fluid compositions and reservoir temperature. The mole fractions of hydrocarbon components (C_1, C_2, C_3, C_4, nC_4, C_5, nC_5, C_6, C_7, C_8, C_9, C_{10}, C_{11} and C_{12+}) and non-hydrocarbon components (H_2S, CO_2 and N_2), molecular weight (MW) of C12 and specific gravity (Sp.Gr) of C_{12+} are usually measured in the reservoir fluid compositions test. These parameters and reservoir temperature are used to prediction of bubble point pressure Pb, solution gas to oil ratio on bubble point - Rsb and formation volume factor for oil at bubble point – Bob (Kazemi, 2011).

When comparing Black Oil and the composite fluid model, it is evident that the composite model has greater accuracy in predicting the fluid properties of the hydrocarbon mixture. On the other hand, the Black Oil model requires only a few input data points (Mittbock, 2014). Due to the limitations of input data, the fluid model in the simulation was constructed as Black Oil.

The components that make up the oil were taken from the well model in PROSPER and selected when creating the component list, which effectively represents a starting step in the simulation itself. Pure components and pseudocomponents were selected based on the following parameters: critical temperatures, pressures, and volumes, molar masses, and acentric factors—as one of the parameters that provide information about the degree of polarization and interactions among molecules.

The equation of state is used to describe the thermodynamic behavior of fluids and enables engineers to understand and predict how fluids will behave under different conditions of pressure, temperature, and volume.

Equations of State (EoS) are becoming more prevalent for modeling the fluid properties of crude oil and gas reservoirs, providing a more accurate prediction of fluid behavior compared to traditional black oil models (Almehaideb et al, 2000).

In 1873, van der Waals proposed an EOS that represented non-ideal behavior by accounting for finite volumes occupied by molecules of substances and the repulsive and attractive forces between these molecules. The van der Waals EOS is shown as:

$$\left(p + \frac{a}{V^2}\right)(V - b) = RT \tag{1}$$

In Eq. 1, p is pressure; V is volume; T is temperature; a is the attraction parameter to correct pressures for attraction between molecules; b is the effective molecular volume to correct for volume occupied by the molecules; and R is the universal gas constant.

The equation of state applied in both software is the Peng-Robinson equation, which will be elaborated on later.

In 1976, Peng and Robinson introduced a new two-parameter equation of state developed primarily to improve calculations in the vicinity of the critical region and improve calculation of liquid densities. The PR EOS (Eq. 2) is expressed as:

$$p + \frac{\alpha(T,\omega)}{V(V+b)+b(V-b)} = \frac{RT}{V-b} \tag{2}$$

α – shape parameter in gamma function

ω – acentric factor. (Ezekwe, 2010)

The Peng-Robinson equation of state was used, which is applicable to single-component systems for defining the partial pressure of a component and its volumetric state. However, it is also utilized in two-phase or multiphase systems to describe the phase behavior of the observed thermodynamic system. This equation is an improved model of the Soave-Redlich-Kwong equation of state and demonstrates its greatest advantage in defining the density of the liquid phase (Grubač, 2019).

The advantage of using it in the simulation package is that it represents the most advanced model in Aspen HYSYS, providing high accuracy over a wide range of temperatures and pressures (Zhao, 2016). Additionally, the Peng-Robinson equation of state is also employed in GAP software.

2.1 Data Collection

All necessary data for creating the model were obtained from the technical regime in Šahmatka for April 2024. To create a model of the surface infrastructure in GAP, it is first necessary to develop the reservoir model in MBAL and the well models in PROSPER.

In this process, it is essential to collect data on oil, gas, and water production (Tables 1, 2, and 3), as well as pressures for a specific date that will be used to create the model. Additionally, data on pipelines, including their lengths and diameters, must be gathered from the pipeline database and GIS (Tables 4, 5, 6).

An Excel table has been created, customized for automatic data input into GAP through OPENSERVER, utilizing a developed Python script.

In addition to the previously mentioned data, it is necessary to enter the components that constitute the oil in HYSYS. The oil composition includes components C1 to C50+. For HYSYS, due to modeling fluids as Black Oil, the gas composition input is also required (Table 7).

Furthermore, data on oil density, gas specific gravity, water salinity, and the molar fraction of non-hydrocarbon components—H_2S, CO_2, and N_2 (Table 8)—are required. For the HYSYS model, the input of viscosity variation with temperature is necessary due to working with the Black Oil model of fluid, and this data is provided in Table 9.

All well pipelines connecting the wells at GS-1 and GS-2 are made of pipe material Φ73 mm x 5.2 mm API STD 5L GRADE B, buried and protected against corrosion. The fluid is transported via pipeline from GS-2 to GS-1, where the process of separating the liquid from the gas phase occurs, along with the dehydration of oil and its preparation for shipment, as well as the disposal of formation water into designated wells. The extracted dissolved gas is further prepared and delivered to end consumers, including shipments to JP Srbijagas, as well as for the operation of a cogeneration plant where electricity is produced.

The following tables present the input data that were used for model development.

Table 1 Input data for gathering station 1

Serial number	Parameter	Unit of measure	AMU-1	AMU-2	AMU-3	AMU-4	AMU-5
1	Qf	m^3/day	268	304	178,2	201	398,2
2	Qo	m^3/day	31	51	50	40,692	82,113
3	Qg	m^3/day	60	574	65	856	1248
4	p	bar	500	480	490	580	547
5	T	degC	20	20	20	20	20

Table 2 Input data for gathering station 1

Serial number	Parameter	Unit of measure	AMU-6	AMU-7	AMU-8	AMU-9	AMU-10
1	Qf	m^3/day	187,3	156,8	187,5	225,3	126,2
2	Qo	m^3/day	31,847	30,05	34,684	41,788	25,234
3	Qg	m^3/day	280	839	967	1464	427
4	p	bar	594	500	500	500	670
5	T	degC	20	20	20	20	20

Table 3 Input data for gathering station 2

Serial num.	Para-meter	Unit of measure	AMU-1	AMU-2	AMU-3	AMU-4	AMU-5	AMU-6	AMU-7
1	Qf	m^3/day	220,7	220,2	202,7	315	327	159,7	413
2	Qo	m^3/day	49,11	51,63	39,67	55,46	67	33,34	116
3	Qg	m^3/day	801	861	1160	914	104	2372	1521
4	p	bar	676	682	679	696	682	1063	976
5	T	degC	20	20	20	20	20	20	20

Table 4 Input data for pipelines on GS-1

Gathering station 1 (GS-1)							
Serial num.	**Parameter**	**Unit of measure**	**AMU-1**	**AMU-2**	**AMU-3**	**AMU-4**	**AMU-5**
1	Pipe length	m	10	10	10	530	130
2	Internal diameter of the pipeline	mm	156,3	156,3	156,3	156,3	156,3
3	Wall thickness	mm	6	6	6	6	6

Table 5 Input data for pipelines on GS-1

Gathering station 1 (GS-1)							
Serial num.	**Parameter**	**Unit of measure**	**AMU-6**	**AMU-7**	**AMU-8**	**AMU-9**	**AMU-10**
1	Pipe length	m	165	55	35	18	700
2	Internal diameter of the pipeline	mm	156,3	156,3	156,3	156,3	156,3
3	Wall thickness	mm	6	6	6	6	6

Table 6 Input data for pipelines on GS-2

Gathering station 2 (GS-2)									
Serial num	**Parameter**	**Unit of measure**	**AMU-1**	**AMU-2**	**AMU-3**	**AMU-4**	**AMU-5**	**AMU-6**	**AMU-7**
1	Pipe length	m	15	15	15	15	15	650	10
2	Internal diameter of the pipeline	mm	156,3	156,3	156,3	156,3	156,3	156,3	116
3	Wall thickness	mm	6	6	6	6	6	6	6

Table 7 Component composition of gas

Parameter	**Unit of measure**	**C1**	**C2**	**C3**	**iC4**	**nC4**	**iC5**	**nC5**	**C6**	**C7**	**N2**	**CO2**
Component participation	mol %	87	3,23	0,3	0,04	0,02	0,02	0,01	0,03	0,02	4,49	4,89

Table 8 Viscosity at standard conditions – input for Hysys

Serial number	**Parameter**	**Unit of measure**	**Value**			
1	Temperature	degC	25	35	45	60
2	Viscosity at standard conditions	mm	96,93	55,1	34,5	19,3

Table 9 PVT characteristics of fluids

Serial number	**Parameter**	**Unit of measure**	**Value**	**Parameter**
1	ρ_o	kg/m^3	914	ρ_o - oil density
2	ρ_{gr}	ρgr	0,687	ρ_{gr} - gas gravity
3	Water salinity	ppm	6221,8	Water salinity
4	Molar percentage H_2S	mol %	0	Molar percentage H_2S
5	Molar percentage CO_2	mol %	4,88	Molar percentage CO_2
6	Molar percentage N_2	mol %	4,49	Molar percentage N_2

2.2 Creating and matching the model

Simulation is the process of creating an operational model of a system and conducting experiments on that model to understand the system's behavior or evaluate alternative strategies for its development and operation.

Models of the surface infrastructure for oil field X were created using Aspen HYSYS and GAP software, and the process of developing the models is described below.

Modeling in HYSYS

Considering that it is heavy oil composed of fractions up to C50+, the hydrocarbon components with more than 10 carbon atoms were grouped into pseudocomponents based on critical conditions: pressure, temperature, volume, acentric factor, etc., and entered into the software accordingly (Figure 1).

After defining the components that make up the oil, the next step involves selecting a thermodynamic model, i.e., an equation of state. Equations of state were developed to provide a mathematical relationship between pressure, volume, and temperature. Initially, they were introduced as a method to interpret the non-ideal nature of many pure substances. Later, the role of equations of state expanded to include the prediction of properties for both simple and complex mixtures. The equations used in PVT analysis are derived from the Van der Waals equation. In the software, the Peng-Robinson equation of state was used (Petroleum Experts, 2011).

The material streams, which represent automatic measuring units in the simulation, were modeled based on data on fluid production, system pressure, and temperature. Given that the base model was created using the Black Oil fluid model, input on the gas-to-oil ratio (GOR), water-to-oil ratio (WOR), water cut, oil density, viscosity changes with temperature, and the PVT composition of gas obtained from laboratory tests in the "oil and gas feed" section was also required. Based on the input data, the software independently calculated the molar fraction of each individual component in the fluid. Figure 2 shows the method of defining material streams in HYSYS and in Figure 3, the data input window for the Black Oil fluid model is shown.

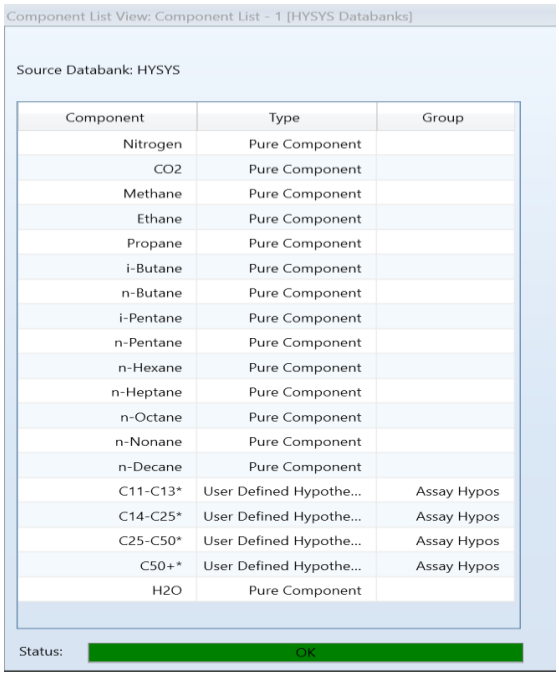
Component List View: Component List - 1 [HYSYS Databanks]

Source Databank: HYSYS

Component	Type	Group
Nitrogen	Pure Component	
CO2	Pure Component	
Methane	Pure Component	
Ethane	Pure Component	
Propane	Pure Component	
i-Butane	Pure Component	
n-Butane	Pure Component	
i-Pentane	Pure Component	
n-Pentane	Pure Component	
n-Hexane	Pure Component	
n-Heptane	Pure Component	
n-Octane	Pure Component	
n-Nonane	Pure Component	
n-Decane	Pure Component	
C11-C13*	User Defined Hypothe...	Assay Hypos
C14-C25*	User Defined Hypothe...	Assay Hypos
C25-C50*	User Defined Hypothe...	Assay Hypos
C50+*	User Defined Hypothe...	Assay Hypos
H2O	Pure Component	

Status: OK

Figure 1 Component List (Aspen Hysys V12)

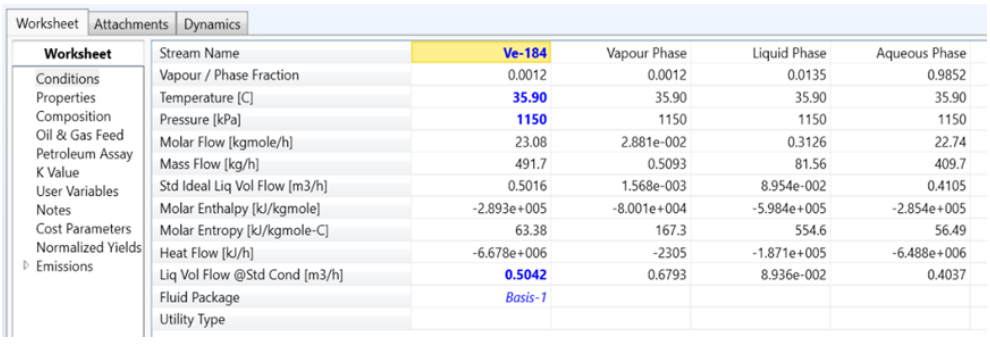
Worksheet | Attachments | Dynamics

Worksheet
- Conditions
- Properties
- Composition
- Oil & Gas Feed
- Petroleum Assay
- K Value
- User Variables
- Notes
- Cost Parameters
- Normalized Yields
- Emissions

Stream Name	Ve-184	Vapour Phase	Liquid Phase	Aqueous Phase
Vapour / Phase Fraction	0.0012	0.0012	0.0135	0.9852
Temperature [C]	35.90	35.90	35.90	35.90
Pressure [kPa]	1150	1150	1150	1150
Molar Flow [kgmole/h]	23.08	2.881e-002	0.3126	22.74
Mass Flow [kg/h]	491.7	0.5093	81.56	409.7
Std Ideal Liq Vol Flow [m3/h]	0.5016	1.568e-003	8.954e-002	0.4105
Molar Enthalpy [kJ/kgmole]	-2.893e+005	-8.001e+004	-5.984e+005	-2.854e+005
Molar Entropy [kJ/kgmole-C]	63.38	167.3	554.6	56.49
Heat Flow [kJ/h]	-6.678e+006	-2305	-1.871e+005	-6.488e+006
Liq Vol Flow @Std Cond [m3/h]	0.5042	0.6793	8.936e-002	0.4037
Fluid Package	Basis-1			
Utility Type				

Figure 2 Defining material streams in Hysys (Aspen Hysys V12)

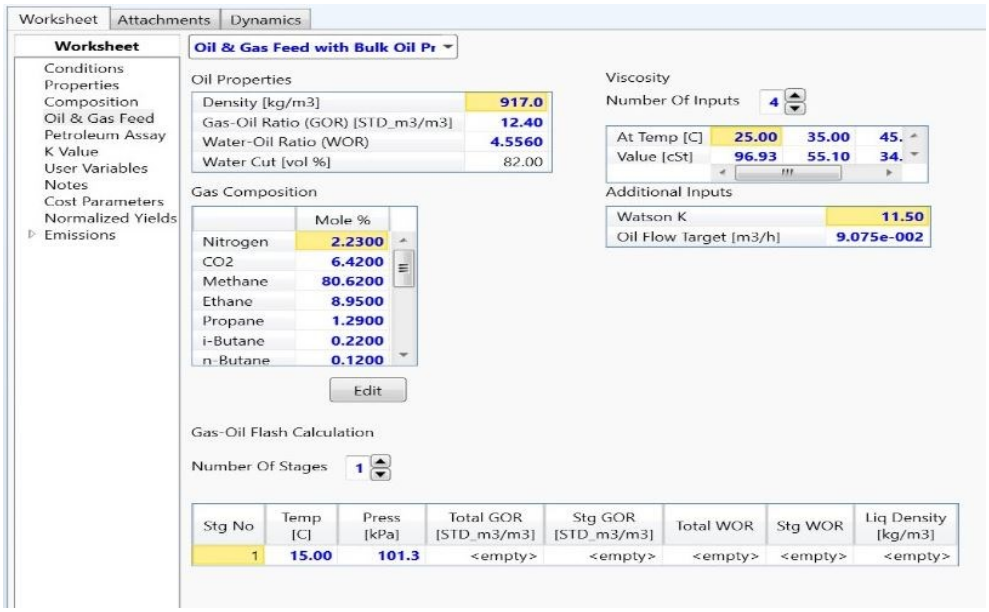

Figure 3 Defining material streams in HYSYS (Aspen Hysys V12)

The pipelines were modeled based on data regarding their length and diameters – both internal and external (Figure 4). This data was obtained from the pipeline database. The heat transfer coefficient (Figure 5) was determined using the "Estimate HTC" option based on data on burial depth and ambient temperature, as well as the soil composition at the burial depth, which is moist clay – data from the Republic Hydrometeorological Institute.

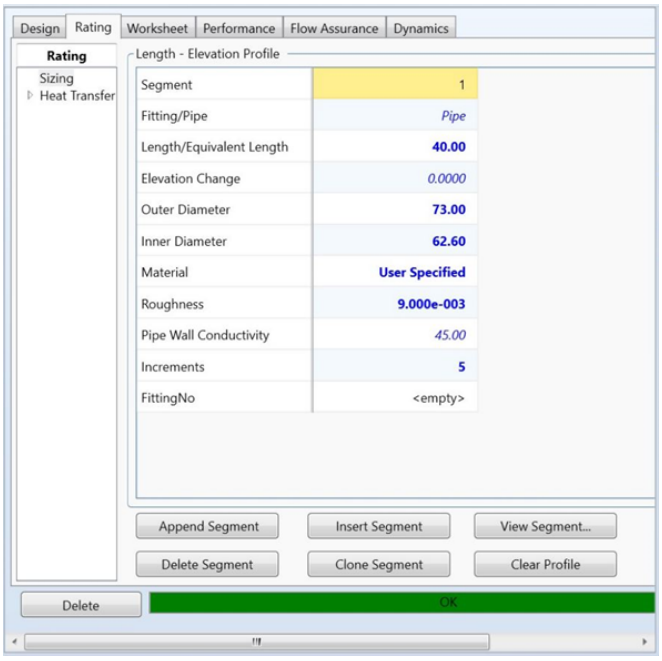

Figure 4 Defining pipelines in HYSYS (Aspen Hysys V12)

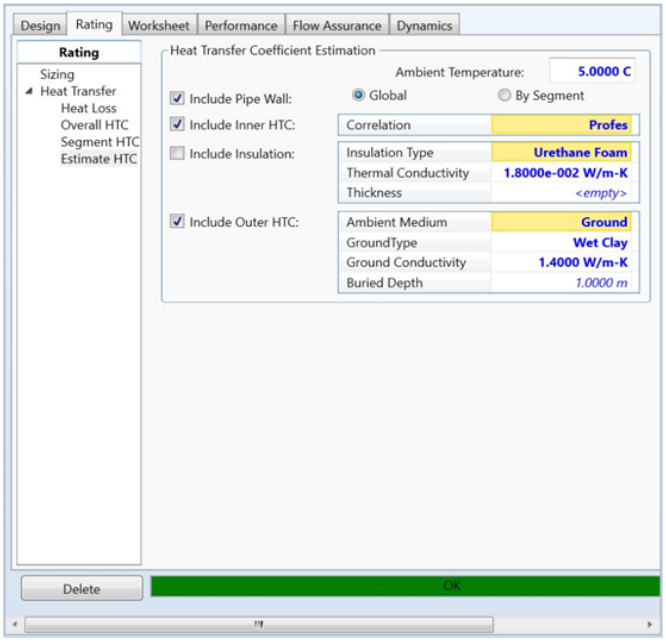

Figure 5 Calculation of the heat transfer coefficient (Aspen HYSYS V12)

Figure 6 shows the window in the software Aspen Hysys for selecting correlations.

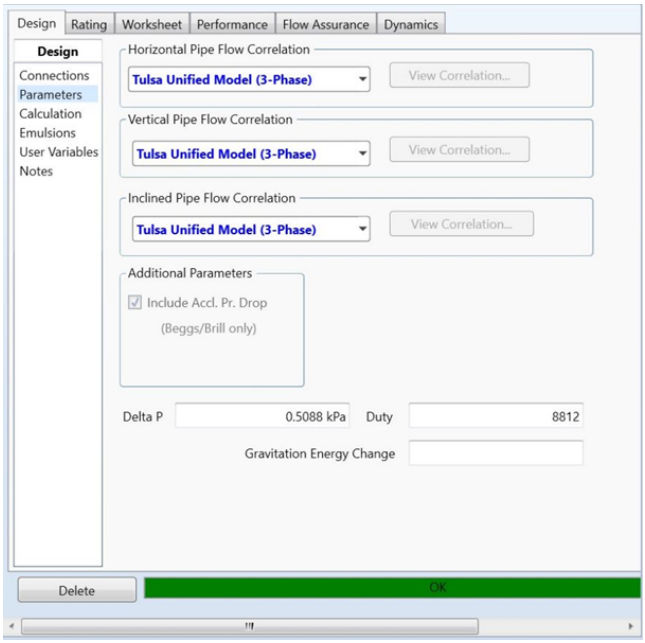

Figure 6 Selecting correlations for pipelines (Aspen Hysys V12)

By selecting the appropriate correlations, it was possible to achieve a match between the measured values from the field and the results of the base model. For this reason, special attention must be paid to the correlations. At the end of this chapter on models, the theoretical basis of the correlations used to define pressure drop through the pipeline in both software programs is presented.

In Figure 7, the base model of the surface infrastructure for oil field X created in Aspen HYSYS software is shown.

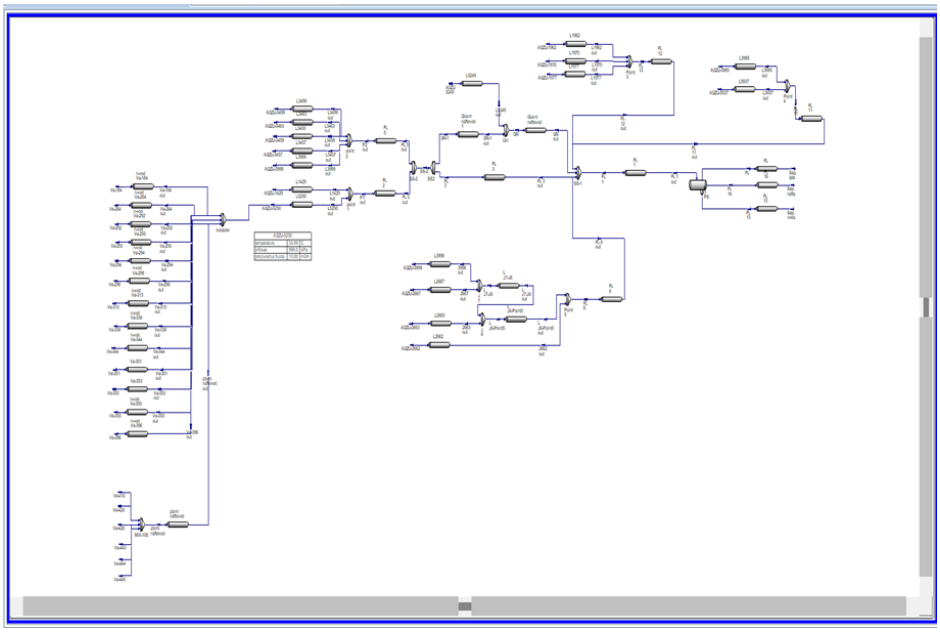

Figure 7 Base model of the surface infrastructure for oil field X (Aspen HYSYS V12)

Modeling in GAP

Before creating the surface infrastructure model in GAP, it is necessary to develop the reservoir model in MBAL and the well model in PROSPER, generate VLP tables from the well model, and import everything into GAP. The data required for the surface infrastructure model was obtained from the Pipeline Database (data on the diameter and length of pipelines), production data by well from the Sahmatka, pressure data from the SCADA system, and the GIS Odeon (pipeline situational map).

In this software, the Black Oil fluid model and the Peng-Robinson equation of state were also used.

The measured field data on pressures and production by wells, obtained from the Production Worksheet, are entered into the created skeleton of the surface infrastructure, which consists of wells, pipelines, and separators. To achieve a match between the model and the measured data, the correlation parameters that define the pressure drop through the pipeline are adjusted.

Figure 8 shows part of the surface infrastructure of this oil field, specifically one automatic measurement unit to which 16 wells are connected.

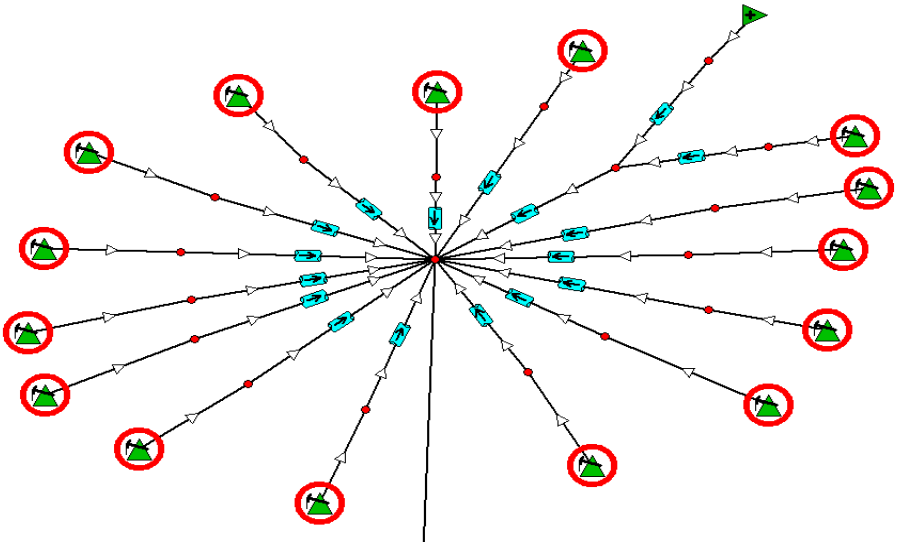

Figure 8 Automatic measurement unit – part of the surface infrastructure (GAP IPM13)

Figure 9 shows the input window for wells in the software – the corresponding PROSPER file with the previously created well model and the VLP table extracted from the model is imported.

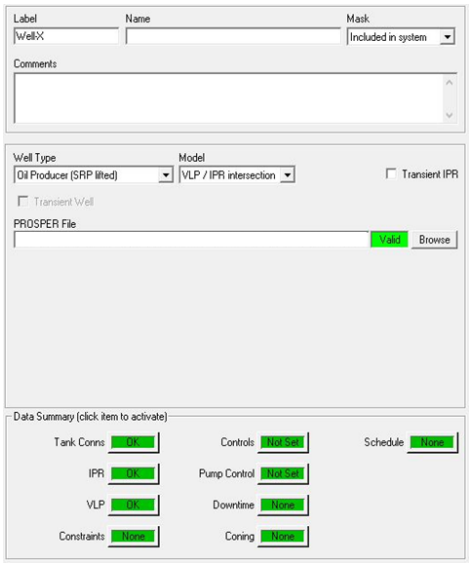

Figure 9 Input data for wells (GAP IPM13)

For pipelines, it is necessary to enter the length, diameter, roughness in the description window (Figure 10).

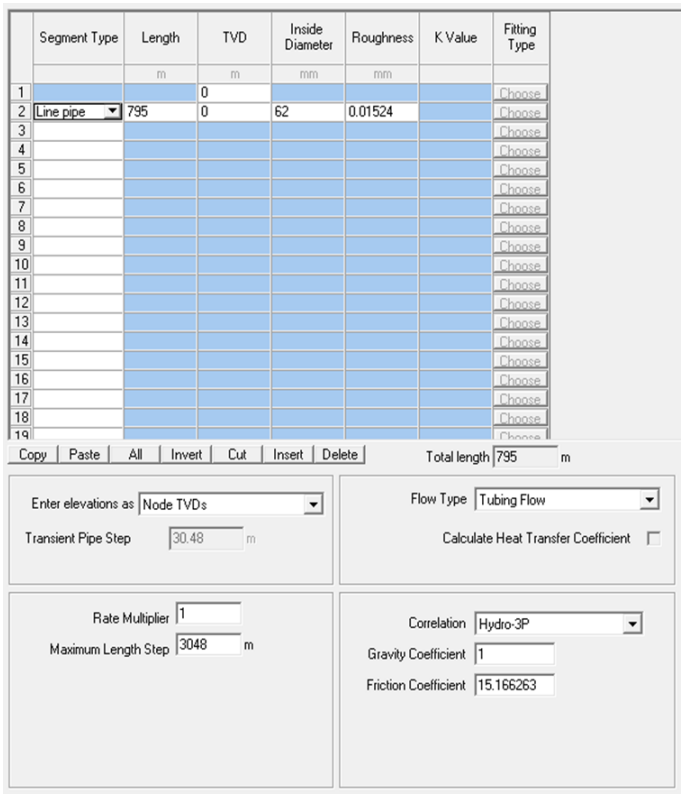

Figure 10 Description window for pipeline (GAP IPM13)

It is also necessary to enter the parameters for achieving a match between the model and the facts: molar fractions of nitrogen, carbon dioxide, and hydrogen sulfide, relative gas density, gas-oil ratio, water salinity, and inlet and outlet pressure in the matching window (Figure 11).

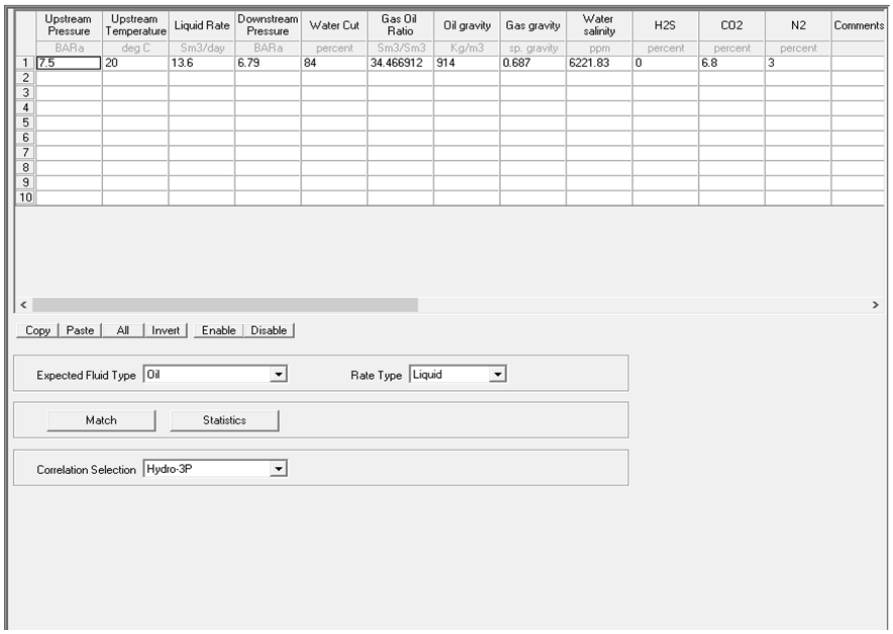

Figure 11 Matching window for pipeline (GAP IPM13)

Since there was an existing surface infrastructure model for oil field X in GAP, an update of that model was performed for April 2024. All necessary data has been entered into a unified Excel database, where, through the development of Python code, automatic data transfer to the model is carried out via OPENSERVER. This enables automatic communication between OPENSERVER and GAP.

The operational parameters of the wells in GAP have been updated, IPR data in PROSPER have been adjusted, new well models that were not included in the base model have been created, and changes in equipment in existing models have been made if maintenance is conducted. A review and verification of the production parameters of the wells have been performed, and all PROSPER models, as well as the necessary parameters in the GAP model, have been updated.

Models of gathering stations with corresponding wells for GS-1 and GS-2 have been created. Fluid is transported from GS-2 to GS-1 via two pipelines, and the station operates in a flow-through manner. GS-1 is equipped with a separation system where, after separation, gas and oil are transported further through separate pipelines.

A base model has been created with 248 wells that were operational on April 14th, 2024.

Figure 12 shows the surface infrastructure model of oil field X created in GAP software.

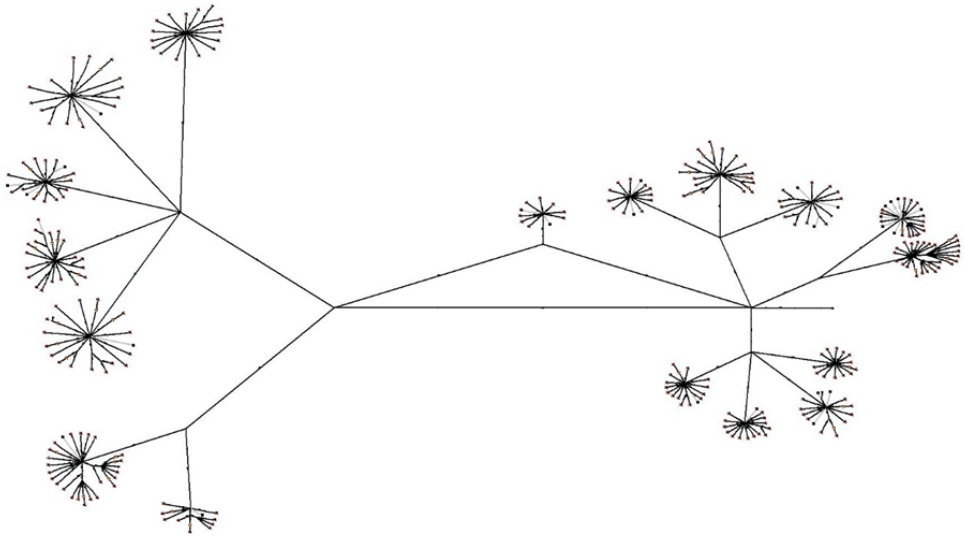

Figure 12 Base model of surface infrastructure of oil field X in GAP (GAP IPM13)

Model matching

The behavior of multiphase flow is significantly more complex compared to single-phase flow. When gas and liquid flow simultaneously, they tend to segregate due to variations in fluid properties. These fluids will experience different shear stresses as a result of their differing densities and viscosities (Brill and Mukherjee, 1999).

In the oil industry, multiphase flow models are often used to simulate the flow from the reservoir to the production unit. Flow simulations help monitor production and optimize processes to support decision-making. Despite the need for accurate simulations that support production operations, multiphase flow models are primarily developed using laboratory data and are rarely validated under field conditions (Chaves et al, 2022 & Xiao et al, 1990).

By matching pressure losses through the pipeline, an accurate integrated model is developed, starting from the reservoir, passing through the wells, gathering systems, and reaching the production separator.

It's crucial to carefully approach the pipeline matching process, especially when dealing with multiphase flows through long, undulating pipelines where field measurements have been taken over considerable distances. Pressure measurements may not align with production data due to the combined effects of fluid compressibility and the time required for the fluid to travel between measurement points.

The correlations used to achieve alignment with the measured data are: Beggs and Brill, Hydro 3P, and Petroleum Experts 5 in GAP, as well as Tulsa 3 Phase and Beggs and Brill in HYSYS. The following describes the correlations used.

The Beggs and Brill equation, first introduced in 1973 and later improved in 1979, is applicable to pipelines in horizontal, vertical, and inclined positions. This equation accounts for pressure drop due to friction and hydrostatic pressure changes. The first part of the equation addresses the determination of flow pattern and liquid holdup, followed by the calculation of the densities of the liquid and gas phases. Based on this, along with the flow pattern, the hydrostatic pressure drop is determined (Beggs & Brill, 1973).

Initially, the pipe was positioned horizontally, and the flow rates were adjusted to observe all horizontal flow patterns. Afterward, the inclination of the pipe was altered, allowing for the measurement of liquid holdup (HL(θ)) and pressure drop. This setup enabled the study of the effect of inclination on holdup and pressure drop. Beggs and Brill proposed the following equation for the pressure gradient (Eq. 3)

$$\frac{dp}{dL} = \frac{\frac{f\rho_n {v_m}^2}{2d} + \rho_m g sin\theta}{1 - Ek} \tag{3}$$

where Ek, dimensionless kinetic-energy pressure gradient, is defined by (Eq. 4)

$$Ek = \frac{v_m v_{SG} \rho_n}{p} \tag{4}$$

and mixture density should be calculated as (Eq. 5):

$$\rho_m = \rho_L H_{L(\theta)} + \rho_G \left[1 - H_{L(\theta)}\right] \tag{5}$$

Liquid holdup and friction factor should be found as described in the following.

Gravity forces act on the liquid, causing a decrease in the liquid velocity and thereby slippage and holdup is increased. By further increasing of the angle, liquid covers the entire cross section of the pipe. The slippage between the phases is reduced and liquid holdup reduces. Beggs and Brill observed that degree of holdup with angle varied with flow rates. To include effects of pipe inclination, it was decided to normalize liquid holdup. The following equation was proposed (Eq. 6):

$$\Psi = \frac{H_{L(\theta)}}{H_{L(0)}} \tag{6}$$

where Ψ is inclination correction factor, HL(θ) is holdup at angle θ from horizontal, and HL(0) is horizontal holdup (Fossmark, 2011).

On the other hand, the Tulsa 3 Phase correlation provides a unique methodology for hydrodynamic calculations, allowing for the prediction of flow patterns, pressure drop, holdup, and even the characteristics of slug flow in multiphase fluids. This model is

applicable in horizontal, vertical, and inclined pipelines. The first step in solving the equation is defining the fluid flow pattern, followed by calculating the pressure drop through the system using the appropriate relationships (Grubač, B. 2019).

The TUFFP unified model for gas/liquid flow in pipes was designed to predict transitions between flow patterns, pressure drop, liquid holdup, and slug properties across all inclination angles from -90° to +90° relative to horizontal. The TUFFP unified model is based on the dynamics of slug flow. Because slug flow has transition boundaries with all other flow patterns, the equations of slug flow can be used not only to calculate the slug characteristics, but also to predict transitions from slug flow to other flow patterns. Therefore, flow pattern transitions and other hydrodynamic behaviors are all calculated within a single model. Oil and water can be found as a fully mixed pseudo-single-phase in a slug body and in bubbly, dispersed, bubble and annular flow. On the other hand, they may not be fully mixed, and the local holdups may not be the same as the input fractions. Presumably, the continuous phase is slower than the dispersed phase due to its contact with the pipe wall. The relative velocity between the continuous phase and the dispersed phase needs to be modeled under different flow conditions. As mentioned above, if the oil and water are fully separated, like in stratified flow or in the film region of slug flow, then the flow can be modeled with the three-layer approach. The model for predicting the transition from stratified to dispersed liquid-liquid flow can be developed based on the local turbulent intensity and the physical properties of the liquid phases. (Sarica & Zhang, 2006; Zhang et al, 2003; Al-Safran & Brill, 2017).

The upgraded Petroleum Experts 5 mechanistic correlation improves upon the previous Petroleum Experts 4. While PE4 exhibited instabilities (like other mechanistic models) that restricted its use, PE5 minimizes these issues by using a calculation approach that avoids flow regime maps as a starting point.

PE5 can model any type of fluid flow through various well or pipeline paths. It accounts for fluid density changes along both upward and downward trajectories.

Additionally, well stability can be assessed using PE5 by calculating gradient profiles, which also enable the modeling of liquid loading, slug frequency, and more (Fetoui, I. 2017).

The multiphase flow correlation is suitable for predicting and analyzing the behavior of three-phase flow in pipelines and wells. Applicable to both gas and oil fields, the "Hydro-3P" correlation offers accurate predictions for horizontal pipeline simulations across various flow regimes. It is particularly well-suited for stratified and annular flows, but it can also handle other flow regimes encountered in multiphase flow systems.

3 RESULTS AND DISCUSSION

The fluid production at the GS-1 facility, Field X, on April 14th, 2024, amounted to approximately 2233 m³/day, with a water cut of 83.1%. Oil production on that date was 398 m³/day, and gas production was 6780 m³/day.

In the base model in HYSYS, the fluid production at GS-1 is 2159.8 m³/day, of which 396 m³/day is oil. The percentage difference in fluid production between the base model and actuals is 1.66%, the oil production difference is 0.52%, while the pressure difference at GS-1 is 0.21%. In the actuals, the pressure at GS-1 is 4.69 bar, while in the base model it is 4.68 bar.

On the other hand, the differences between the base model and actuals at GS-1 in GAP are as follows:

- Fluid production: $\Delta Qf = 3.06\%$;
- Oil production: $\Delta Qn = 4.52\%$;
- Pressure at GS-1: $\Delta p = 1.07\%$.

At GS-1 and GS-2, the temperature, according to actual data, varied between 19 and 22°C on the date the data was analyzed. A temperature value of 20°C was used as input for the models. In the HYSYS model, only the arithmetic value of the input temperatures can be obtained, slightly reduced due to the roughness of the pipelines through which the fluid flows and the chosen correlations, so the model was not matched based on temperature data.

Fluid production at GS-2, according to the actual data, is 1858.9 m³/day, with oil production around 411.94 m³/day. In the base model in HYSYS, the production values are as follows: fluid 1853.1 m³/day, oil 411.12 m³/day, and gas 7733 m³/day.

In the base model in HYSYS, the fluid production at GS-2 is 1853.1 m³/day, of which 411.12 m³/day is oil. The percentage difference in fluid production between the base model and actuals is 0.31%, oil production differs by 0.2%, while the pressure difference at GS-2 is 3.33%. In the actuals, the pressure at GS-2 is 6.3 bar, while in the base model it is 6.09 bar.

On the other hand, the differences between the base model and actuals at GS-2 in GAP are as follows:

- Fluid production: $\Delta Qf = 2.32\%$;
- Oil production: $\Delta Qn = 4.96\%$;
- Pressure at GS-2: $\Delta p = 4.44\%$.

These deviations of the base model from the actual data in both software platforms are also presented in tabular form (Tables 10, 11 12 and 13), where the differences in values, not just the percentage deviations, can be observed.

Since all deviations are within the allowable limits of ±10%, the models in both software platforms are considered valid and can be used for various simulations and for monitoring system behavior due to certain changes made to optimize the process of crude oil and gas separation, storage, and transport.

Table 10 Value deviation of the model from the fact

Serial number	Parameter	Unit of measure	Hysys	Gap	Fact
1	Q_f	m^3/day	2159,8	2164,6	2254
2	Q_o	m^3/day	395,92	380	398
3	Q_g	m^3/day	6260	7272	6780
4	Q_w	m^3/day	1799,88	1784,6	1856
5	P_{GS-1}	kPa	468	464	469
6	T	degC	20	20	20

Table 11 Value deviation of the model from the fact

Serial number	Parameter	Unit of measure	Hysys	Gap	Fact
1	Q_f	m^3/day	1853,1	1815,8	1858,9
2	Q_o	m^3/day	411,12	391,5	411,94
3	Q_g	m^3/day	6609,6	7385	7733
4	Q_w	m^3/day	1442	1424,3	1446,96
5	P_{GS-2}	kPa	609	602	630
6	T	degC	18,84	20	20

Table 12 Percentage deviation of the model from the fact on GS-2

Gathering station 1						
Serial number	**Unit of measure**	**Parameter**	**Hysys**		**Gap**	
			Δ	**Δ(%)**	**Δ**	**Δ(%)**
1	m^3/day	Q_f	-37	1,66	-68	3,06
2	m^3/day	Q_o	-2	0,52	-18	4,52
3	m^3/day	Q_g	-520	7,67	492	7,26
4	m^3/day	Q_w	-56,12	3,02	-71,4	3,85
5	kPa	P_{GS-1}	-1	0,21	-5	1,07
6	degC	T	0	0	0	0

Table 13 Percentage deviation of the model from the fact on GS-2

Gathering station 2						
Serial number	**Unit of measure**	**Parameter**	**Hysys**		**Gap**	
			Δ	**Δ(%)**	**Δ**	**Δ(%)**
1	m^3/day	Q_f	-6	0,31	-43	2,32
2	m^3/day	Q_o	-1	0,2	-20	4,96
3	m^3/day	Q_g	-923	9,53	-348	4,5
4	m^3/day	Q_w	-20,33	1,39	-38	2,6
5	kPa	P_{GS-1}	-21	3,33	-28	4,44
6	degC	T	-1,16	5,8	0	0

4 CONCLUSION

In this paper, a comparative analysis of the software solutions HYSYS and GAP for modeling the surface infrastructure of oil field in the Pannonian Basin is conducted.

Error analysis shows that both software solutions provide reliable estimates, with deviations within acceptable limits of ±10%. At Gathering Station 1, HYSYS displayed a deviation of -37 m³/day for the parameter Qf, with a percentage error of 1.66%, while GAP had a deviation of -68 m³/day, with a percentage error of 3.06%. These deviations indicate that HYSYS provides more precise results for this parameter. Regarding oil production (Qo), HYSYS had a minimal deviation of -2 m³/day (0.52%), while GAP showed a larger deviation of -18 m³/day (4.52%), further confirming HYSYS provides better accuracy in its estimates.

However, in the analysis of gas production (Qg), GAP had a deviation of 492 m³/day with a percentage error of 7.26%, while HYSYS recorded a significantly larger negative

deviation of -520 m³/day (7.67%), suggesting greater reliability of GAP for this parameter.

At Gathering Station 2, the results also showed similar trends. HYSYS had a deviation of -6 m³/day for Qf, corresponding to an error of 0.31%, while GAP had a deviation of -43 m³/day (2.32%). In terms of gas production (Qg), HYSYS had a larger deviation of -923 m³/day, with a percentage error of 9.53%, while GAP recorded a deviation of -348 m³/day (4.5%), indicating greater accuracy for GAP in this segment.

HYSYS excelled in estimates related to oil and fluid production, while GAP was more successful in analyzing gas production. This complementarity suggests that both tools can be used together to provide a comprehensive picture of the surface infrastructure system. It is recommended to use HYSYS when there are time constraints for model development, as it allows for modeling wells as material streams within the software itself. This functionality significantly reduces the time required for model development, making it suitable for quick analyses and simulations. On the other hand, GAP requires the initial creation of the model for the reservoir and all wells, which can significantly extend the modeling time.

The results indicate that HYSYS offers detailed simulation capabilities for the entire production process, whereas GAP offers integrated asset modeling that optimizes interconnected systems. The advantages of HYSYS include its versatility in various operational scenarios, while GAP excels various operational scenarios.

The comparison between HYSYS and GAP highlights that HYSYS is more suited for complex process simulations, while GAP excels in specific flow applications. HYSYS provides advanced capabilities for modeling multiphase flows, whereas GAP has limitations in this area. The user-friendly interface of HYSYS makes it easier for engineers to conduct simulations, while GAP requires a higher level of technical expertise. In terms of optimization and performance analysis, HYSYS offers broader options, while GAP focuses on specific flow calculations. Results obtained from HYSYS can be easily validated against real-world data, thanks to its advanced algorithms, whereas GAP is accurate for predefined scenarios. Additionally, HYSYS integrates well with various process units, while GAP is primarily geared toward pipeline flow analysis.

Overall, HYSYS is more applicable to refinery and chemical processes, while GAP is tailored for the oil and gas industry. Lastly, HYSYS tends to demand more resources and is better suited for larger systems, whereas GAP is simpler and more efficient for smaller-scale applications.

These findings are significant for the oil and gas industry, as they assist in selecting the most suitable software depending on the specific project needs. Further research is recommended to explore additional functionalities of these tools and their integration with modern technologies.

HYSYS allows engineers to explore various operational scenarios and optimize process units. On the other hand, GAP provides integrated modeling that focuses on analyzing the interconnections within the network, enabling the identification of potential bottlenecks and a better understanding of pipeline dynamics.

Although this study did not include optimization, the simulation results demonstrate the value of both software solutions in understanding the complexities of surface infrastructure. This study highlights the need for further research to explore additional functionalities of both tools, including possible approaches to optimization and the integration of modern technologies in future analyses.

REFERENCES

ALMEHAIDEB R., AL-KHANBASHI A., ABDULKARIM M. & ALI M., (2000). "EOS tuning to model full field crude oil properties using multiple well fluid PVT analysis", https://doi.org/10.1016/S0920-4105(00)00043-7;

AL-SAFRAN EISSA and BRILL P. JAMES, (2017). "Applied Multiphase Flow in Pipes and Flow Assurance – Oil and Gas Production", Society of Petroleum Engineers, ISBN 978-1-61399-492-4;

BEGGS, D. and BRILL, J., (1973). "A study of two-phase flow in inclined pipes", Journal of Petroleum Technology, Vol. 25;

BRILL, J.P. and MUKHERJEE, H. (1999). "Multiphase Flow in Wells". Monograph series, SPE, Richardson, Texas 17: 2-69;

CHAVES G.S., KARAMI H., VIRGILIO JOSE MARTINS FERREIRA FILHO & BRUNO FERREIRA VIEIRA, (2022). "A comparative study on the performance of multiphase flow models against offshore field production data", Journal of Petroleum Science and Engineering, Volume 208, Part E, 109762, ISSN 0920-4105, https://doi.org/10.1016/j.petrol.2021.109762,
https://www.sciencedirect.com/science/article/pii/S092041052101384X ;

ELKAMEL, A., PARASCHIVOIU, M., & ALATIQI, I. (2003). "Process Optimization of Oil and Gas Separation." Journal of Petroleum Science and Engineering, 40(3), 109-123

EZEKWE NNAEMEKA, (2010). "Petroleum Reservoir Engineering Practice" , Prentice Hall, ISBN 0-13-715283-3;

FETOUI ISLAM, (2017). „Multiohase flow correlations", Production Technology;

FOSSMARK MARTHE GILJE, (2011). „Multiphase-Flow Correlations" University of Stavanger, Faculty of Science and Technology;

GUO BOYUN, LYONS C. WILLIAM & GHALAMBOR ALI, (2007). „Petroleum Production Engineering A Computer-Assisted Approach“, ISBN: 0750682701, Publisher: Elsevier Science & Technology Books;

GRUBAČ BRANKO, (2019). „Uticaj utiskivanja gas-lift gasa na prenos mase i toplote“, doktorska disertacija, Univerzitet u Beogradu Rudarsko-geološki fakultet;

HONEYWELL, (2009). „UniSim Design Black Oil Tutorial“, Prepared in Canada, dostupno na: Honeywell Black Oil;

KAZEMI KOROSH, (2011). „Prediction of Crude Oils PVT Properties Using Artificial Neutral Networks“, Master of Science Thesis, Petroleum University of Technology, Iran;

MADDONA S., NURPERBANGSARI DZ., SUGIANA A.M. & ZULKIFLIANI, (2022). „Bioprocess of Oil Contamined Water At Gathering Station Through A Consortium Of Endogenous and Exogenous Bacteria“, IOP Conf. Series: Earth and Environmental Science, doi:10.1088/1755-1315/1065/1/012063;

MARTINOVIC, B., ZIVKOVIC, M. & GRUBAC, B. (2022) ″Convective heat transfer in centrifugal pumps lifted wells: the case of South-Eastern Europe waxy wells″, Int. J. Oil, Gas and Coal Technology, Vol. 30, No. 3, pp.229–249.;

MITTBOCK SEBASTIAN, (2014). „Development of a Slug Analysis Tool for Slugging in Gas-Oil-Water Multiphase Pipelines and Comparison with Aspen Hysys“, masterthesis Vienna University of Technology;

PETROLEUM EXPERTS, (2011). „User Manual“ IPM PVTP Version 8.5 February;

PETROLEUM EXPERTS, IPM13. „Integrated Production Modelling User Manuals“;

PETROLEUM EXPERTS LTD. (2010). “Integrated Production Modeling Using GAP”, Petroleum Expert Technical Papers;

SARICA CEM & ZHANG HOLDEN, (2006). “Development of Next Generation Multiphase Pipe Flow Prediction Tools” The University of Tulsa, Tulsa University Fluid Flow Projects, DE-FC26-03NT15403;

XIAO, J.J., SHOHAM O. & BRILL J.P., (1990). „A Comprehensive Mechanistic Model for Two-Phase Flow in Pipelines“, University of Tulsa, Society of Petroleum Engineers, SPE 20631;

ZHANG H., WANG Q.,SARICA C. & BRILL J. (2003). “Unified model for gas - liquid pipe flow via slug dynamics-part 1: model development”, Journal of Energy Resources Technology, Vol. 125;

ZHAO YUANXI, (2016). „Property Package“; PVT-Flow-Assurance;

UNDERGROUND MINING ENGINEERING 46 (2025) 67-91 UDK 62
UNIVERSITY OF BELGRADE - FACULTY OF MINING AND GEOLOGY ISSN 03542904

Original scientific paper

PROSPER AND PIPESIM SOFTWARE FOR MODELING OF WELLS EQUIPPED WITH ESP SYSTEMS

Aleksandar Sredojević[1], Bojan Martinović[1], Milan Repac[1], Dino Jovanović-Sovtić[1], Ana Ponoćko[1], Miroslav Crnogorac[2], Dušan Danilović[2]

Received: November 29, 2024 **Accepted:** December 25, 2024

Abstract: When the pressure at the bottom of the well is insufficient to overcome the total pressure losses from the bottom of the well to the separator, production using reservoir energy is no longer possible, and the well ceases to naturally flow. To enable fluid production from the well again, it is necessary to apply some artificial lift systems. The most applicable artificial lift methods are gas lift (GL), sucker rod pumps (SRP), electric submersible pumps (ESP), progressive cavity pumps (PCP), and hydraulic pumps (HP).

This paper will delve into the modeling of wells equipped with electric submersible pump (ESP) systems, which are a widely adopted artificial lift methods in the oil and gas industry. This research aims to create accurate models that reflect the performance of these systems. For the modeling we will use industry standard software Prosper and Pipesim and perform a comparative study between both. Study will aim to show advantages and disadvantages of using both software, contributing to the understanding of their applicability in optimizing ESP system performance. Ultimately, this work seeks to enhance the knowledge base regarding effective exploitation methods in hydrocarbon extraction.

We begin by explaining the cessation of the well's natural flow, followed by a transition to an artificial lift method. The second section focuses on the methodology, explaining how each software Pipesim and Prosper employs specific empirical formulas and correlations for modeling, and how they use NODAL analysis to predict the well's behavior. The final part of the paper presents an actual case study in which the output data from both software programs are compared with the actual field-collected data from the ESP-equipped Well-X-1. Additionally, this analysis offers valuable insights into the strengths and limitations of using both Prosper and Pipesim, contributing to a deeper understanding of their applicability in optimizing ESP system performance. Ultimately, this study aims to enhance the knowledge base on effective exploitation methods in hydrocarbon extraction.

Keywords: Electric Submersible Pump (ESP), Fluid Production, Mechanical Exploitation Methods, Prosper, Pipesim

[1] STC NIS Naftagas doo, Narodnog fronta 12, 21000 Novi Sad
[2] University of Belgrade – Faculty of Mining and Geology, Djusina 7, Belgrade, Serbia

E-mails: aleksandar.sredojevic@nis.rs; bojan.martinovic@nis.rs; dino.jovanovic@nis.rs; milan.d.repac@nis.rs; ana.ponocko@nis.rs; miroslav.crnogorac@rgf.bg.ac.rs, ORCID 0000-0002-8078-2684; dusan.danilovic@rgf.bg.ac.rs, ORCID 0000-0002-2969-040X

1 INTRODUCTION

In oil production, the initial phase often sees wells producing oil through a process known as natural lift. This phase relies on the inherent energy of the reservoir, which,when substantial enough, enables fluids to ascend to the surface at economically viableflow rates (Martinović B. et al. 2023). When this condition is no longer met, natural flow ceases, and the well stops producing fluid. There are two main reasons for the cessation of reservoir fluid production:

- The dynamic pressure at the bottom of the well drops below the total pressure losses in the well.
- The pressure losses in the well become greater than the dynamic pressure required for oil flow to the surface (Gabor, T., 2018).

The first reason occurs due to a reduction in reservoir pressure caused by fluid depletion, while the second reason involves increased flow resistance in the tubing (production pipe). This can be caused by an increase in fluid density due to reduced gas production or various mechanical issues, such as smaller tubing dimensions and other limitations in the well equipment (Gabor, T., 2018).

When the pressure drops below the level that allows for eruptive operation or when production falls below the desired level, it is essential to apply one of the mechanical methods (gas lift, sucker rod pump, electric submersible pump, hydraulic pump, or progressive cavity pump) as soon as possible to ensure an extension of the production lifespan and increased ultimate recovery. The choice of method depends on the characteristics of the reservoir, the well, and the fluid being produced (Zhu, J. & Zhang H.Q., 2018).

In modern petroleum engineering, efficient well management and optimization of oil and gas production are key aspects of achieving commercial success. Electric submersible pumps (ESP) are one of the most important components in this process, playing a crucial role in lifting fluids from wells and ensuring production continuity. Modeling the well with an ESP system is a complex task that requires a detailed analysis of numerous factors, including the specific characteristics of the well, the mechanical properties of the fluid, and economic feasibility (Petroleum Experts 2022; Schlumberger, 2022).

This paper will discuss the method of modeling a well equipped with an ESP system, utilizing Prosper and Pipesim software for detailed modeling. The modeling process will involve inputting critical parameters such as fluid properties, reservoir characteristics, and operational conditions to create accurate representations of the well's performance with the ESP system.

The results obtained from these models will be compared with actual data collected from Well X-1 to assess their accuracy and effectiveness in predicting production behavior. This comparison will highlight any discrepancies and offer insights into the reliability of the modeling tools used. By analyzing the modeled outputs alongside real-world input data, this study will contribute to a deeper understanding of the dynamics at play in Well X-1, specifically in relation to the ESP system, and will evaluate the strengths and limitations of the Prosper and Pipesim software in practical applications. Ultimately, this research seeks to enhance methodologies for well modeling, particularly for wells equipped with ESP systems.

2 METHODOLOGY

The methodological framework of this paper consists of four distinct steps, each crafted to offer a systematic approach to the scientific objectives. The next section details the methodology of this study, encompassing data collection, model creation, model validation, and result finalization. Each of these steps is essential for a comprehensive understanding and interpretation of the results. The schematic diagram presented below (Figure 1) illustrates the interconnectedness of these methodological components

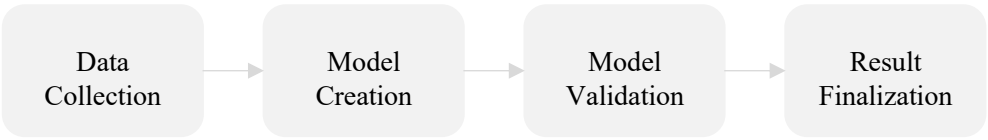

Figure 1 Schematic representation of methodology

2.1 Data collection

The data for this paper were collected from an operational oil well equipped with an ESP system. This comprehensive dataset includes a wide range of critical parameters that are vital for the analysis and modeling. Specifically, it encompasses production data (Table 1), which provides insights into the well's output over time; PVT properties of the fluid (Table 2), detailing the physical and thermodynamic characteristics of the produced fluid; information about the well equipment (Table 3), which outlines the technical specifications and components used; data related to the pump (Table 4), which includes specifications and performance metrics; well inclinometrics (Table 5), which present measurements of the well's inclination; and surface equipment data (Table 6), Together, these tables serve as a foundation for a thorough examination of the well's performance and the effectiveness of the ESP system.

Table 1 Production data

Serial number	Parameter	Unit of measure	Value
1	P_r	bar	181.7
2	T_r	◦C	128.9
3	WC	%	62
4	Q_{ftest}	m^3/day	50.5
5	P_{wf}	bar	153.88
6	P_{wh}	bar	24
8	P_{casing}	bar	1.1

Table 2 PVT data

Serial number	Parameter	Unit of measure	Value
1	Solution GOR	sm^3/m^3	60.6
2	Total GOR	sm^3/m^3	33
3	ρ_o	kg/m^3	857.5
4	ρ_{gr}	ρ_{gr}	0.814
5	Water salinity	ppm	16935
6	Molar percentage H_2S	mol %	0
7	Molar percentage CO_2	mol %	2.22
8	Molar percentage N_2	mol %	5.51

Table 3 Information about the well equipment

Serial number	Parameter	Unit of measure	Value
1	H_{tubing}	m	2100
2	ID_{tubing}	mm	62
3	$H_{perforations}$	m	2304-2313

4	OD_{tubing}	mm	73
5	H_{casing}	m	2309
6	ID_{casing}	mm	162
7	ID_{choke}	mm	4.6

Table 4 Data related to the pump

Serial number	Parameter	Unit of measure	Value
1	H_{ugr}	m	2100
2	F	Hz	39
3	L_{cable}	m	2100
4	$V_{surface}$	V	1000
5	Pump stages	/	360

Table 5 Well inclinometrics

Serial number	MD (m)	TVD (m)
1	0	0
2	10	10
3	140	139.998
4	270	269.992
5	400	399.988
6	530	529.988
7	660	659.985
8	790	789.983
9	920	919.979
10	1050	1049.97
11	1180	1178.31
12	1310	1305.48
13	1440	1431.86
14	1570	1558.81
15	1700	1685.71

16	1830	1812.84
17	1960	1939.15
18	2090	2065.8
19	2220	2193.03
20	2386	2354.1

Table 6 Surface equipment data

Serial number	Parameter	Unit of measure	Value
1	Pipeline length	m	300
2	Internal diameter of the pipeline	mm	73
3	Pipe wall thickness	mm	5.3
4	Coefficient of thermal conductivity of pipelines	W/mK	X
5	Absolute roughness of the inner wall of the pipeline	mm	X
6	Average digging depth	m	0.8-1
7	Soil temperature at the depth of burial	◦C	X
8	Thermal conductivity coefficient of the soil	W/mK	X
9	Thermal conductivity coefficient of polyurethane foam insulation	W/mK	X
10	Separator pressure	bar	2
	Separator temperature	◦C	X

2.2 Model Creation

NODAL analysis, as applied in this study to assess well performance, is a key technique in reservoir and production engineering. It provides a structured framework for evaluating and optimizing the operation of oil and gas wells—including those using Electric Submersible Pumps (ESP)—from the reservoir all the way to the wellhead. By incorporating factors such as wellbore geometry, tubing and casing dimensions, and

completion design, this method offers a realistic representation of well behavior under actual operating conditions (Mach et al., 1979; Ješić M. et al. 2023).

All modeling performed in Prosper and Pipesim is based on the principles of nodal analysis, which will be the core methodology used in this study to better understand and forecast well behavior. This approach enables a comprehensive exploration of the factors influencing well performance. (Petroleum Experts 2022; Schlumberger, 2022).

In the oil and gas sector, Inflow Performance Relationship (IPR-curve) and Vertical Lift Performance (VLP-curve) are two fundamental tools used to evaluate and optimize well performance. IPR describes how the production rate of a well relates to its bottomhole pressure, providing valuable insights for managing reservoir behavior and improving production efficiency. On the other hand, VLP examines how the production rate correlates with tubing head pressure, helping engineers assess the performance of artificial lift systems and surface facilities (Golan & Whitson, 1991). Both IPR and VLP are utilized in modeling wells using Prosper and Pipesim, allowing for a comprehensive evaluation of well performance and optimization strategies.

The Inflow Performance Relationship (IPR) describes the link between the wellbore flowing pressure and the surface liquid production rate. This concept has been a cornerstone of well performance analysis since bottom hole pressure gauges were first introduced in the 1920s (Golan & Whitson, 1991). Among the different models within the IPR framework, the Productivity Index (PI) is one of the most straightforward. It expresses how efficiently a well produces by relating the surface liquid flow rate to the pressure drawdown across the reservoir, typically measured at the midpoint of the producing zone, as shown in Equation 1 (Gabor, T., 2018)

$$J = \frac{Q}{(p_r - p_{wf})} \quad 1$$

Where:

Q - flow rate, m³/day

J - productivity index, m³/day/bar

p_r - reservoir pressure, bar

p_{wf}- flowing bottomhole pressure, bar

In many wells using mechanical production methods, bottomhole pressures are below saturation pressure, resulting in a certain amount of gas being released from the oil. Due to the presence of a free gas phase in the reservoir, the assumptions used to develop the PI equation are no longer valid. There are methods employed when reservoir pressure is

lower than saturation pressure, one of which is Vogel's method (1968) (Golan & Whitson, 1991).

$$\frac{Q}{Q_{max}} = 1 - 0.2\frac{p_{wf}}{p_r} - 0.8(\frac{p_{wf}}{p_r})^2 \quad (2)$$

Q - production at pressure p_{wf}, m³/day

Qmax - maximum production, m³/day

p_r - average reservoir pressure, bar

p_{wf} - flowing bottomhole pressure, bar

Vertical Lift Performance (VLP) correlations are empirical relationships and mathematical expressions used to predict and analyze the performance of artificial lift systems in oil and gas wells. These correlations are crucial for engineers and industry professionals, enabling them to estimate production rates, optimize lift systems, and make informed decisions regarding well operations (Soleša, M., Danilović, D & Buza, Z. 1999).

Some of the empirical correlations are illustrated in Figure 2 and can be classified into the following categories:

- Category "a": No slip, no flow pattern consideration required is for the two-phase friction factor
- Category "b": Slip and no flow pattern was considered. A correlation is required for both liquid holdup and friction factor
- Category "c": After using a method to establish the flow pattern, the appropriate holdup and friction-factor correlations are determined (Hofstatter, H., 2018).

Method	Category
Poettmann and Carpenter	a
Baxendell and Thomas	a
Fancher and Brown	a
Hagedorn and Brown	b
Gray	b
Asheim	b
Duns and Ros	c
Orkiszewski	c
Aziz et al.	c
Chierici et al.	c
Beggs and Brill	c
Mukherjee and Brill	c

Figure 2 Empirical correlations (Hofstatter, H., 2018)

The creation of a well model during NODAL analyses for Pipesim and Prosper software consists of the following steps (Ješić M. et al. 2023):

1. Outline key aspects of the well completion: Begin by inputting essential completion data such as tubing and casing sizes, the type of completion, and any artificial lift methods being used;
2. Specify PVT Properties: Define the pressure-volume-temperature (PVT) properties of the well fluids, including composition, density, viscosity, and other key characteristics that influence flow behavior;
3. Define the Inflow Performance Relationship (IPR-curve): Establish the relationship between bottomhole pressure and production rate to evaluate the well's productivity under different reservoir conditions;
4. Input Hydrodynamic Measurements: Incorporate the most recent dynamic pressure data to accurately represent the current performance of the well;
5. Vertical Lift Performance (VLP-curve): Develop VLP models to assess the well's response to changes in tubing and casing pressures;
6. Run NODAL Analysis: Carry out the NODAL analysis to model how the well behaves under different operating scenarios. This involves calculating key parameters such as pressure, flow rate, and temperature at various points along the production system to better understand and predict overall well performance;

7. Review Simulation Results: Analyze the output, focusing on parameters such as wellhead pressure, tubing and casing pressures, flow rates, and temperature profiles. Assess performance across a range of scenarios;

8. Optimize Well Performance: Based on the analysis, make adjustments as needed—such as modifying choke size, changing completion configuration, or tuning artificial lift parameters—to enhance production efficiency (Ješić M. et al. 2023).

2.3 Model Validation

To successfully validate the model, whether using Prosper or Pipesim, it is essential that the actual production data closely align with the data generated by the constructed model. It is important to recognize that some discrepancies may arise between the modeled data and the actual measurements, regardless of the software used.

If, for any reason, the model fails to align with the actual well data, it may be necessary to adjust specific parameters that are either unavailable or considered unreliable. Such adjustments are crucial for enhancing the model's accuracy and predictive capabilities.

For example, it may be necessary to modify the discharge coefficient for the nozzle, as it can significantly impact flow characteristics. Additionally, if the well uses artificial lift methods, adjustments to parameters such as the pump wear factor and the volumetric pump factor may also be required. These parameters are critical for accurately reflecting the well's performance and ensuring that the model provides a reliable representation of the actual operating conditions.

Additionally, various correlations can be employed, as they can significantly influence the final results of the model. Prosper utilizes proprietary correlations, such as the "Petroleum Experts 3" correlation, which are specifically tailored to enhance modeling accuracy within its framework. In contrast, Pipesim uses established and experimentally validated correlations that have been rigorously tested in real-world scenarios. These correlations play a crucial role in determining fluid behavior, pressure drops, and overall production performance. The choice between proprietary and established correlations can affect not only the reliability of the model but also its applicability to different well conditions. Therefore, understanding the implications of these correlations is essential for optimizing the modeling process and ensuring that the results accurately reflect the well's performance. (Petroleum Experts, 2022; Schlumberger, 2022).

By making these necessary corrections, we can improve the model's alignment with the real-world data, thereby increasing its validity and usefulness in predicting future well behavior.

3 RESULTS AND DISCUSSION

This analysis focuses on well X-1, which is equipped with an Electric Submersible Pump (ESP) system. The modeling was conducted using Prosper and Pipesim software.

3.1 Modeling in Prosper

The Prosper software enables detailed well modeling, beginning with the input of PVT fluid properties (Figure 3). To create the IPR (Inflow Performance Relationship) curve, Vogel's method is utilized (Figure 4). This method is efficient as it requires only a single measurement to produce reliable results

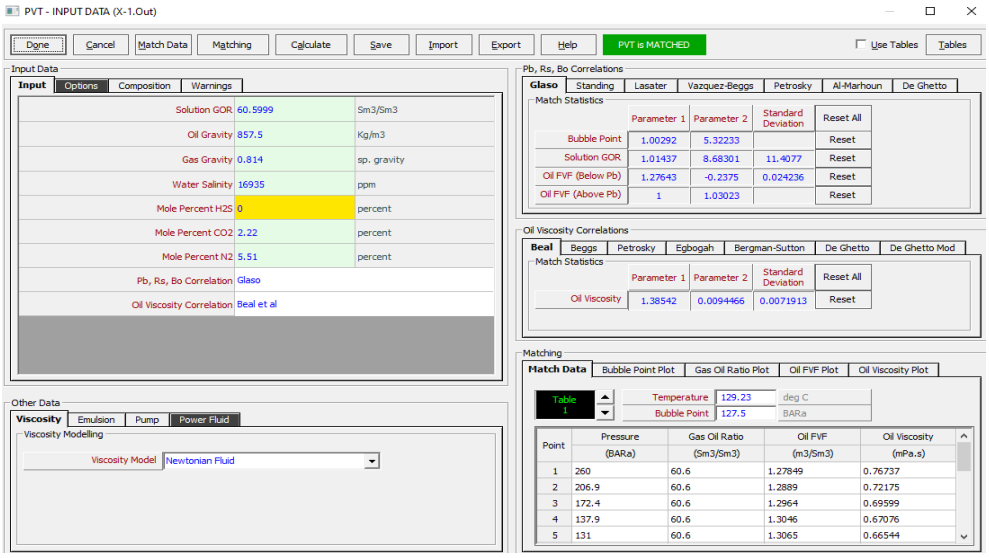

Figure 3 Input of PVT fluid properties

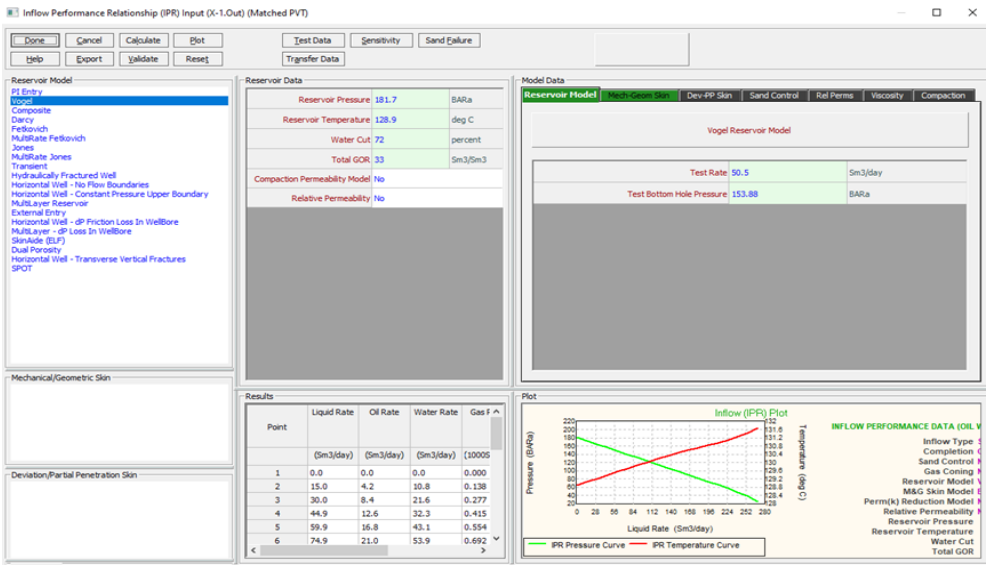

Figure 4 Input data for IPR

The selection of an ESP system (Figure 5) involves several key factors: the target production rate should be a percentage of the well's Absolute Open Flow Potential (AOFP), the chosen ESP must offer the highest pump efficiency at the desired production rate, and the pump diameter must be smaller than the internal diameter of the casing. In this study, the scenarios analyzed include using an ESP with an anchor gas efficiency of 90% (Gas in Place, GIP = 10%), with the pump positioned at the bottom of the well (Bagci A. et al. 2010). Based on these criteria, the 5-50 pump was selected.

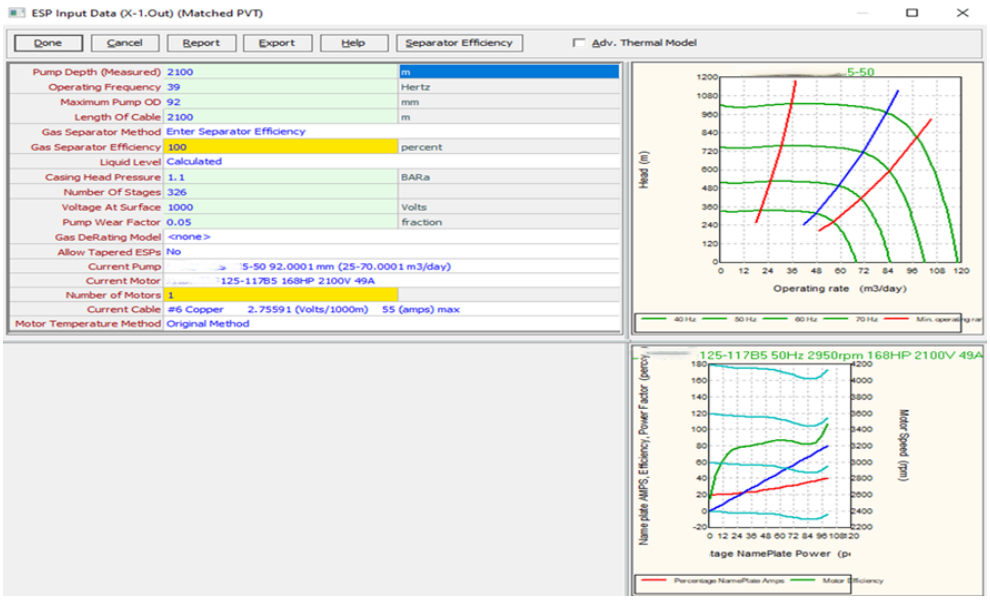

Figure 5 Input data for the Pump

The modeling process involves incorporating inclination data (Figure 6) and specifying the downhole equipment (Figure 7). Additionally, surface choke parameters (Figure 8) are included if necessary to accurately simulate the flow conditions.

DEVIATION SURVEY (X-1.Out)

Done | Cancel | Main | Help | Filter | Plot

MD <-> TVD

662 | 661.985 | Calculate

Input Data

Point	Measured Depth (m)	True Vertical Depth (m)	Cumulative Displacement (m)	Angle (degrees)
1	0	0	0	0
2	10	10	0.00349	0.019996
3	140	139.998	0.75223	0.33
4	270	269.992	1.93206	0.52
5	400	399.988	2.95307	0.45
6	530	529.988	3.36147	0.18
7	660	659.985	4.17828	0.36
8	790	789.983	4.94971	0.34
9	920	919.979	5.94803	0.44
10	1050	1049.97	7.35472	0.61999
11	1180	1178.31	28.0721	9.17
12	1310	1305.48	55.034	11.97
13	1440	1431.86	85.5143	13.56
14	1570	1558.81	113.518	12.44
15	1700	1685.71	141.744	12.54
16	1830	1812.84	168.884	12.05
17	1960	1939.15	199.629	13.68
18	2090	2065.8	228.983	13.05
19	2220	2193.03	255.656	11.84
20	2386	2354.1	295.815	14

Figure 6 Input data for deviation survey

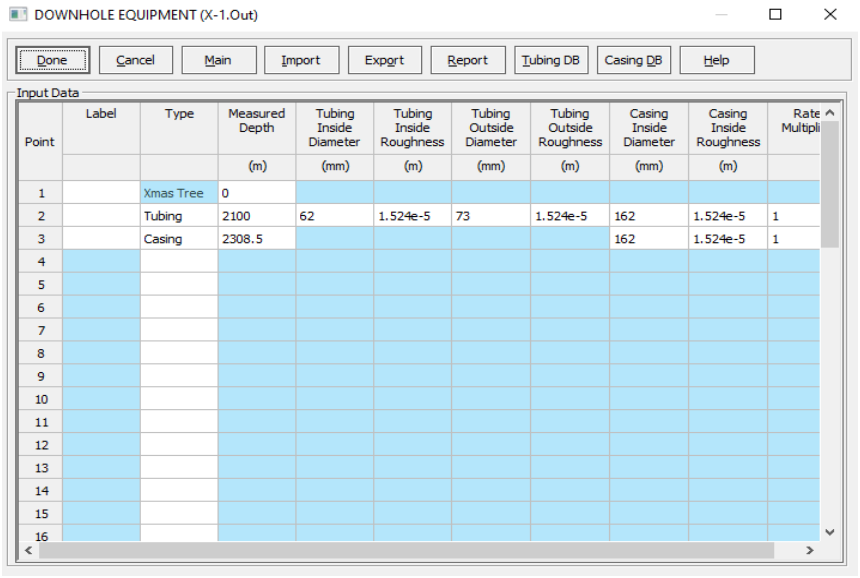

Figure 7 Input data for downhole equipment

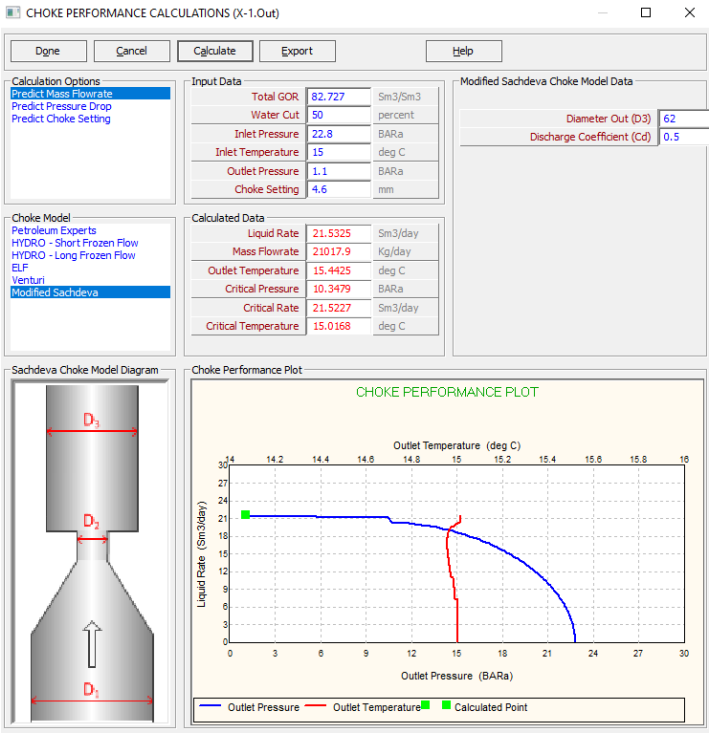

Figure 8 Input data for surface choke parameters

At the end of the modeling process, users can access the sensitivity analysis window (Figure 9) to select specific correlations that align with actual data on fluid flow rates and bottom hole pressure. When the simulated results closely match the actual measurements, it confirms that the well has been accurately modeled.

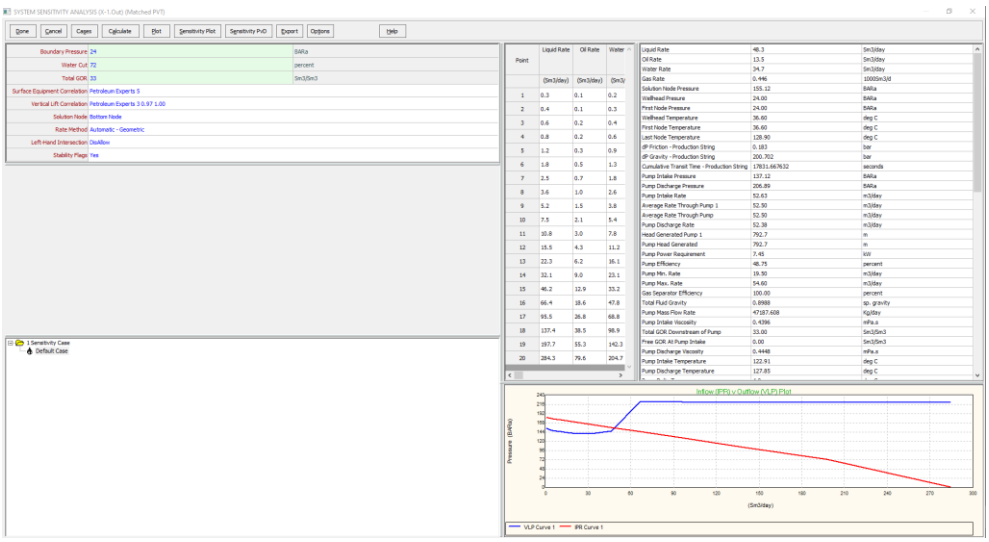

Figure 9 Sensitivity analysis window

In this window, users can also conduct a sensitivity analysis, which allows for the modification of specific parameters such as frequency, tubing diameter, and choke diameter. This analysis enables the evaluation of how changes in these parameters impact other variables, such as fluid production. By examining these relationships, engineers can identify optimal conditions and make informed decisions to enhance overall well performance. Additionally, this approach helps predict the well's behavior in response to these changes, providing valuable insights for future operational strategies.

3.2 Modeling in Pipesim

The initial step in the process of modeling any well in Pipesim involves entering crucial parameters that pertain to both the well dimensions and the associated production equipment (Figure 10). This specifically includes detailed information about the sizes and specifications of the tubing and casing. Accurately inputting these parameters is essential, as they lay the groundwork for all subsequent analyses and simulations within the modeling framework.

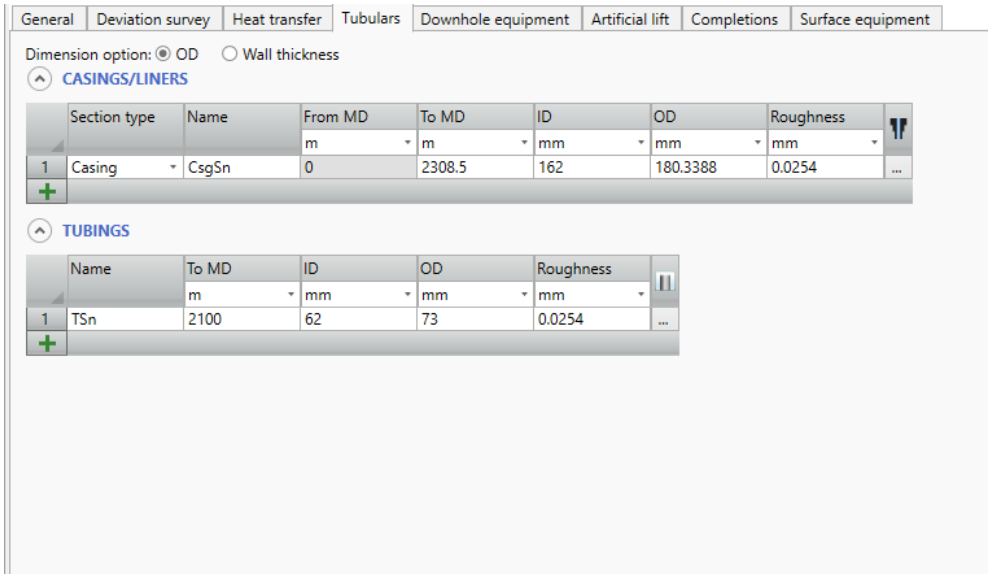

Figure 10 Input of data for well dimensions and production equipment

The next step involves entering the PVT properties of the fluid (Figure 11) and the data needed to construct the IPR curve (Figure 12). The "Black oil model" was used for constructing the reservoir fluid, which is the same model utilized in Prosper, and Vogel's method was also employed for the IPR curve. The primary and most important parameter in the Black oil model is the oil viscosity; without this parameter, it is not possible to construct the Black oil model.

Crude oil viscosity affects the flow of oil through porous media and pipes. It is defined as the internal resistance of the fluid to flow (Wang et al., 1964). Literature survey shows that change of viscosity with temperature and pressure is commonly predicted empirically when it is not possible to perform analysis in laboratory (Martinović B., Zivkovic, M. and Grubac, B. 2022).

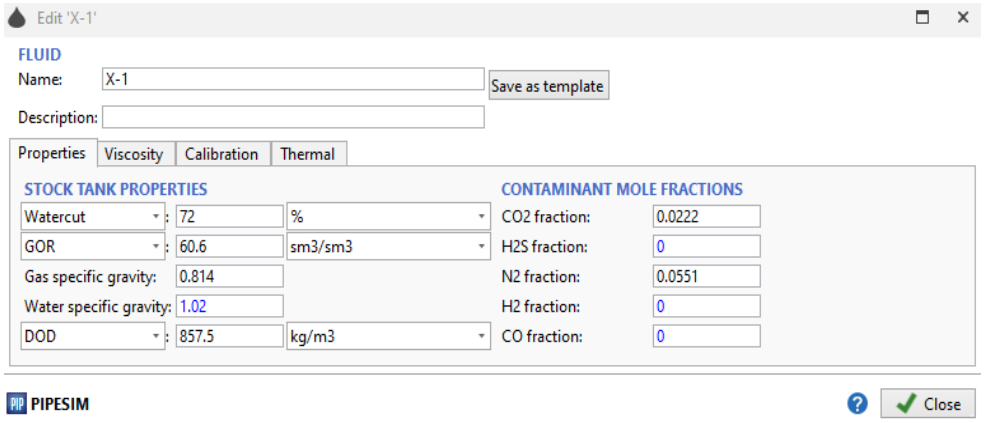

Figure 11 Input of PVT fluid properties

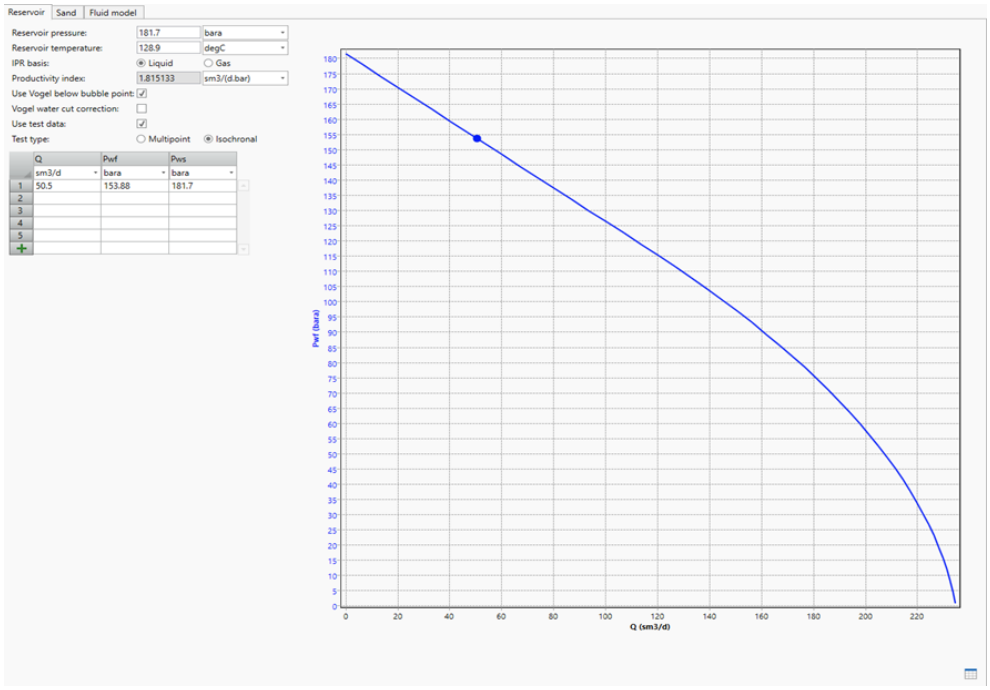

Figure 12 Input data for IPR

After that, data for the well's inclinometry is entered (Figure 13), along with information related to the pump. Using the software, the appropriate pump is selected—in this case, the Borets ESPM5-50. This process is illustrated in Figure 14, where the performance curve of the pump is shown on the left. Additionally, a suitable electric motor is selected.

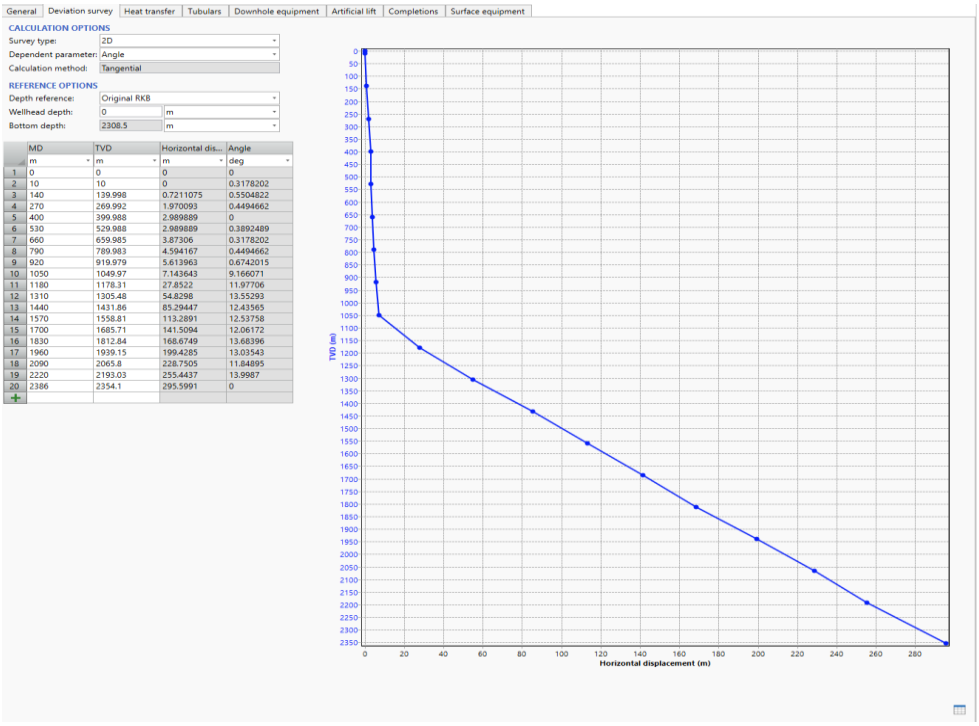

Figure 13 Input data for deviation survey

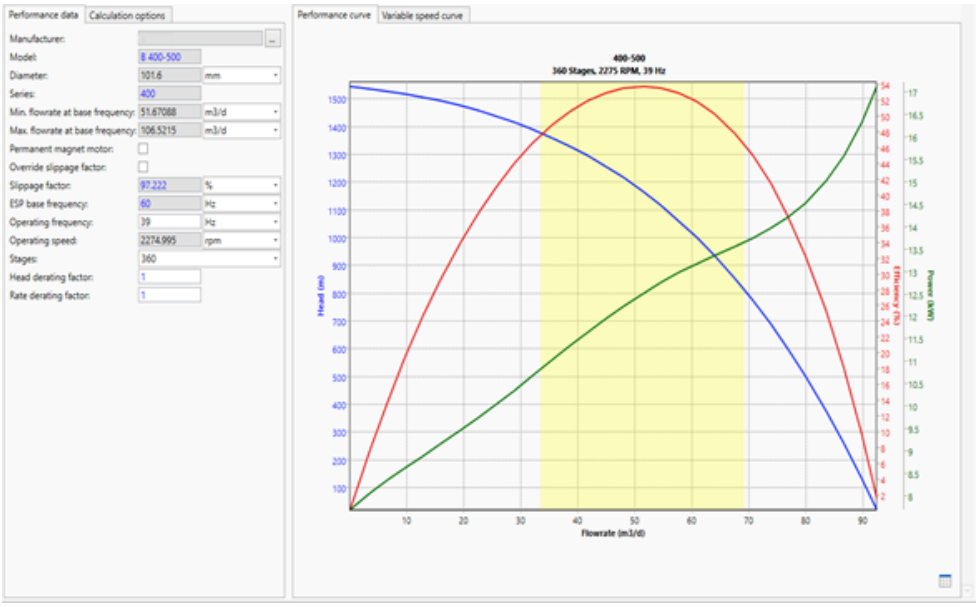

Figure 14 Input data for the Pump

The next step involves entering the surface nozzle data, as shown in Figure 15. After that, you proceed to the "Data comparison" window, where specific correlations are selected. The software then identifies the most suitable correlation that aligns with the entered data. This window is illustrated in Figure 16.

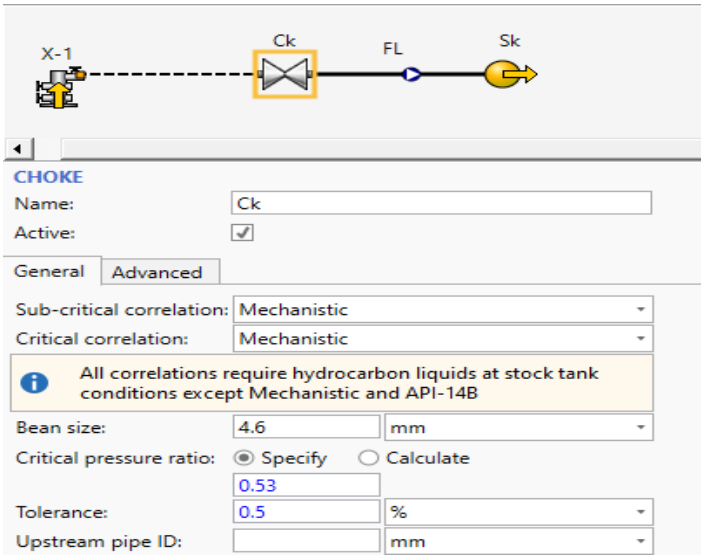

Figure 15 Input data for surface choke parameters

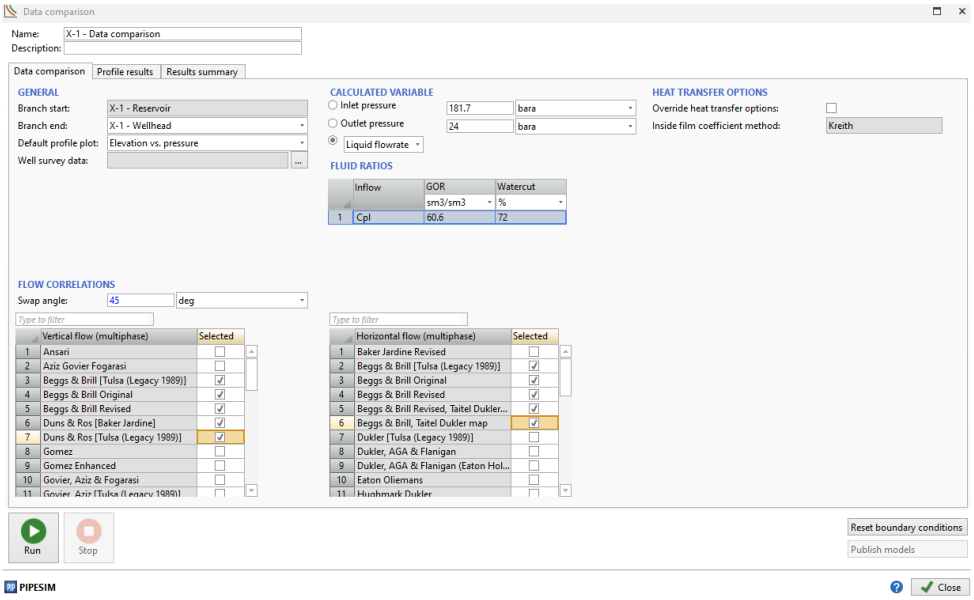

Figure 16 Selection of correlation

Finally, the "Nodal analysis" window (Figure 17) is opened, where the results are obtained, including the production rate of the reservoir fluid and the bottom-hole pressure. In Figure 17, the intersection of the IPR and TPR (VLP) curves is shown. The Tubing Performance Relationship (TPR) represents the ability of the tubing to transport fluid. The optimal tubing size can be selected by determining the best flow rate for each well using a sensitivity analysis that compares the TPR curves for various tubing sizes with the IPR curve. (Guo et al. 2015)

These results are then compared with actual data, and we can conclude that the model has been validated, as the results obtained from the nodal analysis closely match the actual data from the well.

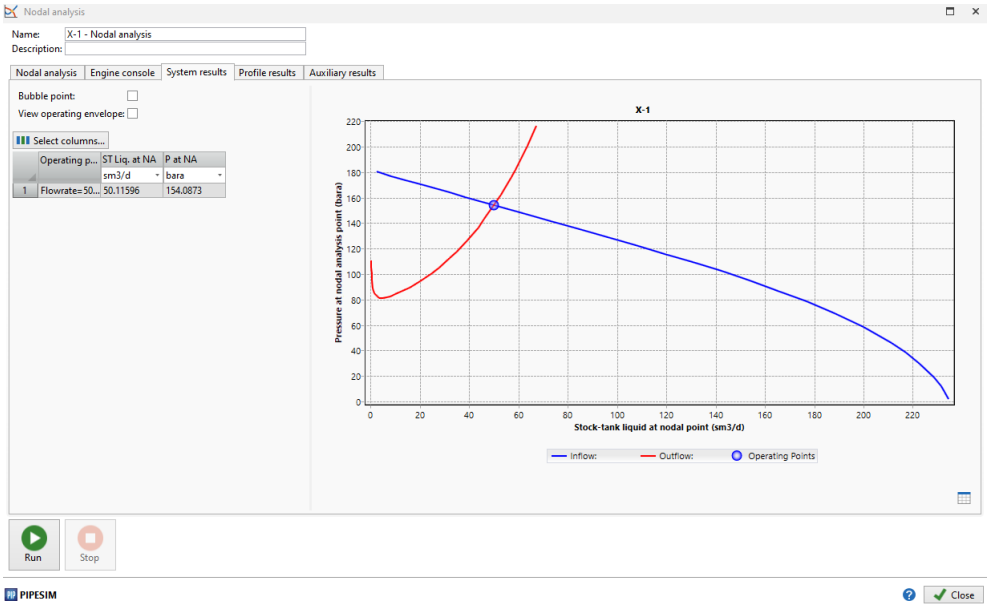

Figure 17 Display of the window with output data

3.3 Analysis of the results

The results for the models in Prosper and Pipesim are presented in Table 7. This table compares key metrics such as production rates, bottom-hole pressures, and pressure at the wellhead from both modeling approaches. Analyzing these results side by side allows for a comprehensive evaluation of the performance and reliability of each model, providing valuable insights into their effectiveness in simulating the well's behavior under various conditions.

Table 7 Results obtained from both software programs

Serial number	Parameter	Unit of measure	Prosper	Pipesim	Fakt
1	Q_f	m^3/day	49.8	50.1	50.5
2	P_{wf}	bar	154.3	154.1	153.9
3	P_{wh}	bar	24	23	24

Table 8 presents the deviations from actual values for both Prosper and Pipesim software. As we can see, the deviations in the Prosper model are smaller compared to those in the Pipesim model. Nonetheless, the deviations are relatively minor, indicating that both software programs have demonstrated their capability to effectively model a well equipped with an ESP system. This suggests that users can rely on either tool for accurate simulations in such applications.

Table 8 Deviation of results from actual values

Serial number	Unit of measure	Parameter	Prosper		Pipesim	
			Δ	**Δ(%)**	**Δ**	**Δ(%)**
1	m^3/day	Q_f	0.7	0.7	0.4	0.4
2	bar	P_{wf}	-0.4	-0.1	-0.22	-0.1
3	bar	P_{wh}	0	0	1	2.1

The primary difference between these two software programs lies in their approach to correlations. Prosper utilizes its proprietary correlations, such as "Petroleum Experts 3," while Pipesim employs existing, experimentally validated correlations. Prosper is distinguished by its simplicity and user-friendliness compared to Pipesim, as evidenced by its clearer and more accessible manual, which facilitates user familiarity with the software. In contrast, Pipesim provides a broader range of correlations and a more extensive catalog of ESP pumps (Petroleum Experts 2022; Schlumberger, 2022).

The Pipesim simulator includes models for a variety of common surface facility equipment to determine their impact on system design. The sophisticated sensitivity options in the Pipesim simulator can be used to design systems by varying key operating parameters, thus enabling determination of the optimal pipeline and equipment sizes. This entails the following:

- Control of pump performance by applying limits for ΔP, power, and other individual factors or a combination of these
- Calculation of pump parameters (such as ΔP and power) for single or multiple sets of operating conditions
- Simple thermodynamic model or user-specified curves
- Availability of most pump performance parameters (including head, ΔP, power, number of stages, speed, and efficiency) as sensitivity variables for design or uncertainty analysis
- Viscosity correction (Turzo method) (Schlumberger, 2022)

Prosper categorizes pumps and motors by diameter and performance characteristics, leaving it up to the user to ensure that the selected motor is physically compatible with the pump and to choose the most economical combination of voltage and current. Meanwhile, Pipesim filters appropriate pumps from the catalog based on the data provided in the model (Petroleum Experts 2022; Schlumberger, 2022).

Both software applications can also be utilized to model wells employing various types of artificial lift methods, as well as those that operate on a natural flow basis. This versatility allows for a comprehensive analysis of different extraction techniques, enabling users to simulate various scenarios and optimize performance based on specific operational conditions.

4 CONCLUSION

Effectively modeling a well equipped with an ESP (Electric Submersible Pump) system in specific reservoirs to enhance or increase production is a complex task. Making informed decisions requires extensive data collection on well conditions, reservoir characteristics, fluid properties, and production metrics. Software tools like Prosper and Pipesim enable a swift and accurate modeling process for ESP systems.

Using Prosper and Pipesim in ESP-equipped well modeling within the oil industry significantly streamlines and accelerates the workflow. It can be concluded that modeling wells equipped with ESP systems allows for accurate predictions of well behavior through sensitivity analysis. This approach enables parameter adjustments, such as changing the ESP system's operating frequency or installing a new pump, to observe potential pump performance in the well, along with anticipated production rates and pressure levels.

These models serve as digital replicas of actual wells, where parameters can be adjusted, mistakes can be explored and corrected, and lessons learned ultimately preventing similar issues in real-world conditions.

While both software programs effectively model ESP-equipped wells, each offers unique advantages depending on project needs. Prosper is ideal for projects requiring simplicity and high accuracy, while Pipesim is more suited to complex analyses involving multiple variables and advanced correlations. Therefore, oil industry professionals should select the software that best matches their project requirements and objectives to optimize the performance and efficiency of ESP-equipped wells.

REFERENCES

BAGCI, A. S., KECE, M., NAVA, J. (2010). Challenges of Using Electrical Submersible Pump (ESP) in High Free Gas Applications, SPE-131760;

GABOR TAKACS, (2018). „Electrical Submersible Pumps Manual Design, Operations, and Maintenance Second edition“;

GUO, D., RAGHAVENDRA, C. S., YAO, K. T., HARDING, M., ANVAR, A., PATEL, A. (2015). Data Driven Approach to Failure Prediction for Electrical Submersible Pump System, SPE- 174062-MS.

HOFSTATTER, H., (2018). Oil and Gas Production Principls: 9th Lecture: Vertical Lift Performancee (VLP);

JEŠIĆ M., MARTINOVIĆ B., STANČIĆ S., CRNOGORAC M., DANILOVIĆ D., (2023) „Mitigating Hydrate Formation in Onshore Gas Wells: a Case Study on Optimization Techniques and Prevention“, University of Belgrade - Faculty of Mining and Geology

MACH, J., PROANO, E., and BROWN, K.E. (1979) A Nodal Approach for Applying Systems Analysis of the Flowing and Artificial Lift Oil or Gas Well. Paper SPE 8025 available from SPE, Richardson, Texas.

MARTINOVIC, B., ZIVKOVIC, M. and GRUBAC, B. (2022) ‘Convective heat transfer in centrifugal pumps lifted wells: the case of South-Eastern Europe waxy wells’, Int. J. Oil, Gas and Coal Technology, Vol. 30, No. 3, pp.229–249.

MARTINOVIĆ B., BIJANIĆ M., DANILOVIĆ D., PETROVIĆ A. & DELIBASIĆ B. (2023) „Unveiling Deep Learning Insights: A Specialized Analysis of Sucker Rod Pump Dynamographs, Emphasizing Visualizations and Human Insight“, Mathematics 2023, 11, 4782.;

MICHAEL GOLAN, CURTIS H. WHITSON, (1991). „Well Performance Second Edition“, Norwegian University of science and Technology (NTNU);

PETROLEUM EXPERTS, (2022). „Prosper Software User Manual“ Edinburgh, Scotland, UK: PE Limited;

SCHLUMBERGER, (2022). „Pipesim User Guide“ Houston, Texas, USA: SLB;

SOLEŠA, M., DANILOVIĆ, D., BUZA, Z. (1999). „Sistem analiza proizvodnje nafte i gasa eruptivnom metodom“; Univerzitet u Beogradu, Rudarsko-geološki fakultet;

WANG, Z., FINGAS, M., YANG, C. AND CHRISTENSEN, J.H. (1964) „Crude oil and refined product fingerprinting: principles“, Environmental Forensics, pp.339–407.

ZHU, J. & ZHANG H.Q. (2018). „A Review of Experiments and Modeling of Gas-Liquid Flow in Electrical Submersible Pumps“, project: Mechanistic modeling in Electrical Submersible Pumps (ESP)

PETROLEUM EXPERTS, (2022). „Prosper Software User Manual“ Edinburgh, Scotland, UK: PE Limited;

SCHLUMBERGER, (2022). „Pipesim User Guide“ Houston, Texas, USA: SLB;

SOLEŠA, M., DANILOVIĆ, D., BUZA, Z. (1999). „Sistem analiza proizvodnje nafte i gasa eruptivnom metodom“; Univerzitet u Beogradu, Rudarsko-geološki fakultet;

WANG, Z., FINGAS, M., YANG, C. AND CHRISTENSEN, J.H. (1964) „Crude oil and refined product fingerprinting: principles“, Environmental Forensics, pp.339–407.

ZHU, J. & ZHANG H.Q. (2018). „A Review of Experiments and Modeling of Gas-Liquid Flow in Electrical Submersible Pumps“, project: Mechanistic modeling in Electrical Submersible Pumps (ESP).

UNDERGROUND MINING ENGINEERING 46 (2025) 93-100 UDK 62
UNIVERSITY OF BELGRADE - FACULTY OF MINING AND GEOLOGY EISSN 2560-3337

Original scientific paper

CORROSION RESISTANCE of X12CrMoWVNbN10-1-1 STEEL in NaCl SOLUTIONS at DIFFERENT pH VALUES

Jovanka Pejić[1], Borut Kosec[2], Olga Pantić[1], Tatjana Volkov Husović[3], Matija Zorc[2], Milica Vlahović[1]

Received: January 11, 2025 **Accepted:** January 29, 2025

Abstract: The influence of pH on the corrosion behavior of X12CrMoWVNbN10-1-1 steel was examined in 0.1 M NaCl solution. The rate of general (uniform) corrosion of the tested steel was determined using linear polarization resistance (LPR) and electrochemical impedance spectroscopy (EIS) methods. In the NaCl solution with a pH of 2.9, the tested steel exhibited a more negative corrosion potential and lower corrosion resistance. Significantly higher corrosion potential and resistance to general corrosion were observed in a neutral solution (pH = 6.5), where the steel was in a passive state.

Keywords: Alloy steels, Corrosion, Passive layer, Electrochemical methods

1 INTRODUCTION

X12CrMoWVNbN10-1-1 steel is a high-alloy ferritic-martensitic steel used primarily in thermal power plants, especially in steam generators, due to its exceptional properties. This steel exhibits resistance to plastic deformation at high temperatures, good toughness, and resistance to radiation and corrosion in elevated temperature environments. These properties make X12CrMoWVNbN10-1-1 steel well-suited for applications in industries that demand high-temperature performance and exceptional mechanical characteristics (Bendick and Ring, 1996; Haarmann et al., 2002; Little, 1972; Garr, Rhodes and Kramer, 1973).

[1] University of Belgrade, Institute of Chemistry, Technology and Metallurgy- National Institute of the Republic of Serbia, Njegoševa 12, Belgrade, Serbia
[2] University of Ljubljana, Faculty of Natural Sciences and Engineering, Aškerčeva cesta 12, Ljubljana, Slovenia
[3] University of Belgrade, Faculty of Technology and Metallurgy, Karnegijeva 4, Belgrade, Serbia

E-mails: jovanka.kovacina@ihtm.bg.ac.rs, ORCID: 0000-0002-3494-9180; borut.kosec@ntf.uni-lj.si, ORCID: 0009-0001-8117-9721; olga.pantic@ihtm.bg.ac.rs, ORCID: 0000-0003-4667-2585; tatjana@tmf.bg.ac.rs, ORCID: 0000-0002-2667-5802; matija.zorc@ntf.uni-lj.si, ORCID: 0009-0002-8792-0549; m.vlahovic@ihtm.bg.ac.rs, ORCID: 0000-0002-7893-9101

Since X12CrMoWVNbN10-1-1 steel is used under extreme conditions, its high corrosion resistance is crucial. This includes resistance to corrosion in the presence of the vapor phase and various types of electrolytes, particularly those with an acidic nature. The most common form of corrosion in acidic electrolytes is general (or uniform) corrosion, which involves the uniform dissolution of the metal surface, leading to a gradual reduction in the steel's thickness.

A quantitative indicator of general (uniform) corrosion is the corrosion rate, which can be determined in different ways.

Electrochemical techniques allow for the determination of parameters such as polarization resistance (R_p) and corrosion current density (j_{corr}). The corrosion rate (v_{corr}) can be directly calculated from the corrosion current density using Faraday's law. Additionally, polarization resistance is related to corrosion current density through a corresponding equation.

In this study, the general (uniform) corrosion rate of X12CrMoWVNbN10-1-1 steel in acidic and neutral NaCl solutions was determined using two electrochemical methods-linear polarisation resistance (LPR) and electrochemical impedance spectroscopy (EIS). The values of polarization resistance (R_p) and corrosion current density (j_{corr}) were used as indicators of resistance to general corrosion.

2 EXPERIMENTAL

2.1 Material characterization

The standard chemical composition of the tested steel (Materials Number 1.4906, X12CrMoWVNbN10-1-1) (ASTM A335, 2022), as well as the values determined by the XRF method using an Olympus Vanta C Series Handheld XRF Analyzer, are presented in Table 1.

Table 1 Chemical composition of the X12CrMoWVNbN10-1-1 steel (wt. %)

	C	Si	Mn	Cr	Mo	Ni	V	W	Nb	N	S
Standard	0.10 - 0.14	≤ 0.12	0.40 - 0.60	10.0 - 11.0	1.00 - 1.20	0.60 - 0.80	0.15 - 0.25	0.95 - 1.10	0.04 - 0.06	0.04 - 0.07	≤ 0.007
XRF	-	0.92	0.49	10.16	1.05	0.77	0.17	0.92	0.055		0.11

The tested steel contains a high concentration of chromium (Table 1), which allows it to exhibit stainless steel-like behavior under approximately neutral conditions. Before the

electrochemical tests, the X12CrMoWVNbN10-1-1 steel samples were ground with abrasive paper up to 1500 grit, degreased with ethanol, rinsed with distilled water, and air-dried. The samples were then stored in a desiccator until the start of the tests

2.2 Electrochemical testing

Two 0.1 M NaCl solutions, prepared with bidistilled water, were used for electrochemical tests. The first solution had a pH of 2.9 (acidic solution), adjusted by carefully adding 0.1 M HCl, while the second solution had a pH of 6.5 (neutral solution). The pH value was measured using a HANNA Instruments HI 2210 device.

Linear Polarisation resistance (LPR) method

LPR measurements were performed at room temperature in both acidic and neutral chloride-containing solutions. The tests were conducted in a standard three-electrode electrochemical cell using a potentiostat/galvanostat/ZRA GAMRY 620. The working electrode was the steel specimen (with a working area of 1 cm^2), the reference electrode was a Saturated Calomel Electrode (SCE), and the auxiliary electrode was a Pt-mesh. After achieving a stable corrosion potential (E_{corr}), the specimens were polarized within a narrow potential range (E = ±10 mV) relative to E_{corr}, starting from the cathodic to the anodic region, and the corresponding current density (j) was recorded. The potential sweep rate was 0.166 mVs^{-1}. The polarization resistance (Rp) was determined as the slope of the recorded E-j curve at the E_{corr}.

Electrochemical Impedance spectroscopy (EIS) method

EIS measurements were carried out in both acidic and neutral chloride-containing solutions. After stabilizing the corrosion potential (E_{corr}), a sinusoidal potential of amplitude ±10 mV vs. E_{corr} across a frequency range from 100,000 Hz to 0.001 Hz was applied to the specimen (with a working area of 1 cm^2). The reference electrode was SCE, and the auxiliary electrode was Pt-mesh. Measurements were conducted using the potentiostat/galvanostat/ZRA GAMRY 620, and the EIS data were analyzed and fitted using the Gamry Echem Analyst software.

2.3 Optical microscopy

The surface morphology of the tested specimens, both before and after electrochemical testing, was analyzed using a Delta Optical Smart 5MP PRO digital USB microscope, accompanied by the Delta Optical Smart Analysis Pro software package.

3 RESULTS AND DISCUSSION

3.1 LPR measurements

Polarisation (potential-current density, E-j) diagrams obtained using the LPR technique in solutions with different pH values are shown in Figure 1

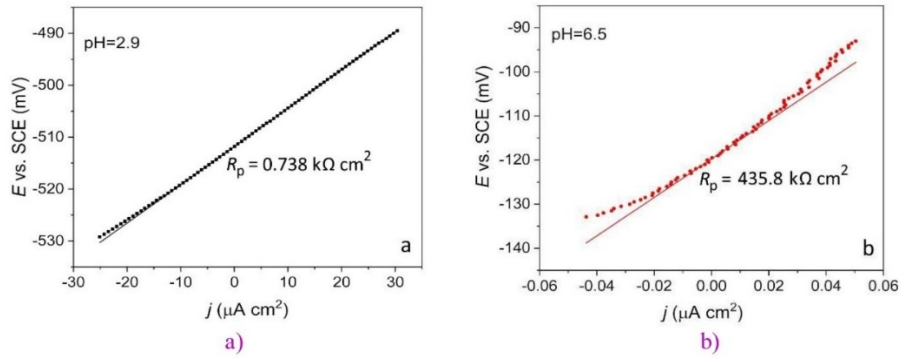

Figure 1 LPR diagrams in: a) acidic (pH=2.9) solution, b) neutral (pH=6.5) solution

The slope of the curve ($\Delta E/\Delta j$) at the corrosion potential (E_{corr}) corresponds to the polarization resistance (Rp) value. The Rp value in the acidic solution is significantly lower than in the neutral solution.

3.2 EIS measurements

Nyquist plots obtained in solutions with different pH values are shown in Figure 2a), with an enlarged view of the initial portion in Figure 2b).

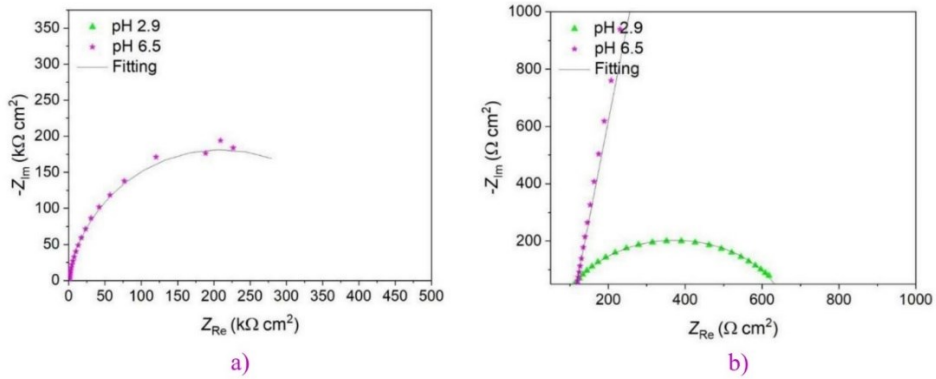

Figure 2 EIS diagrams for: a) Nyquist plot for the tested steel, b) Enlarged view of the Nyquist plot for the tested steel

The Nyquist plot (Figure 2a) displays the relationship between the real impedance component (Z_{Re}) and the imaginary impedance component ($-Z_{Im}$) in linear coordinates. The diameter of the semicircle corresponds to the polarization resistance (R_p) value. A larger diameter indicates a higher R_p value, and thus higher corrosion resistance.

The R_p values in acidic and neutral NaCl solutions are approximately 0.560 kΩ cm² and 420 kΩ cm², respectively. As expected, the tested steel demonstrates the lowest resistance to general corrosion in the acidic environment. This can be attributed to the high concentration of hydrogen ions in the acidic solution, which accelerates corrosion and leads to intense dissolution of the steel.

In the neutral solution, two-time constants are observed. One corresponds to electrochemical processes occurring in the passive layer, while the other corresponds to processes at the metal/passive layer interface. Since these time constants are associated with frequencies at the lower end of the spectrum, the experimental EIS results were fitted using a simplified Equivalent Electrical Circuit (EEC) (Figure 3), with a single time constant.

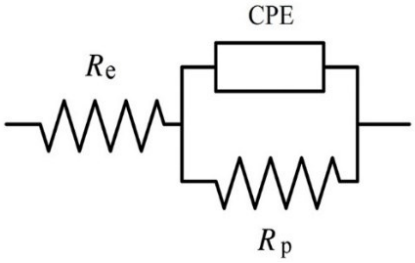

Figure 3 Equivalent electrical circuit (EEC) used for fitting EIS results (R_p - polarization resistance, R_e - electrolyte resistance, CPE- constant phase element)

In the EEC, the CPE replaces the double-layer capacitance (C_{dl}) at the surface of the tested steel. The CPE accounts for the microstructural inhomogeneities of the steel surface, such as surface roughness and segregation of alloying elements (Srinivasan and Fasmin, 2021). The effective capacitance of the passive film (C_{eff}) was determined using the Brug equation (Eq. 1) with the corresponding values for R_p, Q, and n (Hirschorn et al., 2010)

$$C_{eff} = R_p^{\frac{1-n}{n}} \cdot Q^{\frac{1}{n}} \quad (1)$$

The results obtained are presented in Table 2.

Table 2 Results of EIS measurements in acid and neutral solutions for the tested steel

pH	R_p (kΩ cm^2)	CPE		C_{eff}
		$Yo/10^{-6}$ (s Ω^{-1} cm^{-2})	n	(μF cm^{-2})
2.9	0.557	260.0	0.800	901.9
6.5	418.5	37.15	0.910	96.50

3.3 Summary of General (Uniform) Corrosion Measurements

Table 3 summarizes the results of electrochemical tests conducted using the LPR and EIS methods.

Table 3 Summary results (R_p) of electrochemical methods for the tested steel

pH	R_p (kΩ cm^2)	
	LPR	EIS
2.9	0.738	0.557
6.5	435.8	418.5

The results from both the LPR and EIS methods indicate that the general corrosion rate, as expressed by the value of R_p (Table 3), decreases with rising pH. The corrosion rate values obtained using both methods are in good agreement.

In a neutral environment, the formation of a passive layer on the steel surface significantly reduces the occurrence of corrosion reactions, allowing the steel to behave similarly to stainless steel.

3.4 Appearance of the sample surfaces before and after electrochemical testing

Figure 4 shows the surface of the steel sample before electrochemical tests (a) and after testing in acidic (b) and neutral (c) solutions.

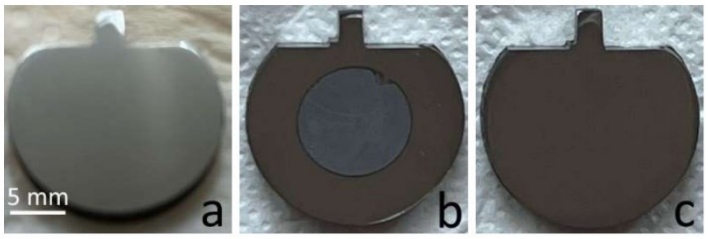

Figure 4 Sample surfaces a) before electrochemical tests, b) after electrochemical testing in pH 2.9 solution, c) after electrochemical testing in pH 6.5 solution

Before electrochemical testing (Figure 4a), no traces of corrosion or other damage are visible on the sample's surface, as proper sample preparation was ensured. In the acidic NaCl solution, intensive dissolution of the metal surface occurs in the anodic region, resulting in visible traces of dissolution on the sample surface (Figure 4b). In the neutral NaCl solution, the steel surface remains passive, and dissolution occurs at an extremely low rate only through the pores in the passive film, leaving the surface largely unaffected (Figure 4c).

4 CONCLUSION

The polarization resistance (R_p), corrosion current density (j_{corr}), and corrosion rate (v_{corr}) were used as indicators of the resistance to general (uniform) corrosion. As the pH value of the NaCl solutions increased, the tested steel exhibited higher corrosion resistance.

In the acidic NaCl solution, the steel did not enter a passive state and dissolved rapidly. In contrast, in the neutral NaCl solution, a passive layer formed on the steel surface, protecting it from further corrosion.

The corrosion rate results obtained using linear polarization resistance (LPR) and electrochemical impedance spectroscopy (EIS) methods are in good agreement, confirming the consistency of the electrochemical techniques employed.

ACKNOWLEDGEMENTS

This work was financially supported by the Ministry of Science, Technological Development and Innovation of the Republic of Serbia and the Ministry of Higher Education, Science and Innovation of the Republic of Slovenia, under the joint Serbia-Slovenia project for the period 2023-2025.

REFERENCES

ASTM A335 (2022) Standard Specification for Seamless Ferritic Alloy-Steel Pipe for High-Temperature Service.

BENDICK, W. and RING, M. (1996) Creep rupture strength of tungsten-alloyed 9-12 % Cr steels for piping in power plants. Steel Research, 67, pp. 382-385.

GARR, K., RHODES, C., and KRAMER, D. (1973) Effects of Microstructure on Swelling and Tensile Properties of Neutron-Irradiated Types 316 and 405 Stainless Steels, ASTM Selected Technical Papers, pp. 109-121.

HAARMANN, K. et al. (2002) The T91/P91 Book. Boulogne: Vallourec and Mannesmann Tubes.

HIRSCHORN, B., ORAZEM, M.E., TRIBOLLET, B., VIVIER, V., FRATEUR, I., and MUSIANI, M. (2010) Constant-phase element behavior caused by resistivity distributions in films: II. Applications. Journal of The Electrochemical Society, 157, C458.

LITTLE, E.A. (1972) Voids produced in mild steel by 1MeV electron irradiation. Radiation Effects, 16, pp. 135-137.

SRINIVASAN, R. and FASMIN, F. (2021) An introduction to electrochemical impedance spectroscopy. Boca Raton: CRC Press.

UNDERGROUND MINING ENGINEERING 46 (2025) 101-116 UDK 62
UNIVERSITY OF BELGRADE - FACULTY OF MINING AND GEOLOGY EISSN 2560-3337

Original scientific paper

THEORETICAL FUNDAMENTALS OF MECHANOCHEMICAL REACTIONS IN THE SOLID PHASE

Nataša Đorđević[1], Slavica Mihajlović[1], Milica Vlahović[2], Vladan Kašić[1], Srđan Matijašević[1], Mirko Grubišić[1]

Received: February 28, 2025 **Accepted:** April 23, 2025

Abstract: Chemical reactions in the solid phase are characterized by many specificities. The study of such reactions, with regard to the condensed state, eliminates the need to introduce many approximations that are common when considering reactions in the liquid phase or heterogeneous reactions, other laws, specific and inherent only to the solid state of matter. These make the scientific field of solid-state chemistry far more complex, due to the very strong need for a comprehensive multidisciplinary approach. The basic theoretical principles from the fields of physics, chemistry, physical chemistry and chemical technology are equally important. The article gives an example of mechanochemical synthesis of the neutralization type, and barium oxide as the base component and titanium oxide as the sisal component of the mixture are activated. In order to determine the changes that occur due to the mechanical activation of the starting materials, barium oxide and titanium oxide were ground in a stoichiometric ratio for 440 minutes. The analysis determined that a mechanochemical synthesis had taken place and that barium titanate with a degree of synthesis of 0.99 had been obtained. This was confirmed using X-ray structural analysis, which monitored the state of the activated material as a function of the time of activation.

Keywords: solid state, mechanochemical synthesis, barium titanate

1 INTRODUCTION

The possibility of achieving a chemical reaction between the reacting components of solid substances, without the phase of their dissolution and decomposition into ions, has always been attractive to chemists and encouraged constant research in the field of solid-state chemistry and physics. Regardless of whether the reaction is thermodynamically possible or not, the problem that needs to be overcome in initiating such reactions is

[1] Institute for Technology of Nuclear and Other Row Materials, Franše'd Eperea Boul. 86, Belgrade, Serbia
[2] University of Belgrade, Institute of Chemistry, Technology and Metallurgy, National Institute of the Republic of Serbia, Njegoševa St 12, Belgrade, Serbia

E-mails: n.djordjevic@itnms.ac.rs, ORCID: 0000-0002-2353-6751; s.mihajlovic@itnms.ac.rs, ORCID: 0000-0003-0904-3878; m.vlahovic@ihtm.bg.ac.rs, ORCID: 0000-0002-7893-9101; v.kasic@itnms.ac.rs, ORCID: 0000-0002-4430-567X; s.matijasevic@itnms.ac.rs, ORCID: 0000-0002-3897-8085; m.grubisic@itnms.ac.rs, ORCID: 0009-0007-9705-2796

initiating the beginning of the reaction, i.e. bringing the required amount of energy that will be equal to or greater than the required activation energy for that reaction and the conditions in which it should occur. takes place. For this reason, methods of realizing such reactions using thermal activation were mainly researched and developed. The method of mechanical activation, which also enables the creation of active (excited) and unstable states in a solid material, reveals completely new perspectives for accelerating such reactions. Therefore, it is possible to define several methods of application of mechanical activation for this purpose (Feng, Fahrenholtz and Brenner, 2021; Sani et al., 2017; Fang et al., 2018; Đorđević et al., 2022; Obradović et al., 2015):

- previous individual mechanical activation of the input components (or one of them) before thermal activation,
- previous simultaneous mechanical activation of the mixture of input components before thermal activation,
- realization of a chemical reaction directly during the communication of mechanical energy to the reaction system (mechanochemical method),
- realization of a chemical reaction by simultaneous application of mechanical and thermal activation (mechanothermic method).

Mechanochemical methods of conducting reactions in mixtures of solid materials, as well as methods of previous simultaneous mechanical activation, are extremely important for this issue.

In accordance with the basic principles of chemical thermodynamics, the direction of the chemical reaction and the degree of mutual reactivity of the starting reactants are determined by the isobaric-isothermal potential of the reaction ΔG (Wang et al., 2016; Pandey, Buljak and Balać, 2017). A reaction between chemical elements and compounds in the solid state is possible if:

$$\Sigma\Delta G_{products} - \Sigma\Delta G_{reactants} = \Delta G_{reactions} < 0 \quad (1)$$

For reactions of the type:

$$A_{ss} + B_{ss} \rightarrow C_{ss} + D_{ss} \text{ (or } AB_{ss}) \quad (2)$$

(ss-solid state)

$$\Delta G_{reactions} = \Delta G^{o}_{reactions} + RT\ln(a_C a_D / a_A a_B)$$

where aD, aC, aA, aB - activities of reaction products and reactants.

If solid substances are exposed to normal pressure and if their activities are equal or close to unity, then it is:

$$\Delta G_{reactions} = \Delta G^{o}_{reactions} \quad (3)$$

To determine the direction of the reaction, it is sufficient to know whether the value of ΔG of the reaction at standard conditions (T=298°K, p=0.1 MPa) is positive or negative. If the reaction is thermodynamically possible (ΔG < 0), then in a mixture of solid reactants it will theoretically go to the end.

If a liquid or gaseous phase appears as a product of the reaction or solid solutions are formed, then the influence of the term TΔS in the expression for the change in the isobaric-isothermal potential

$$\Delta G = \Delta H - T\Delta S \quad (4)$$

becomes very expressed, and then it is difficult to talk more about the ratio between the direction of the reaction and the sign of the □G value, because the entropy change in such processes can be both positive and negative. During the mechanical activation of solid materials, transformations and accumulation of released mechanical energy occur in the form of crystal lattice defects, displacement of atoms from their equilibrium positions, etc., which leads to an increase in enthalpy and entropy of the treated system. In a large number of cases, this change is significant, and then the change in free energy can be such that the reaction changes its direction. Insufficient study of those factors can lead to the conclusion of the alleged inconsistency of the obtained results with thermodynamic calculations (Ewais et al., 2017).

The characteristic features of chemical reactions in the solid phase are their progress in stages and the localization of the chemical process, which takes place only at the points of direct contact of the starting reactants. The following stages have the greatest influence on the kinetics of chemical processes in the solid phase (Kerbart et al., 2019): communicating the required amount of energy to initiate and start a chemical reaction, creation of the first nuclei of the chemical reaction product and diffusion of reactants through the layer of the resulting product.

The chemical reaction begins first on the most active parts of the surface of solid substances, namely the beginnings of dislocations, point defects of the crystal lattice, etc. This is where nuclei of chemical reaction products are formed, whose growth and fusion lead to the creation of a compact reaction zone. Diffusion transfer of reactants through the resulting product layer represents a slow step in the further course of the reaction and can take place according to different mechanisms. In any case, by acting on the slow stage of the process, it is possible to act on the speed of the chemical reaction in the solid phase. Mechanical activation of the mixture of solid reactants is one of the most effective ways to eliminate the interference during the reaction caused by the diffusion of reactants through the layer of the resulting product.

In order to understand and clarify the phenomena that accompany mechanochemical reactions, it is necessary to monitor and clarify the factors that make mechanochemical

reactions specific. These factors are primarily the local pressure and temperature that occur at the points of collision of reactants with grinding bodies, as well as specific phenomena that occur during plastic flow of materials. Thus, the impulsive nature of local temperatures can give a mechanochemical reaction a completely different course compared to reactions between the same reactants that take place with gentle heating. When multiple parallel or subsequent reactions are possible in the combination of two or more reactants, only those that are thermodynamically possible in a short-term thermal impulse at the moment of collision will occur during mechanical activation (Marc et al., 2013). In addition, when it is taken into account that most of the mechanical energy during mechanical activation is transformed into thermal energy, it is clear that heat has a significant impact on the course and outcome of mechanochemical reactions.

1.1 Mechanochemical syntheses

Mechanochemical synthesis refers to chemical reactions that take place in the solid phase, initiated by mechanical energy input, in mechanochemical reactors (special mills, disintegrators, etc.), and in which one or more reactants are obtained from two or more reactants, according to a clearly defined chemical reaction new substances - reaction products. Figure 1 schematically shows the transformations during the mechanochemical process (Raghu, Nampoothiri and Satish Kumar, 2018).

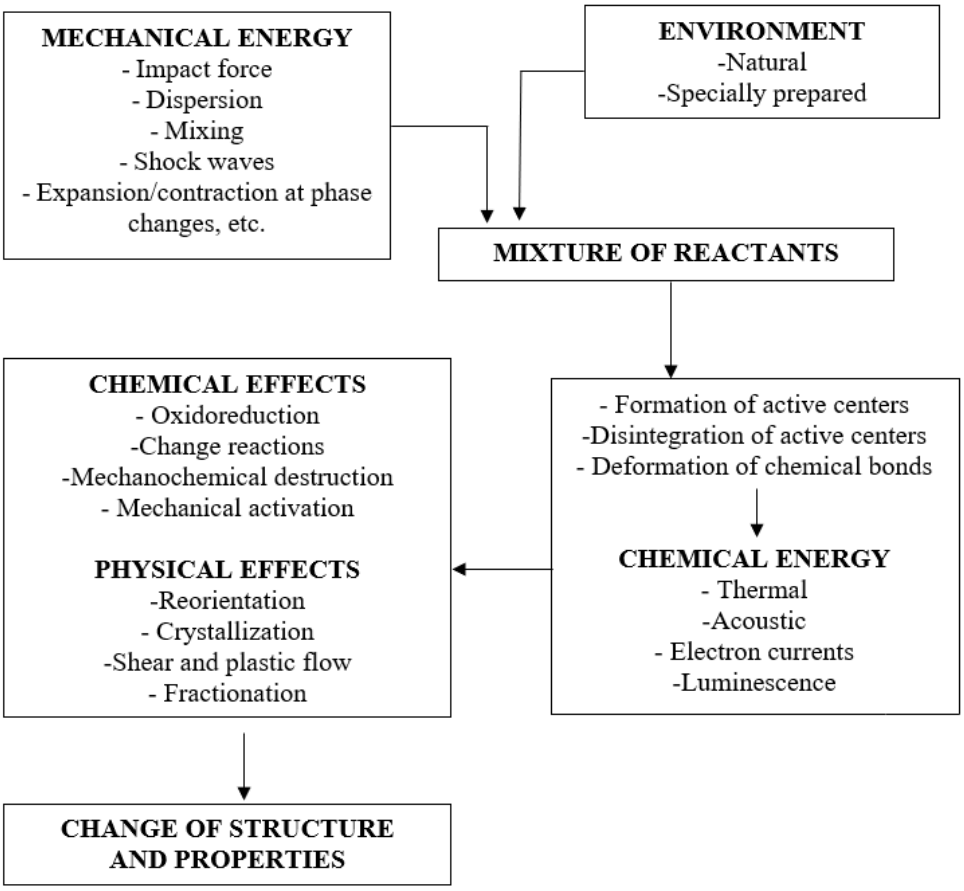

Figure 1 Schematic view of mechanochemical transformations

It is noticeable that during the mechanochemical process, in addition to the chemical reaction, a number of other transformations take place, which directly or indirectly affect the course and result of the chemical reaction. If the subject of scientific study is precisely the chemical reaction that takes place in the solid phase during the mechanochemical process, then the study of other, parallel, effects and transformations is aimed at elucidating and defining the kinetics, mechanism, and other essential features of the mechanochemical reaction.

Considering all forms of chemical reactions in general, it is most correct to divide them into two general groups: chemical reactions in which oxidation-reduction changes occur in elements that are part of the reacting chemical compounds and reactions in which such changes do not occur. However, for the study of mechanochemical reactions, it is necessary to make a more detailed division that more clearly specifies the final outcome of a mechanochemical reaction. In this way, it is possible to more clearly specify the

conditions under which the mechanochemical process will take place, and thus it is easier to control and manage parallel effects that decisively affect the parameters of the microenvironment in which the chemical process takes place. In this regard, perhaps the most appropriate division of mechanochemical reactions into (Ewais et al., 2017): neutralization reactions, ion exchange reactions, union reactions i redox reactions. It has been shown in previous research (Marc et al., 2013) that this division enables a fairly precise division of the parameters of mechanochemical processes, as well as the division of parameters related to the choice of reactants (thermodynamic parameters and other physical and chemical characteristics of reacting substances and possible reaction products).

1.1.1 Mechanochemical reactions of neutralization

If one strictly starts from the basic principle of mechanochemistry, that mechanochemical reactions take place exclusively in the solid phase, then mechanochemical reactions of neutralization could be called those chemical reactions that take place under the influence of mechanical energy between oxides-anhydrides of acids and oxides-anhydrides of the corresponding hydroxides, with the condition that both substances are in a solid state under normal conditions (Pandey, Buljak and Balać, 2017). Such, for example, are the reactions between WO_3, MoO_3, SiO_2, TiO_2, V_2O_5, Fe_2O_3, etc. as one reactant, (anhydrides of corresponding acids) and BaO, CaO, MgO, SrO, NiO, CoO, etc. as a second reactant (oxide bases of corresponding hydroxides). (Lazarević et al., 2009; Li and Shih, 1997).

Such reactions take place according to the general equation:

$$Me^{I}O + Me^{II}O_n = Me^{I}Me^{II}O_{n+1} \quad (5)$$

where n = 2, 3, etc.

However, it is advisable to expand the list of potential reactants for mechanochemical neutralization reactions with the following groups of reactants: all hydroxides, acids that under normal conditions are in a solid state and carbonates, formed from basic oxides and corresponding hydroxides (Raghu, Nampoothiri and Satish Kumar, 2018).

Regardless of the fact that hydroxides and acids contain constitutional water, which in their mutual reaction will certainly be a product of the reaction, thus potentially introducing a liquid phase into the reaction system, it is also a fact that a large number of salts, formed in neutralization reactions, crystallize together with water, that is, in their crystal structure, and thus in their chemical composition, they contain a certain number of water molecules. Crystalline water constitutes that substance by its physical and chemical characteristics, which is essentially different from the same but anhydrous substance. When it comes to carbonates, there are two important reasons that make them suitable for being classified as reactants in mechanochemical neutralization reactions:

- the carbonate ion, as the base of extremely weak carbonic acid, allows carbonates to retain most of the properties of hydroxides and basic oxides from which they were formed;
- the product of the mechanochemical reaction of neutralization, in which the appropriate carbonate participates instead of hydroxide or basic oxide, will be gaseous carbon dioxide, which, if the process takes place in an open system, will immediately leave the reaction zone, so that it will not interfere with the further flow and outcome of the reaction.

Bearing all this in mind, as well as the results of previous research, it can be assumed that mechanochemically activated substances will react with each other in the solid phase by the mechanisms of neutralization reactions and in the case of binary systems of the general type: acid/acid anhydride + metal (hydr)oxide/metal carbonate (Lazarević et al., 2009; Li and Shih, 1997; Avvakumov, Senna and Kosova, 2001; Đorđević, Vlahović and Mihajlović, 2023).

Neutralization reactions in mechanochemical syntheses are interesting for research, and one of these reactions is the preparation of bismuth titanate from bismuth and titanium oxides. In the article of the group of authors (Lazarević et al., 2009), mechanochemical activation of a stoichiometric powder mixture $2Bi_2O_3$ and $3TiO_2$ was performed, and the compound $Bi_4Ti_3O_{12}$ was obtained. Powder X-ray diffraction was used to monitor the intermediate product as well as the product obtained after the optimal activation time. The authors investigated the mechanochemical activation of the mixture $2Bi_2O_3$ and TiO_2, where the activation was performed in a planetary ball mill (Li and Shih, 1997). To monitor the parameters (change in crystallite size, the presence of an amorphous phase and the product obtained by transforming the initial components, they were monitored by the method of X-ray diffraction analysis. The authors of the paper (Li and Shih, 1997) established that there was deformation of the crystal lattice and destruction of the structure of the starting material. After a certain amount of grinding, the analysis showed that they obtain highly disordered, amorphous/nanocrystalline structure.

1.1.2 Mechanochemical reactions of ion exchange

Studies of mechanochemical reactions of ion exchange have shown that this type of reaction, when it takes place in the solid phase, strictly obeys the laws of chemical kinetics and chemical thermodynamics Namely, it was established that the exchange of ions in a mixture of two chemical compounds (salts) occurs kinetically exactly as it can be predicted, considering the strength of the acids or bases, from which the reacting salts were formed (Avvakumov, Senna and Kosova, 2001).

1.1.3 Mechanochemical oxido-reduction reactions

This type of mechanochemical reactions, considering the nature of possible reactants, is reduced mainly to reactions of metal oxides with elemental metals, non-metals and metal

sulfides (Gonzales et al., 2017). All these reactions can be represented by the following general equations:

$$Me^{I}O_{n/2} + n/mMe^{II} = Me^{I} + Me^{II}{}_{n/m}O_{n/2} \quad (6)$$

$$MeO_{n/2} + n/4xC = Me + n/4xCO_2 \quad (7)$$

$$MeO_{n/2} + n/4xSi = Me + n/4xSiO_2 \quad (8)$$

$$MeS + 2\,MeO = 3Me + SO_2 \quad (9)$$

$$Me^{I}S_2 + Me^{II}O_2 = Me^{I}S + Me^{II}O + SO_2 \quad (10)$$

In Eq. 6, n and m are the degrees of oxidation of metals Me^{I} and Me^{II} in the corresponding oxides, respectively. In Eq. 7 and 8, n is the degree of oxidation of metal Me in the corresponding oxides. It has been shown that these reactions, when they take place in the solid phase, obey to a large extent the predictions that can be made based on the thermodynamic parameters of the corresponding reactions.

1.1.4 Mechanochemical reactions of compounding

Mechanochemical joining reactions have been the most frequently studied so far, and there are the most achieved results in that area. This statement refers both to the number of processed and tested combinations of reactants, as well as to the study of the kinetics and mechanism of the process and the characteristics of the obtained products. The most numerous groups consist of works in which the possibility of mechanochemical production of substances such as complex oxides, carbides, nitrides and hydrides is studied. Different possibilities of obtaining were examined, and two directions were mostly considered: previous individual mechanical activation of the starting substances and simultaneous mechanical activation of those substances that participate in the construction of the final material. The essence and goal of mechanochemical joining reactions is to obtain substances with specific physical and especially crystallographic characteristics. Namely, all these works are carried out with the aim of obtaining materials for specific purposes: ceramics, metal-ceramics, glass, metal-glass, superconductors, additives for alloying, etc. In the mechanochemical process of joining, the entire transformation during the process takes place between the reacting particles of the nanometer-sized particles, and the specific properties of the obtained material result

primarily from the phenomena that occur on particles of these sizes. For this reason, in recent years, the terminology in this field has been adapted to this knowledge, so often the materials obtained in mechanochemical reactions of union are called nanomaterials, nanopowders, nanocrystalline powders, etc. (Kavairasu and Ravichandran, 2020; Zhang, et al., 2020).

2 EXPERIMENTAL PART

The authors of this paper are involved in experimental research in the field of mechanochemical activation and mechanochemical synthesis. Therefore, here we will present the results obtained from the solid-state synthesis process, specifically neutralization reactions in the mechanochemical synthesis reaction. The aim was to support the theoretical considerations of the basis of neutralization reactions presented in the introductory, theoretical, part of the paper with concrete results.

2.1 Materials and methods

For the experimental research presented in the paper, the starting components barium oxide BaO, as a basic reactant and titanium dioxide TiO_2 as an acid, were used. Barium oxide manufactured by FLUKA (Switzerland), CAS No. was used in the experiments. [1304-28-5], quality pure and TiO_2 produced by MERCK (Germany), CAS No. [13463-67-7], pro analysis quality.

Recalculated according to reaction 6, the amount of starting substances consisted of 0.5 mol (76.7 g) BaO and 0.5 mol (39.9 g) TiO_2, so the total amount of starting material amounted to 116.6 g.

$$BaO(s) + TiO_2(s) = BaTiO_3(s) \text{ (or } BaO{*}TiO_2) \quad (11)$$

Chemical analysis. Chemical analysis was conducted using a Perkin Elmer Analyst 703 Atomic Absorption Spectrophotometer (AAS).

Procedures of mechanochemical synthesis. The mechanochemical synthesis of BaO and TiO_2 was performed in a high-energy vibration mill with torsion springs and annular working elements, manufacturer KHD Humboldt Wedag A.G., Germany, type MH954/3. The starting powders were activated for 440 minutes. The motor power of the mill used was 0.8 kW.

During the mechanochemical synthesis, samples were taken at 30, 110, 200, 290, and 440 min of activation, and X-ray structural analysis were performed. In this way, both starting components and products of mechanochemical processes are identified and monitored.

X-ray analysis. The samples were recorded and analyzed diffractometrically on an automated diffractometer with a copper tube PHILIPS PW-1700, which operates at 40

kV and 35 mA. The device is supplied with a graphite monochromator and a proportional counter, filled with xenon. The imaging angle (2θ) from 4 to 15° was used.

3 RESULTS AND DISCUSSION

3.1 Characterization of starting components

The starting components, BiO and TiO_2, which were used in the neutralization reaction were chemically analyzed and X-ray analysis was performed on the samples. X-ray diffractograms have been shown in previously published works, so only characteristic peaks are tabulated in this paper. They are important for monitoring the synthesis and formation of a new compound through the neutralization reaction that the authors wanted to show in this paper (Đorđević et al., 2023).

Table 1 shows the chemical characteristics of barium oxide.

Table 1 Chemical characterization of barium oxide

Content (acidimetric), min %	98
Substances insoluble in HCl, max %	0.005
Impurities, max%	
Carbonates (as CO_2)	0.5000
Chlorides (Cl)	0.0050
Sulfates (SO4)	0.0010
Total Nitrogen (N)	0.0020
Arsene (As)	0.0001
Calcium (Ca)	0.0200
Iron (Fe)	0.0050
Potassium (K)	0.0050
Sodium (Na)	0.2500
Lead (Pb)	0.0010
Loss on ignition, max %	0.5

The previously performed X-ray analysis confirmed the crystal structure of BaO and identified two characteristic peaks at certain wavelengths, which is shown in Table 2.

Table 2 Characteristic diffraction maxima of BaO

Pick no.	**d-value**	**Angle 2Θ**
1	3.2895	27.085
2	2.6771	33.445

Table 3 shows the chemical characteristics of titanium dioxide, while Table 4 shows the characteristic peaks obtained by X-ray diffraction, which confirmed its crystal structure.

Table 3 Chemical characterization of titanium dioxide

The content, %	99.0-100.5
Substances soluble in water, max %	0.5
Substances soluble in HCl, max %	0.5
Impurities, max%	
Heavy metals (like Pb)	0.0020
Acid-soluble antimony (Sb)	0.0002
Sulfates (SO_4)	0.0010
Total nitrogen (N)	0.0020
Acid-soluble barium (Ba)	0.0002
Arsenic (As)	0.0001
Iron (Fe)	0.0050
Acid-soluble lead (Pb)	0.0010
Zinc (Zn)	0.0005
Loss on ignition at 800°C, max%	0.5
Loss on drying at 105°C, max%	0.5

Table 4 Characteristic diffraction maxima of TiO_2

Pick no.	**d-value**	**Angle 2 Θ**
1	3.5133	25.330
2	2.3778	37.805
3	1.8926	48.035
4	1.6667	55.055
5	1.4806	62.700

3.2 Results of mechanochemical synthesis

The neutralization reactions between Bao and TiO2 and the formation of barium titanate were monitored by X-ray analysis of samples taken at precisely determined time intervals. (30, 110, 200, 290, and 440 min).

Figure 2 shows a comparative overview of X-ray structural analyses of the mechanochemical synthesis of barium titanate during activation.

The broadening of diffraction lines and their insignificant intensity indicate that after 30 minutes there was a significant disruption of the crystal structure of the initial reactants, especially titanium dioxide, whose crystal structure was very clearly expressed before the start of the reaction (Figure 2). The analysis of the registered peaks and corresponding

diffraction angles confirmed the presence of initial reactants, but also the beginning of the formation of the product-barium titanate under some of the characteristic diffraction angles for this substance.

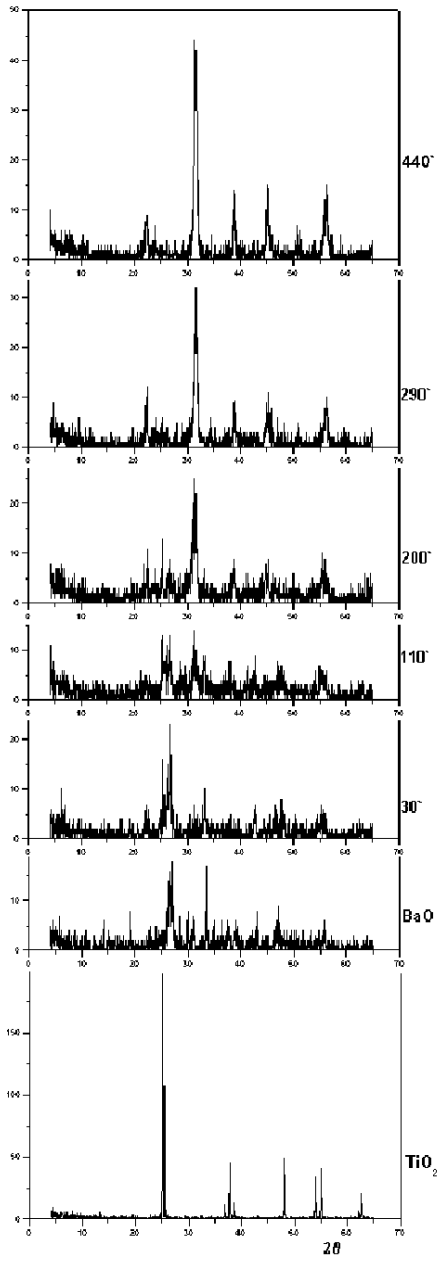

Figure 2 Comparative review of X-ray structural analyzes of the mechanochemical synthesis of barium titanate

The first phase takes place in the first 30 minutes of activation of the starting components and is the phase of progressive destruction of the crystal structure of the reactants. This part of the research has already been presented in the paper (Đorđević, Vlahović and Mihajlović, 2023). After the 30th minute of activation, subsequent X-ray structural analyzes showed that the characteristic peaks for the initial components are increasingly lost, and new ones are created (assuming that these are intermediate compounds).

It can be noted that the mechanical energy introduced into the reaction system, in this level, is mainly spent on the destruction of the crystalline structure of the starting reactants and their significant amorphization. The mechanochemical activation of individual substances (as well as the combination of two or more substances) leads to the transformation of the released mechanical energy and its accumulation in the treated material in the form of accumulated deformations of the crystal lattice, extremely developed and active specific surface of the material, whereby the material is brought to an elevated level of energy content. Further activation provides by introducing energy into the reaction system, which overcomes the energy barrier on the reaction path to the reaction product, so the chemical reaction irreversibly flows towards the expected product.

The final result of the X-ray structural analysis showed that after 440 minutes of activation, we obtained the final product, barium titanate, with a degree of synthesis of 99% (η=0.99). Initial components were not detected in the traces either, and further activation in the vibro mill did not lead to new changes in the structure. This results in an increased degree of potential energy, i.e. chemical reactivity of the material. Considering that the reaction involved pure and unactivated reactants that exist as elementary particles (BaO and TiO_2 molecules) as reactants during the mechanochemical reaction, it is concluded that the reaction of the mechanochemical synthesis of barium titanate proceeds in two phases. The first phase is mutual collisions between the molecules of two reactants, during which an activated complex is formed, which stoichiometrically correspond to the chemical composition of barium titanate, but in terms of structure and characteristics of chemical bonds, it represents a special compound.

4 CONCLUSION

Chemical reactions in the solid phase are specific in relation to other chemical reactions and different chemical laws apply to them, which are characteristic only for this aggregate state. Considering that the reactants remain in the solid phase, the action of the particles that enter the reaction is much more complex and requires a multidisciplinary approach. A particularly interesting area of solid-state reactions is mechanochemical synthesis, which depends on many input parameters. In addition to the input components, the device in which the synthesis process takes place, the type of activator, and the energy invested in the activation and synthesis process are also of great importance. Modern

methods of monitoring the processes that take place in such devices, the application of modern scientific achievements in the fields of mechanics, crystallography, chemical thermodynamics, chemical kinetics, physical electronics, help to understand the complex processes that occur in activators.

As an example of mechanochemical synthesis in neutralization reactions in the solid state, an example of obtaining barium titanate from the initial components barium oxide and titanium oxide, where barium oxide (BaO) was used as a basic reactant, and titanium dioxide (TiO_2) as an acidic reactant, is given. The experiments showed that after 440 minutes of activation, the initial components were completely synthesized into the final barium titanate product, with a utilization rate of 99%. X-ray structural analysis after this activation time did not detect traces of the initial components, but only the final product.

ACKNOWLEDGEMENT

The authors would like to thank the Ministry of Science, Technological Development and Innovation of the Republic of Serbia for the financial support of the research, the results of which are presented in the paper (contract 451-03-136/2025-03/200023 and 451-03-66/2024-03/200026).

REFERENCES

AVVAKUMOV, E.G., SENNA, M and KOSOVA, N. (2001) Soft Mechanochemical Synthesis-A Basis for New Chemical Technologies, Chapter 3: Some Theoretical Aspects of Mechanochemical Reactions. 1th ed., New York: Springer. https://doi.org/10.1007/b114163

ĐORĐEVIĆ, N. et al. (2022) Thermal analysis and phase changes of mechanochemically activated sodium carbonate. Thermochimica Acta, 708, 179139. https://doi.org/10.1016/j.tca.2021.179139

ĐORĐEVIĆ, N., VLAHOVIĆ M. and MIHAJLOVIĆ, S. (2023) X-ray structural analysis of the BaO and TiO2 starting compounds and initial mechanochemical activation. Undeground Mining Engineering, 42, pp. 37-46. https://doi.org/10.5937/podrad2342037Q

EWAIS, E.M:M. et. al. (2017) Synthesis of nanocrystalline MgO/MgAl2O4 spinel powders from industrial wastes. Journal of Alloys Compounds, 691, pp. 822-833. https://doi.org/10.1016/j.jallcom.2016.08.279

FANG, ZZ. et al. (2018) Powder metallurgy of titanium-past, present, and future. International Materials Reviews, 63 (7), pp. 407-459. https://doi.org/10.1080/09506608.2017.1366003

FENG, L., FAHRENHOLTZ, W.G. and BRENNER, D.W. (2021) High-Entropy ultra-high-temperature borides and Carbides: a New class of materials for extreme environments. Annual Review of Materials Research, 51, pp. 165-185. DOI: 10.1146/annurev-matsci-080819-121217

GONZALES, F. et al. (2016) General aspects of redox chemistry. Basic Terms and Theories-Encyclopedia of Physical Organic Chemistry, Wiley Online Library, pp.1-19. https://doi.org/10.1002/9781118468586.epoc1015

KAVAIRASU, C. and RAVICHANDRAN, M. (2020) Nanomaterials through Powder Metallurgy: Production, Processing, and Potential Applications toward Energy and Environment. Handbook of Nanomaterials and Nanocomposites for Energy and Environmental Applications. Springer, pp. 1-40. DOI: 10.1007/978-3-030-11155-7_127-1

KERBART, G. et al. (2019) Pressure-assisted microwave sintering: A rapid process to sinter submicron sized grained MgAl2O4 transparent ceramics. Journal of the European Ceramic Society, 39 (9), pp. 2946-2951. https://doi.org/10.1016/j.jeurceramsoc.2019.03.046

LAZAREVIĆ, Z.Ž. et al. (2009) Study of Barium Bismuth Titanate Prepared by Mechanochemical Synthesis. Science of Sintering, 41 (3), pp. 329-335. https://doi.org/10.2298/SOS0903329L

Li, X. and Shih, W. (1997) Size Effects in Barium Titanate Particles and Clusters. Journal of the American Ceramic Society, 80 (11), pp. 2844-2852. https://doi.org/10.1111/j.1151-2916.1997.tb03202.x

MARC, D. et al. (2013) Fifty Years of Research and Development Coming to Fruition; Unraveling the Complex Interactions during Processing of Transparent Magnesium Aluminate (MgAl2O4) Spinel. Journal of the American Ceramic Society, 96 (11), pp. 3341-3365. DOI: 10.1111/Jace.12637

OBRADOVIĆ, N. et al. (2015) The Influence of Compaction Pressure on the Density and Electrical Properties of Cordierite-based Ceramics. Science of sintering, 47 (1), pp.15-22. DOI: 10.2298/SOS1501015O

PANDEY, S., BULJAK, V. and BALAĆ, I. (2017) Reduced order numerical modeling for calibration of complex constitutive models in powder pressing simulations. Science of Sintering, 49 (3), pp. 331-345. https://doi.org/10.2298/SOS1703331P

RAGHU, R., NAMPOOTHIRI, J. and SATISH KUMAR T. (2018) In-situ generation of MgAl2O4 particles in Al-Mg alloy using H3BO3 addition for grain refinement under ultrasonic treatment. Measurement, 129, 389-394. https://doi.org/10.1016/j.measurement.2018.07.056

SANI, E. et al. (2017) Titanium diboride ceramics for solar thermal absorbers. Solar Energy Materials and Solar Cells, 169, pp. 313-319. https://doi.org/10.1016/j.solmat.2017.05.038

WANG, F. et.al. (2016) Effect of MoO3 on microstructure and mechanical properties of (Ti,Mo)Al/Al2O3 composites by in situ reactive hot pressing. Ceramics International, 42 (1), pp. 1-8. DOI: 10.1016/j.ceramint.2015.08.138

ZHANG, Z. et al. (2020) Synthesis of a novel dual layered double hydroxide hybrid nanomaterial and its application in epoxy nanocomposites. Chemical Engineering Journal, 381, 122777. https://doi.org/10.1016/j.cej.2019.122777

UNDERGROUND MINING ENGINEERING 46 (2025) 117-122 UDK 62
UNIVERSITY OF BELGRADE - FACULTY OF MINING AND GEOLOGY EISSN 2560-3337

Original scientific paper

URANIUM(VI) ADSORPTION ON NATURAL AND MODIFIED CLINOPTILOLITE MINERAL

Srđan Matijašević[1], Nataša Đorđević[1], Slavica Mihajlović[1], Mirko Grubišić[1], Milica Vlahović[2]

Received: March 3, 2025 **Accepted:** March 21, 2025

Abstract: In this paper the investigation results of adsorption of uranyl ion on unmodified and acid modified clinoptilolite are presented. Adsorption was investigated at different amounts of adsorbents in suspension, different concentrations of uranyl ion in solution, as well as at different pH values.

Keywords: Zeolite, Adsorption, Uranyl ion

1 INTRODUCTION

Uranium is the most important element for the nuclear industry. It has a long half-life and is observed to have a coordination chemistry consisting of multiple stable oxidation states and stable solid and aqueous forms within the ecosphere. Under standard environmental conditions, uranium typically occurs in the hexavalent form as the mobile, aqueous uranyl $(UO_2)^{2+}$ ion (Sylwester, Hudson and Allen, 2000).

Adsorption of uranium (VI) ion onto various solids is important from purification, environmental and radioactive waste disposal points of view. In the last decades, the adsorption of uranium (VI) on activated carbon, metal oxides, as well as on natural and modified aluminosilicate adsorbents, has been the subject of many investigations (Seaman, Meehan and Bertsch, 2001, Chisholm-Brause et al.2001, Bors, Dultz and Riebe, 1999).

[1] Institute for Technology of Nuclear and Other Mineral Raw Materials (ITNMS), 86 Franshet d' Esperey St., 11000 Belgrade, Serbia
[2] University of Belgrade, Institute of Chemistry, Technology and Metallurgy, National Institute of the Republic of Serbia, Njegoševa 12, 11000 Belgrade, Serbia

E mails: s.matijasevic@itnms.ac.rs, ORCID 0000-0002-3897-8085; n.djordjevic@itnms.ac.rs, ORCID 0000-0002-2353-6751; s.mihajlovic@itnms.ac.rs, ORCID 0000-0003-0904-3878; m.grubisic@itnms.ac.rs, ORCID 0009-0007-9705-2796; m.vlahovic@ihtm.bg.ac.rs, ORCID 0000-0002-7893-9101

2 EXPERIMENTAL

X-ray diffraction (XRD) was employed for the identification of the mineral composition of the starting sample (Phillips PW/1710). The quantitative chemical analysis of the samples was conducted by the silicate method, SiO_2 content and I.L. (loss on annealing at 1000°C) were determined gravimetrically, while the oxide content Na_2O, K_2O, Fe_2O_3, CaO, MgO after destruction of the sample by melting, were determined by analyzing the content of their cations in the solution using the method of atomic absorption spectrometry (AAS).

The cation exchange capacity (CEC) of clinoptilolite was measured by the method of ion exchange with ammonium chloride (Matijašević et al., 2006), while its external cation exchange capacity (ECEC) was determined using the method of Ming and Dixon (Ming and Dixon, 1987). The suspensions were filtrated and the concentrations of exchanged Ca^{2+}, Mg^{2+}, Na^{+} and K^{+} were measured in the supernatants using AAS. Results expressed in centimole of charge per kg, represents the total CEC (ECEC). Hydrochloric acid (1M) was used for the preparation of the acid-modified zeolite (H-zeolite). The constant quantity of zeolitic tuff (100 g) was mixed with 1000 ml of acid solutions in a turbo mixer at 6000 rpm for 60 minutes at 50°C. The H-zeolite was rinsed with distilled water until Cl- ions were no longer detected and then dried at 60°C.

Adsorption of uranium(VI) on a natural zeolitic mineral as well as on H-zeolite was carried out by the batch technique. Uranium(VI) solutions were prepared using uranyl nitrate hexahydrate ($UO_2(NO_3)_2 \cdot 6H_2O$) (Sigma-Aldrich Co).

The preliminary batch studies were carried out by shaking known amounts of each adsorbent (natural and modified zeolite) and uranium (VI) solution, at room temperature for at least 24 h, at pH 6. In order to investigate the influence of the amount of adsorbents in suspension on uranium (VI) adsorption, at pH 6, the experiments were performed as follows: the volume of solution (50 ml) and the concentration of uranium (VI) (50 mg/l) were kept constant while the amount of adsorbent varied from 0.5 to 2.5 g. The suspensions were shaken for 2 h, at room temperature. After the reaction time, the solids were separated by centrifugation and in supernatants, the remaining uranium (VI) concentration was determined.

In order to investigate uranium (VI) adsorption isotherms on H-zeolite, to each tube 0.125 g of adsorbent and 50 ml of uranium (VI) solution were added at concentrations of 10, 20, 25, 30, 40, 50 mg/l. The adsorption of uranium (VI) ion on H-zeolite was studied at different pH values, with each sample being done in duplicate. The amount of uranium (VI) adsorbed on H-zeolites was calculated from the differences between the initial uranium (VI) concentration and the uranium (VI) concentration in solution after equilibrium. Since, at pH higher than 8.5, precipitation of yellow uranyl carbonate complex was noticed, all experiments were done in pH region from 3 to 8. The pH was

adjusted with HNO_3 and NaOH. The samples were shaken for 2 h, centrifuged at 10000 rpm for 10 min and uranium(VI) concentration was measured in supernatants.

Uranium (VI) concentration in solutions were determined using fluorometric method based on the fluorescence of U in fused mixture of NaF, Na_2CO_3 and K_2CO_3 (Rathore, 2008).

3 RESULTS AND DISCUSSION

The starting material used in these experiments was a natural zeolitic mineral from Beočin deposit (Fruška Gora, Serbia). Based on the qualitative mineralogical analysis, the content of clinoptilolite was over 80%, while the accessory minerals were quartz, feldspar, mica, calcite and clay minerals. The starting material had the following chemical composition: SiO_2–56.00%, Al_2O_3–14.40%, Fe_2O_3–1.86%, CaO–6.20%, MgO–2.64%, Na_2O–0.52%, K_2O–2.67%, I.L.–15.71%, while H-zeolite had:SiO_2–81,22%, Al_2O_3–10,85%, Fe_2O_3–1,51%, CaO–1,31%, MgO–0,35%, Na_2O–0,48%, K_2O–2,51%, I.L.–1.77% (AAS Perkin Elmer 703).

The cation exchange capacity (CEC) of the zeolitic tuff was 168 cmolc/kg (H-zeolite was 30.62 cmolc/kg) and the external cation exchange capacity (ECEC) was 10.4 cmolc/kg.

In order to determine the equilibrium time for uranium(VI) adsorption on H-zeolite, the kinetics of adsorption was investigated. It was found that adsorption begins very fast and that the most of uranium(VI) ion is adsorbed in less than 2 hours (>95%). Practically there were no changes in adsorption within the next 48 h. Based on these results subsequent adsorption experiments were conducted with 2 hours reaction time.

Preliminary uranium(VI) ion adsorption experiments on natural unmodified zeolitic mineral at mass ratio adsorbent: uranium(VI) ion 1000: 1, at pH 6, showed that uranium(VI) adsorption index was 34.8% (0.34 mg uranium(VI)/g adsorbent), while uranium(VI) adsorption on H-zeolite, at pH 6, was 95.3% (0.92 mg uranium(VI)/g adsorbent). At mass ratio adsorbent : uranium(VI) ion 400: 1 adsorption index was 93.1 (2.25 mg/g) on H-zeolite and at mass ratio adsorbent: uranium(VI) ion 200:1 index was 63% (3.04 mg/g) on H-zeolite (Fig.1).

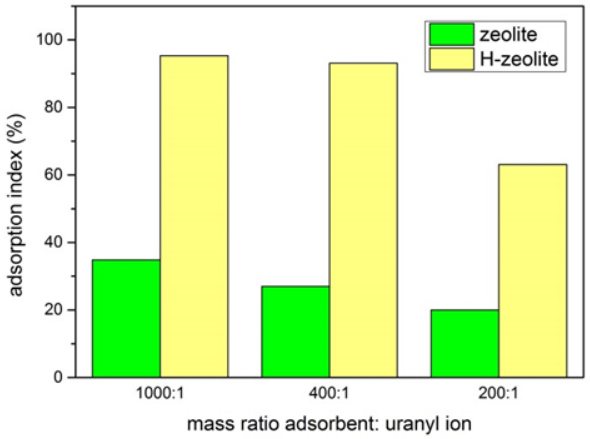

Figure 1 Adsorption index of uranium(VI) at different mass ratio adsorbent: uranyl ion

Acid modified zeolite with hydrochloric acid significantly increases adsorption of uranyl ion. The acid treatment eliminates the impurities of the zeolite through the replacement of natural zeolite cations with H^+ cations and raises the surface area and microporosity (Oztas, Karabakan and Topal, 2008, Castaldi et al.,2008, Matijašević et al., 2016).

Further results at mass ratio adsorbent: uranium(VI) 50:1 and at three different pH are shown at Figure 2.

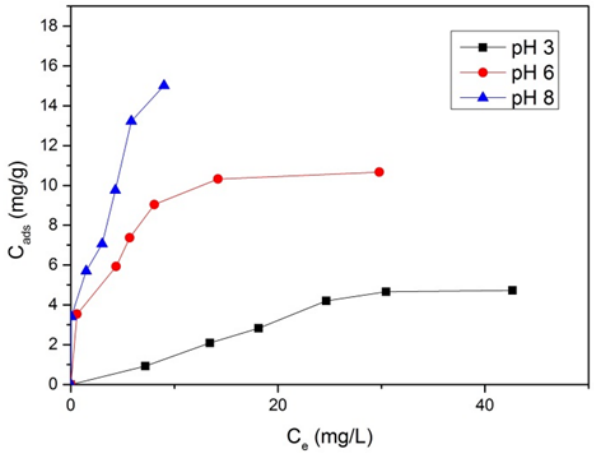

Figure 2 Adsorption index of uranium(VI) at three different pH for acid modified zeolite

As can be seen from Fig. 2, uranium(VI) adsorption on H-zeolite, at pH 3 and pH 6 according to IUPAC classification, is well described by the Langmuir type of isotherm (Type I) while adsorption at pH 8 is described by Type V isotherm.

The adsorption maximum calculated from linear plots gives estimates of the H-zeolite adsorption capacity for uranium(VI) ion. The calculated maximum is 4.72 mg/g at pH 3, 10.48 mg/g at pH 6 and 15.01 mg/g at pH 8. Results demonstrated that presence of H-ions in zeolite improve adsorption of uranium(VI) ion and that adsorption increases in following order pH 8> pH 6> pH 3.

4 CONCLUSION

The results reported in this paper demonstrated that H-zeolites obtained by acid modification of zeolitic mineral clinoptilolite are effective for the removal of uranium(VI) from water solution. The availability of clinoptilolite, their low cost and simple procedure for preparation of H-zeolites are the main advantages for production of large quantities of these materials. Concerning all this, H-zeolites as adsorbents, provide promising materials for removal of uranium(VI) from contaminated soils and groundwater systems.

ACKNOWLEDGEMENT

The authors would like to thank the Ministry of Science, Technological Development and Innovations of the Republic of Serbia for support (Grant No: 451-03-136/2025-03/200023, and 451-03-66/2024-03/200026).

REFERENCES

SYLWESTER, E. R., HUDSON, E. A. and ALLEN, P. G. (2000) The structure of uranium (VI) sorption complexes on silica, alumina, and montmorillonite. *Geochimica et Cosmochimica Acta*, 64 (14), pp. 2431-2438. https://doi.org/10.1016/S0016-7037(00)00376-8

SEAMAN, J. C., MEEHAN, T. and BERTSCH, P. M. (2001) Immobilization of nickel and other metals in contaminated sediments by hydroxyapatite addition. *Journal of Environmental Quality*, 30, pp. 460-469. https://doi.org/10.2134/jeq2001.302460x

CHISHOLM-BRAUSE, et al., (2001) Uranium(VI) Sorption Complexes on Montmorillonite as a Function of Solution Chemistry. Journal of *Colloid and Interface Science*, 233, pp. 38-49. https://doi.org/10.1006/jcis.2000.7227

BORS, J. DULTZ, St. and RIEBE, B. (1999) Retention of radionuclides by organophilic bentonite. *Engineering Geology*, 54, pp. 195-206. https://doi.org/10.1016/S0013-7952(99)00074-5

MATIJAŠEVIĆ, S. et al., (2006) Uranium(VI) adsorption on surfactant modified heulandite/clinoptilolite rich tuff. *Journal of the Serbian Chemical Society*, 71 (12) pp. 1323-1331. https://doi.org/10.2298/JSC0612323M

MING, D. and DIXON, J. (1987) Quantitative Determination of Clinoptilolite in Soils by a Cation-Exchange Capacity Method. *Clays and Clay Minerals*, 35, pp. 463-468. https://doi.org/10.1346/CCMN.1987.0350607

RATHORE, D.P.S. (2008) Advances in technologies for the measurement of uranium in diverse matrices. *Talanta*, 77 (1), pp. 9-20. https://doi.org/10.1016/j.talanta.2008.06.019

OZTAS, N.A., KARABAKAN, A. and TOPAL, O. (2008) Removal of Fe(III) ion from aqueous solution by adsorption on raw and treated clinoptilolite samples. *Microporous Mesoporous Materials*, 111 (1–3), pp. 200–205. https://doi.org/10.1016/j.micromeso.2007.07.030

CASTALDI, P., et al., (2008) Sorption processes and XRD analysis of a natural zeolite exchanged with Pb^{2+}, Cd^{2+} and Zn^{2+} cations. *Journal of Hazardous Materials*, 156 (1–3), pp. 428–434. https://doi.org/10.1016/j.jhazmat.2007.12.040

MATIJAŠEVIĆ, S. et al., (2016) Removal of uranium (VI) from aqueous solution by acid modified zeolites. *Zaštita Materijala*, 57 (4), pp. 551–558. https://doi.org/10.5937/ZasMat1604551M

UNDERGROUND MINING ENGINEERING 46 (2025) 123-137 UDK 62
UNIVERSITY OF BELGRADE - FACULTY OF MINING AND GEOLOGY ISSN 03542904

Review paper

TREATMENT OF FLUE GAS AND COAL TO REDUCE AIR POLLUTION-OVERVIEW

Slavica R. Mihajlović[1], Nataša G. Đorđević[1], Srđan D. Matijašević[1], Vladan D. Kašić[1]

Received: March 28, 2025 **Accepted:** May 26, 2025

Abstract: This paper presents the procedures that can be used to reduce air pollution that originates from the burning of fossil fuels. Research has shown that burning coal is the largest source of emissions of greenhouse gases such as carbon dioxide, sulfur oxides, nitrogen oxides and suspended particles. In order to reduce the emission of harmful agents from thermal power plants, several procedures based on various technologies are applied. It is possible to treat the already created flue gases created by burning coal in the classic way, treatment of the coal itself before the start of combustion in the thermal power plant and special procedures for coal treatment. Very effective procedures applied to protect air from pollution in the energy sector are: flue gas desulphurization (FGD), coal purification before the combustion process (coal washing), coal gasification and coal combustion in a fluidized bed. The paper also provides a detailed account of the advantages and disadvantages of the procedures described with an analysis of the contribution of scientific research in defining the technology itself.

Keywords: air protection, flue gas desulfurization, coal washing, coal gasification, coal combustion in a fluidized bed

1 INTRODUCTION

Environmental degradation implies pollution of air, soil and watercourses as three inseparable components. These problems became particularly pronounced in the era of urbanization, industrial and technological development. Air pollution is a type of pollution that is transferred to both land and water. Air is polluted when an excess of aerosols and chemicals are present in the atmosphere compared to air from a pristine environment. Air pollutants are any physical, chemical or biological agents that have the

[1] Institute for Technology of Nuclear and Other Mineral Raw Materials, Franchet d`Esperey 86, 11000 Belgrade, Serbia

E-mails: s.mihajlovic@itnms.ac.rs, ORCID: 0000-0003-0904-3878; n.djordjevic@itnms.ac.rs, ORCID: 0000-0002-2353-6751; s.matijasevic@itnms.ac.rs, 0000-0002-3897-8085; v.kasic@itnms.ac.rs, ORCID: 0000-0002-4430-567X

ability to adversely affect air quality. Sources of air pollution can be classified into two groups according to the way of their origin:

1. Natural (volcanic eruptions, forest fires, wind-blown dust) and 2. Anthropogenic (industrial processes, fossil fuel combustion, waste treatment, construction and agricultural activities) (Lee, Hadibarata and Yuniarto, 2020; Borm, 2002).

Recently, the increase in the concentration of air pollutants has reached alarming proportions. The dominant pollutants are nitrogen dioxide NO_2, sulfur dioxide SO_2, carbon monoxide CO and suspended particles whose diameter is 10 μm and smaller, known as PM10 μm and PM2.5 μm. Sources of gaseous pollutants are the emission of gases from industrial plants, thermal power plants, car exhaust gases, burning of agricultural waste, individual fireplaces in households, etc. (Singh et al., 2022).

High levels of air pollution adversely affect human health by causing various respiratory diseases. Also, they negatively affect natural processes in ecosystems, which is reflected in the flora and fauna. In the immediate vicinity of the source of pollution, pollutant deposition and the formation of barren soil occur. Weakly developed vegetative cover threatens the habitat of a large number of animal species (Zvereva, Toivonen and Kozlov, 2008).

Therefore, it is important to implement protective measures and prevent the direct discharge of polluting substances into the surrounding area. Purification of contaminated flue gases and removal of all substances that may have a harmful effect on the environment is necessary. Research has shown that thermal power plants that have a traditional way of burning coal are by far the biggest source of greenhouse gas emissions such as: carbon dioxide, sulfur oxides, nitrogen oxides and suspended particles. Coal is responsible for 90% of SO_2 emissions, 70% of dust emissions, 67% of nitrous oxide emissions and 70% of CO_2 emissions (Melikoglu, 2018; EIA, 2018).

In order to reduce the emission of harmful agents from thermal power plants, several procedures are applied in various stages of the process. It is possible to treat the already created flue gases created by burning coal in the classic way, treatment of the coal itself before the start of combustion in the thermal power plant and special procedures by which coal is converted into gas or combustion is carried out in a fluidized state.

Experts dealing with this issue have also introduced the term "clean coal technology" to highlight the importance of this topic. The basis of the concept of this technology is the procedures that improve the quality and efficiency of coal, as well as its environmental acceptability in all stages of its life cycle. This solution includes three main categories (Chen and Xu, 2010): 1. Coal enrichment, 2. Coal transformation - supercritical combustion and combustion in an oxygen atmosphere, and 3. Flue gas treatment.

The application of "clean coal technology" is increasingly important given the greater need for energy sources. The application of this technology prevents the emission of

harmful combustion products from thermal power plants: spent particles, oxides of sulfur, nitrogen, mercury. In this way, not only air pollution is prevented, but also contamination of the surrounding soil and the occurrence of acid rain. It also has an effect on the reduction of global warming and climate change (Rybak et al., 2024; Blaschke, 2008).

2 FLUE GAS AND COAL TREATMENTS

In order to prevent air pollution by burning coal, several procedures are applied: flue gas desulfurization (FGD), coal purification before the burning process (coal washing), coal gasification and coal burning in a fluidized bed (Jafarinejad, 2017).

2.1 Flue gas desulphurization (FGD)

FGD is a purification technique that uses alkaline reagents, usually calcium-based, to remove SO_2. The procedures can be dry, semi-dry and wet, depending on the aggregate state of the used reagent. Lime-wet flue gas purification processes using wet limestone technology, the so-called gypsum process, are most widely used. More than 90% of flue gas desulphurization plants in the world operate according to this principle. The reason for this is the high efficiency, 90-95%, the relatively low consumption of sorbent, as well as the possibility of using the resulting waste product, i.e. gypsum (Ghosh, Biswas and Datta, 2024; Mchabe et al., 2021; Zhao and Zou, 2021).

The procedure is based on washing flue gases with an aqueous suspension of limestone or lime in an adsorption reactor, which produces lime sulfite $CaSO_3$. Limestone or slaked lime powder, after preparation in the form of a water suspension, is introduced into the adsorber using pumps. Additional oxygen saturation enables the conversion of $CaSO_3$ into $CaSO_4$, which, after being separated from the solution, goes on to further processing (washing and drying), which finally produces gypsum ($CaSO_4 \cdot 2H_2O$). A special system of circulation pumps, pipelines and nozzle systems guarantees intensive flue gas washing in the adsorption tower. The effectiveness of the process depends to a large extent on the intensity of the flue gas washing.

The FGD lime-wet process additionally removes HCl and HF compounds, as well as ash from the flue gases. This waste is then subjected to chemical treatment to remove heavy metals. As a result of washing, flue gases are cooled down to a temperature of around 50^{o}C, which is why it is necessary to reheat them before they are taken to the chimney. Heating is carried out in special heaters. However, it is possible to introduce the cooled flue gases into the chimney without heating, which reduces investment costs. Furthermore, due to the reduction of the resistance to the flow of flue gases, the operating costs are also reduced due to the reduction of the energy consumption for the fan drive. There is also a flue gas removal system using a "wet chimney" installed on the adsorber. Due to the possibility of introducing all the mentioned variables, it is necessary, when analyzing the operation of the flue gas processing plant, to always take into account the

local operating conditions for the given object, that is, the plant (Sekulic, Jovanovic and Kasic, 2012; Stojiljkovic et al., 2009).

2.2 Coal purification before the combustion process (coal washing)

Coal cleaning is an effective procedure that reduces the concentration of harmful elements present in coal. In the washing plants, using appropriate mining equipment, the coal is first crushed and sifted, whereby fractions of a certain size are obtained. The cleaning process itself is based on mixing coal of a certain fraction with heavy liquids of a certain density. Zinc chloride $ZnCl_2$ solution is used as a heavy liquid and the density with which the procedure starts is 1100-1300 kg/m^3 and ends with a density of 1800-1900 kg/m^3. During immersion, impurities settle (sink), and clean coal remains on the surface (floats), so this analysis is called float-sink analysis or FS-analysis. The resulting coal fractions are measured and their ash content is determined. Ash represents the non-burnable residue, i.e. the inorganic part of coal. It can be considered that the higher the quality of the coal and the higher the heat capacity, the lower the ash content. Coal also contains large amounts of combustible sulfur. By cleaning coal, it is possible to remove this harmful element. Therefore, the sulfur content is determined on each separated coal fraction, except for ash (Knezevic, 2012).

Graphical presentation of coal FS analysis is done according to the method conceived by Henry and Reinhardt. This method of graphical representation provides for the construction of 4 curves: the curve of the boundary layers, the curve of the average ash content in the fractions that float, the curve of the average ash content in the fractions that sink, and the curve of the stratification density. By applying Henry-Reinhardt curves, it is possible to make a balance with two products (clean coal and tailings) and with three (clean coal, intermediate product and tailings), (Cebeci and Ulusoy, 2013). The effectiveness of the procedure depends on the degree of liberation of the mineral containing the element to be removed. With this procedure, in addition to ash and pyrite sulfur, mercury associated with pyrite is also removed (Miller, 2011).

In the preparation of coal, the main goal is to separate the coal, as a useful component, from impurities. This can also be achieved by processes that include coarse and medium purification, as well as fine and ultrafine (in spirals, separators, conventional and column flotation cells). The treatment of coal before its combustion in the thermal power plant affects the reduction of the percentage of ash formation, fly ash, and the concentration of sulfur dioxide in the flue gases. All of this contributes to better air quality in the thermal power plant area. Also, by cleaning, coal becomes of better quality, because it has a higher calorific value (Kostovic et al., 2022).

2.3 Coal gasification

Coal gasification is the conversion of coal into gaseous fuels, i.e. synthetic gas or syngas. The conversion is done by interacting with agents that act as oxidants such as water vapor, air or oxygen. Complete gasification involves the conversion of all the

carbonaceous material contained in the coal into gaseous products. After the procedure is completed, ash remains as the only solid material (Ward, 2013). Gasification is by nature a thermal process of gas production from the natural reaction of coal with oxygen, air or steam. Coal gasification has an advantage over other energy production technologies because it belongs to clean technologies. With this method, the classic process of burning coal is eliminated. The performance of the procedure depends on the type of coal and the construction of the gasifier itself (Muhammed et al., 2023; Midilli et al., 2021).

By applying an integrated system of a combined gasification cycle, steam and hot air under pressure or oxygen are mixed with coal and during the reaction a gaseous product, syngas, is formed. The resulting mixture of carbon monoxide, hydrogen, carbon dioxide and water vapor is then cleaned, burned in a gas turbine to produce electricity. Cleaning the gas mixture involves removing mercury, sulphur, particulate matter and other trace contaminants so that only CO, CO_2 and hydrogen remain. The method allows reaching a fuel efficiency of 50%. With this relatively new technology, poorer quality coals can be treated, which otherwise could not be used for direct combustion in thermal power plants (Visionias Inspiring Innovation, 2025). The process of coal gasification to obtain pure hydrogen takes place as follows (MWCOG, 2025):

Step 1: Mixing coal powder with oxidants at a high temperature (up to 1800 °C), during which gasification and gas formation occur, which are a source of energy. The resulting gas consists of H_2, CO and traces of CO_2, CH_4 and water vapor.

Step 2: The resulting gas is cooled and purified to remove mercury, sulfur, trace contaminants and particles. CO, CO_2 and hydrogen remain in the purified gas. The purification of the gasification product is much easier and simpler than the purification of flue gases from thermal power plants that work in the traditional way of burning coal.

Step 3: Transport of the gas to the reactor where the CO conversion is carried out. At the end of the process, the gas consists mainly of hydrogen and CO_2.

Step 4: Further purification of the gas and separation into separate hydrogen and CO_2 streams. After this stage, the hydrogen is ready for use, and the CO_2 is sent for sequestration. Sequestration is the process of extracting carbon from CO_2 and depositing it in a previously prepared place. In this way, the emission of CO_2 into the atmosphere is reduced (Mondal et al., 2024).

Step 5: The resulting hydrogen is ready for further use such as: combustion in a gas turbine to produce electricity, conversion to electricity in a fuel cell, use as a fuel in an internal combustion engine and use as a chemical.

2.4 Combustion of coal in a fluidized bed

Coal combustion in a fluidized bed is a process that takes place in a special combustion reactor. The coal powder is suspended in the air stream which is injected into the reactor in pressurized jets. The fuel retention time in these specialized boilers is long enough to ensure complete combustion. Also, fuel, i.e. coal, can be mixed with limestone, which contributes to a more efficient removal of sulfur (Visionias Inspiring Innovation, 2025).

The conditions in the reactors are such that the material is constantly in a fluidized state and behaves like a boiling liquid. This state is maintained by means of an emulsion of gas bubbles that continuously mix the solid phase, whereby good heat transfer between the gas and solid phases is enabled. In the upper part of the reactor there is a gas phase, and in the lower part there is a material with a thickness of 0.2-0.5 mm. The main stages of thermochemical conversion take place within or above the fluidized bed (Liu et al., 2014; Iannello, Morrin and Materazzi, 2020; Nunes, 2020).

Combustion of coal particles in a fluidized bed is a complex procedure and takes place in three phases: drying, loss of volatile substances and combustion. The entry of coal particles into the combustion reactor due to the high temperature leads to rapid loss of moisture (drying) and volatile substances. It can be said that the heat in the reactor is spent on heating and drying the coal particles and the endothermic reaction of evaporation. The reaction of burning carbon is exothermic, so they contribute to the increase of temperature in the reactor. The difference in the temperature of a burning coal particle and the surrounding medium depends on the characteristics of the coal and carbon and on the oxygen concentration in the surrounding gas. According to the literature data, the temperature of the air is up to 400°C, and the combustion products up to 900°C (Komatina, Manovic and Dakic, 2006; Oka, 1994).

The process of burning coal in a fluidized bed represents a great advance in solving the pollution problems that arise from burning coal in the classic way in thermal power plants. The application of this technology and the construction of modern reactors have made a great contribution in the field of energy and coal combustion.

3 ANALYSIS OF ADVANTAGES AND DISADVANTAGES OF FGD AND COAL TREATMENT TECHNOLOGY

3.1 FGD technologies

Experts who research coal as an energy source believe that progress in this area is evident. This was contributed by the application of coal cleaning and gasification procedures, as well as combustion in a fluidized bed. Progress was contributed by defining the mechanism of desulfurization and mass transfer, defining the kinetics of oxidation, finding the possibility of reusing desulfurization products, as well as the possibility of optimization and simulation of procedures. Scientific research, setting the

foundation and defining the mechanism of dry, semi-dry and wet desulfurization processes have made a great contribution to the understanding of this field. A critical review of the concept of these technologies is a prerequisite for new knowledge and improvements in this area, which eliminates their shortcomings (Pandey et al., 2005).

3.1.1 Wet procedure

The wet FGD process is very effective in removing SO_2 from flue gases, but the expert public points out that it also has its disadvantages. The main disadvantage is the high initial investment costs for the equipment and the high operating costs. The wastewater from the desalination plant is highly corrosive and contains pollutants derived from coal and limestone. They contain high concentrations of total dissolved solids, suspended solids, chloride, fluoride, nitrate and nitrite. Also, the wet FGD system is expensive due to the large amount of energy required to operate the pumps. This is especially evident when sea water is used in the plant. Power plants near the sea and the ocean, with a capacity of up to 1000MW, use pumps to supply the necessary amounts of water, which significantly increases the cost of the desulfurization process itself. Regardless of its drawbacks related to large investments, wet desulphurization technology is the most widespread, because it has the highest efficiency. In recent years, the reactors used in this procedure have been significantly improved and optimized, so the costs are also lower. This is also supported by the possibility of using a by-product of this procedure - plaster, which contributes to reducing waste and disposal costs (Li et al., 2022).

3.1.2 Dry procedure

The dry process is an alternative to the wet process for FGD and is based on injecting powdered reagents directly into the furnace. The procedure requires much less space and does not require the disposal of by-products, but it is less efficient than the wet procedure and can be used in power plants with a capacity of up to 1000 MW, unlike the wet procedure, which is used in power plants with a much larger capacity. In the dry SO2 adsorption process, besides powdered limestone, metal oxides and solid compounds such as copper oxide, activated carbon, activated manganese oxide, alumina, red mud etc. are used. However, it was found that they are not efficient adsorbents, because SO2 is only adsorbed on the surface. Great progress in the field of dry adsorption was achieved by modifying adsorbents and defining the mass transfer model of two-phase flow between gas and solid in reactors. The dry desulfurization process can be divided into three different technologies: 1. Desulfurization by injecting calcium; 2. Circulating Fluidized Bed Desulfurization and 3. Activated Coke Desulfurization Technology (Li et al., 2022).

Desulphurization technology by injecting calcium into the furnace is characterized by low investment, low operating costs and the absence of waste water. However, the disadvantage is low efficiency, 20-50%, while limestone utilization is only 10% (He, 1989). In order to increase the use of limestone, and thus the efficiency of the process, a limestone injection procedure with additional activation of unreacted calcium was

developed in Finland. Namely, a device with nozzles for wetting limestone is installed in the activation reactor, and in this way the speed of desulphurization increases (Anthony, et al., 2005).

Circulating fluidized bed desulfurization technology was first installed in Munich in 1984. and proved to be very effective (Graf, 1986). It is based on the injection of slaked lime powder into the fluidized bed where it reacts with SO2 from the flue gas that is fed to the bottom of the bed. After desulfurization, the compressed flue gas is discharged from the top of the fluidized bed.

Activated coke desulphurization technology appeared in 1960. It is based on the adsorption of SO2 from flue gases with the help of activated coke particles produced from coal, whereby after adsorbing SO2, the activated coke can desorb it at high temperatures, thus creating the conditions for a repeated desulphurization process (Zhang, Su and Zhou, 2000; Skopec, Hrdlička and Vodička, 2021).

The subject of study by researchers in this field was the way to activate carbon from coal to form a pore structure to obtain activated carbon. Some have used steam for activation (Rubio et al., 1998) and have concluded that the resulting activated carbon has the same desulfurization capacity as commercial activated carbon, thereby reducing its economic cost. The combination of treatment in furnace atmosphere and multi-stage hydrothermal autoclaves gave such a structure of activated semi-coke that it could be used for sulfur and nitrate removal together which was a very significant data (Zhang et al., 2017).

3.1.3 Semi-dry process

Semi-dry desulfurization technologies are also advancing, which is reflected in the constant optimization of process conditions and the increase of desulfurization efficiency. The development of cheap and highly active adsorbers that can be recycled (e.g. semi-dry ash) reduces the costs of performing the procedure itself. Semi-dry desulfurization technology does not require energy for reheating or wastewater treatment, so operating costs are lower compared to the wet process. Also, it does not require a large space for the installation of the necessary equipment as with the wet process. However, the efficiency of the procedure is at a lower level compared to the wet procedure (Wang, 2018). Within this technology, the following most important methods are used: spray drying, pouring of powder particles and circulating fluidized bed.

The spray drying method was developed in Denmark in the "Niro" company in the seventies of the last century. The concept is based on spraying the lime suspension into the absorption tower in the form of fine droplets with the help of a rapidly rotating sprayer. Droplets of $Ca(OH)_2$ quickly adsorb SO_2, dry and a solid desulphurization product remains. The efficiency of the procedure depends on the superposition of the absorption process with the drying process, while the SO_2 content in the flue gas has no effect on the desulphurization rate, which is a major advantage of the method (Hill and Zank, 2000; Karlsson and Klingspor, 1987). In order to improve the adsorbent utilization

rate and the desulphurization rate, adsorbers have been developed as mixtures of two components such as fly ash/quicklime and fly ash/slaked lime mixtures (Sanders, Keener and Wang, 1995).

The method with poured powder particles contributed to the achievement of desulphurization efficiency close to that achieved by the wet method, which is considered a major advance in the field of semi-dry technologies. Also, it has brought significant economic benefits. As the main place (reactor) in this method, where the SO_2 extraction reactions take place, is actually a cast bed of powder particles. A suspension of slaked lime or some other alkaline powder is continuously sprayed into a bed of coarse particles (usually several hundreds of microns), most often quartz sand, to absorb SO_2. The reactions of desulfurization and suspension drying are carried out simultaneously in the bed of powder particles (Guo, Noriaki and Kato, 1996).

The method of desulphurization with a circulating fluidized bed was created at the suggestion of the University of Cincinnati. With this technology, the vertical fluidized bed is the main body of the reactor, where high-temperature flue gas is drawn into the fluidized bed at high speed, after which the absorption reaction takes place. Circulating fluidized bed can be used both for dry and semi-dry desulphurization. The absorbent used in this method (limestone, fly ash) is recyclable (Jiang, Keener and Khang, 1995).

3.2 Treatment of coal

3.2.1 Coal gasification

Coal gasification is recognized as the basis of clean coal utilization technology. The significant advantage of this technology is reflected in the way of electricity production, production of hydrogen-rich synthetic gas and reduced SO_2 emissions. The obtained synthetic gas is used in combined cycle technology for the production of electricity with a theoretical efficiency of energy production exceeding 45%, which contributes to the comprehensive efficiency of coal use. Also, the concentrations of SO_2 and H_2 can be increased in the produced gas through synthesis gas steam reactions, which reduces the consumption of electricity for SO_2 removal and the production of high-quality hydrogen (Kim et al., 2013).

A major advance in this area has been the introduction of new gasification technologies including supercritical water gasification, plasma gasification, chemical loop gasification, separation gasification, and subsurface gasification. Conventional gasification procedures have been replaced in recent years by new technologies such as fixed bed technology, fluidized bed technology and flow technology, which eliminated all the disadvantages of old technologies (Matamba, Iglauer and Keshavarz, 2022; Fan and Jin, 2022). However, it should be emphasized that the expert public agrees that even today there is room for progress in conventional gasification in the direction of designing large-sized reactors, better control of gaseous pollutants, use of solid residues, etc. On the other hand, with the help of sophisticated techniques and knowledge, there are

conditions for the development of catalytic and microwave gasification, as a process of the future, but currently there are no conditions for their commercial application due to technical shortcomings (Dai et al., 2023).

3.2.2 Combustion of coal in a fluidized bed

The fluidized bed technology has its advantages, as it is very flexible in terms of the properties of the materials being processed, such as the heat value of the raw material, moisture content, particle size and density, sulfur content, etc. Also, it has superior performance in terms of heat and mass transfer. Namely, the advantages compared to other technologies are homogeneity of temperature, increased speed of heat transfer, good mixing of solid particles and the possibility of carrying out further processes such as drying of particles. Also, this technology gives two options in terms of configuration, namely bubbles and circulating fluidized beds (Miccio et al., 2021).

One of the main disadvantages of this technology is the occurrence of agglomeration phenomena due to the sintering of the bed caused by the alkali present in the fuel, especially waste and residues, which leads to a breakdown in the plant and urgent emergency interventions (Hupa, 2012). In order to alleviate the agglomeration phenomenon, cheap alternative materials, such as SiO_2, are used in practice to inhibit this phenomenon. The problem with processes in a fluidized bed is the occurrence of the fragmentation phenomenon, which leads to a decrease in the efficiency of the process. This is especially pronounced in the case of less reactive fuels (Chirone, Massimilla and Salatino, 1991).

4 CONCLUSION

Solving the problem of air pollution in the energy sector has become imperative in countries that use fossil fuels. Emphasis is on clean coal processing technologies (coal gasification and coal combustion in a fluidized bed), which generate significantly less pollutants than conventional coal combustion in thermal power plants. In order to develop new technologies, a connection between science and practice is necessary. Results obtained in scientific research are very often difficult to apply in practice due to large economic investments and technical shortcomings. The development of catalytic and microwave gasification, as examples of this, as processes of the future, have not yet found their full application. Research in this field must progress, despite all the difficulties of practical application. Development of flue gas treatment technologies was contributed by the results of scientific research that defined adsorption mechanisms during desulfurization and mass transfer, defined oxidation kinetics, characteristics of the adsorbents themselves, found the possibility of reusing desulphurization products, as well as the possibility of optimization and simulation of procedures. Critical analysis of the concepts of these technologies is a prerequisite for new knowledge and improvements in this field, which also eliminates their shortcomings. The structure and chemical forms of coal itself are the subject of further scientific research. The researchers

found that there are mechanisms of element binding that deserve attention such as the question under which conditions toxic elements (As, Hg) replace the major sulfide ions in coal. Also, certain rare mineral phases that are not common have been identified in the coal including native forms of W, Au and Ag, various Au and Pt phases. All of the above can affect the efficiency of the procedures presented in this paper. And finally, the following facts that are generally important for both science and practice should be highlighted: 1. Due to the increasing global pressure on the environment and the need for energy, constant research is necessary in the future with the aim of developing innovative technologies for the clean conversion of coal into energy and the reduction of greenhouse gas emissions and 2. Focusing on solving practical engineering problems in terms of designing economically viable plants is essential.

ACKNOWLEDGEMENT

The authors would like to thank the Ministry of Science, Technological Development and Innovation of the Republic of Serbia for supporting the research (contract 451-03-136/2025-03/200023).

REFERENCES

ANTHONY, E.J. et al. (2005) LIFAC ash-strategies for management. *Waste Management*, 25 (3), pp. 265-279. https://doi.org/10.1016/j.wasman.2004.11.005

BLASCHKE, W. (2008) Clean Coal Technologies-The first step is coal preparation. *Polityka Energetyczna-Energy Policy Journal*, 11 (2), pp.7-13. https://epj.min-pan.krakow.pl/Issue-2-2008,6353

BORM, P.J.A. (2002) Particle toxicology: from coal mining to nanotechnology. *Inhalation Toxicology*, 14 (3), pp. 311–324. DOI: 10.1080/08958370252809086

CEBECI, Y. and ULUSOY, U. (2013) An optimization study of yield for a coal washing plant from Zonguldak region. *Fuel Processing Technology*, 115, pp. 110-114. https://doi.org/10.1016/j.fuproc.2013.04.014

CHEN, W. and XU, R. (2010) Clean coal technology development in China. *Energy Policy*, 38 (5), pp. 2123–2130. DOI: 10.1016/j.enpol.2009.06.003

CHIRONE, R. MASSIMILLA, L. and SALATINO, P. (1991) Comminution of carbons in fluidized bed combustion. *Progress in Energy and Combustion Science*, 17 (4), pp. 297-326. https://doi.org/10.1016/0360-1285(91)90006-9

DAI, F. et al. (2023) Recent Progress on Hydrogen-Rich Syngas Production from Coal Gasification. *Processes*, 11 (6), 1765. https://doi.org/10.3390/pr11061765

EIA (2018) *Changes in Coal Sector Led to Less SO_2 and NOx Emissions from Electric Power Industry.* [Online] EIA. Available from: https://www.eia.gov/todayinenergy/detail.php?id=37752 [Accessed 20/03/25].

FAN, C. and JIN, H. (2022) Numerical simulation of gasification of a shrinking char particle in supercritical water. *Fuel*, 318, 123692. https://doi.org/10.1016/j.fuel.2022.123692

GHOSH, D., BISWAS, D. and DATTA, A. (2024) Absorption height in spray tower for wet-limestone process in flue gas desulphurization. *Materials today: Proceedings*, In press. https://doi.org/10.1016/j.matpr.2024.02.001

GRAF, R. (1986) First operating experience with a dry flue gas desulfurization (FGD) process using a circulating fluid bed (FGD-CFB). *Circulating Fluidized Bed Technology*, Proceedings of the First International Conference on Circulating Fluidized Beds, Halifax, Nova Scotia, Canada, November 18–20, 1985. pp. 317-327. https://doi.org/10.1016/B978-0-08-031869-1.50038-7

GUO, Q.M., NORIAKI, I. and KATO, K. (1996) Process Development of Effective Semi-Dry Flue Gas Desulfurization by Powder-Particle Spouted Bed. *Kagaku Kogaku Ronbunshu,* 22 (6), pp. 1400-1407. https://doi.org/10.1252/kakoronbunshu.22.1400

HE, H.G. (1989) In-furnace Sorbent Injection-based Desulfurization Technolog. *Therm Power Generat 5,* 7-9+6. CNKI:SUN:RLFD.0.1989-05-001.

HILL, F.F. and ZANK, J. (2000) Flue gas desulphurization by spray dry absorption. *Chemical Engineering and Processing: Process Intensification*, 39 (1), pp. 45-52. https://doi.org/10.1016/S0255-2701(99)00077-X

HUPA, M. (2012) Ash-Related Issues in Fluidized-Bed Combustion of Biomasses: Recent Research Highlights. *Energy & Fuels*, 26 (1), pp. 4-14. https://doi.org/10.1021/ef201169k

IANNELLO, S., MORRIN, S. and MATERAZZI, M. (2020) Fluidised Bed Reactors for the Thermochemical Conversion of Biomass and Waste. KONA Powder and Particle Journal, 37, pp. 114–131. https://doi.org/10.14356/kona.2020016

JAFARINEJAD, S.H. (2017) *Control and Treatment of Air Emissions*. Chapter 5, Petroleum Waste Treatment and Pollution Control, pp. 149-183. https://doi.org/10.1016/B978-0-12-809243-9.00005-5

JIANG, M.X., KEENER, T.C. and KHANG, S.J. (1995) The use of a circulating fluidized bed absorber for the control of sulfur dioxide emissions by calcium oxide sorbent via in situ hydration. *Powder Technology*, 85 (2), pp. 115-126. https://doi.org/10.1016/S0301-9322(97)88546-1

KARLSSON, H.T. and KLINGSPOR, J. (1987) Tentative modelling of spray-dry scrubbing of SO_2. *Chemical Engineering Technology*, 10 (1), pp. 104-112. https://doi.org/10.1002/ceat.270100114

KIM, J. et al. (2013) Hydrogen production via steam gasification of ash free coals. *International Journal of Hydrogen Energy*, 38 (14), pp. 6014–6020. https://doi.org/10.1016/j.ijhydene.2012.12.058

KNEŽEVIĆ, D. (2012) *Priprema mineralnih sirovina*. Beograd: Rudarsko-geološki fakultet Beograd, Univerzitet u Beogradu.

KOMATINA, M., MANOVIC, V. and DAKIC, D. (2006) An Experimental Study of Temperature of Burning Coal Particle in Fluidized Bed. *Energy & Fuels*, 20 (1), pp. 114-119. https://doi.org/10.1021/ef050222o

KOSTOVIĆ, M. et al. (2022) Coal cleaning before combustion-practice and experience in Serbia. *Underground mining engineering*, 41, pp. 23-30. DOI: 10.5937/podrad2241023K

LEE, B.X.Y., HADIBARATA, T. and YUNIARTO, A. (2020) Phytoremediation Mechanisms in Air Pollution Control: a Review. *Water, Air, & Soil Pollution*, 231, 437. https://doi.org/10.1007/s11270-020-04813-6

LIU, Y. et al. (2014) Novel fluidized bed dryer for biomass drying. *Fuel Processing Technology*, 122, pp. 170–175. DOI:10.1016/j.fuproc.2014.01.036

LI, X. et al. (2022) Summary of research progress on industrial flue gas desulfurization technology. *Separation and Purification Technology*, 281, 119849. https://doi.org/10.1016/j.seppur.2021.119849

MATAMBA, T., IGLAUER, S. and KESHAVARZ, A. (2022) A progress insight of the formation of hydrogen rich syngas from coal gasification. *Journal of the Energy Institute*, 105, pp. 81-102. https://doi.org/10.1016/j.joei.2022.08.001

MCHABE, D. et al. (2021) Development of an integrated model for absorption of sulphur dioxide in limestone slurry. *Chemical Engineering Science*, 229, 116050. https://doi.org/10.1016/j.ces.2020.116050

MELIKOGLU, M. (2018) Clean coal technologies: A global to local review for Turkey. *Energy Strategy Reviews*, 22, pp. 313–319. https://doi.org/10.1016/j.esr.2018.10.011

MICCIO, F. et al. (2021) Fluidized Bed Combustion and Gasification of Fossil and Renewable Slurry Fuels. *Energies*, 14 (22), 7766. https://doi.org/10.3390/en14227766

MIDILLI, A. et al. (2021) A comprehensive review on hydrogen production from coal gasification: challenges and opportunities. *International Journal of Hydrogen Energy*, 46 (50), pp. 25385-25412. https://doi.org/10.1016/j.ijhydene.2021.05.088

MILLER, B.G. (2011) *Clean Coal Engineering Technology*. Butterworth: Heinemann. https://doi.org/10.1016/C2009-0-20236-4

MONDAL, A. et al. (2024) Impact and potential of carbon sequestration and utilization: fundamentals and recent developments. *International Journal of Coal Preparation and Utilization*, 44, 12, pp. 2018-2043. https://doi.org/10.1080/19392699.2024.2305940

MUHAMMED, N.S. et al. (2023) Hydrogen production, transportation, utilization, and storage: Recent advances towards sustainable energy. *Journal of Energy Storage*, 73, Part D, 109207. https://doi.org/10.1016/j.est.2023.109207

MWCOG (2025) *Hydrogen production from coal*. [Online] MWCOG. Available from: https://www.mwcog.org/file.aspx?&A=6lJMMDOHmOUL2TT9fb7pcrAAeY5PdpMxMeZbS9eJzyo%3D [Accessed 18/03/25]

NUNES, L.J.R. (2020) Potential of Coal-Water Slurries as an Alternative Fuel Source during the Transition Period for the Decarbonization of Energy Production: A Review. *Applied Sciences*, 10 (7), 2470. https://doi.org/10.3390/app10072470

OKA, S.N. (1994) *Sagorevanje u fluidizovanom sloju-procesi i priprema*. Beograd: Jugoslovensko društvo termičara.

PANDEY, R.A. et al. (2005) Flue gas desulfurization: physicochemical and biotechnological approaches. *Critical Reviews in Environmental Science and Technology*, 356 (6), pp. 571-622. https://doi.org/10.1080/10643380500326374

RUBIO,B. et al (1998) Influence of low-rank coal char properties on their SO2 removal capacity from flue gases. 2. Activated chars, *Carbon*, 36 (3), pp. 263-268. https://doi.org/10.1016/S0008-6223(97)00190-5

RYBAK, A. et al. (2024) Analysis of the Impact of Clean Coal Technologies on the Share of Coal in Poland's Energy Mix. *Energies*, 17 (6), 1394. https://doi.org/10.3390/en17061394

SANDERS, J.F., KEENER, T.C. and WANG, J. (1995) Heated Fly Ash/Hydrated Lime Slurries for SO2 Removal in Spray Dryer Absorbers. *Indistrial and Engineering Chemistry Research*, 34 (1), pp. 302-307. https://doi.org/10.1021/ie00040a032

SEKULIĆ, Ž., JOVANOVIĆ, V. and KAŠIĆ, V. (2012) Litotamnijski krečnjak ležišta "Dobrilovići" u odsumporavanju dimnih gasova. *Rudarski radovi*, 3, str. 41-44. doi: 10.5937/rudrad1203041S

SINGH, A.A. et al. (2022) Air Pollution: Sources and its Effects on Humans and Plants. *International Journal of Plant and Environment*, 8 (1), pp. 10-24. https://doi.org/10.18811/ijpen.v8i01.02

SKOPEC, P., HRDLIČKA, J. and VODIČKA, M. (2021) Dry additive desulfurization in oxyfuel bubbling fluidized bed combustor. *Fuel*, 283, 118945. https://doi.org/10.1016/j.fuel.2020.118945

STOJILJKOVIĆ, D. et al. (2009) Izbor optimalnog tehničkog rešenja postrojenja za odsumporavanje dimnih gasova na TE „Kostolac B“. *Termotehnika*, 35 (3-4), str. 231-249. https://scindeks.ceon.rs/issue.aspx?issue=8651

ZHANG, K. et al (2017) Multi-stage semi-coke activation for the removal of SO_2 and NO, *Fuel*, 210, pp. 738-747. https://doi.org/10.1016/j.fuel.2017.08.107

ZHANG, X.J., SU, Y.B. and ZHOU, P. (2000) Studies on Sulfur Dioxide Adsorption on the Improved Active Coke. *Environmental Protection Science*, 05, pp. 4-6. 10.16803/j.cnki.issn.1004-6216.2000.05.002

ZHAO, M. and ZOU CH. (2021) An investigation into the influence of dissolution rate on flue gas desulfurization by limestone slurry. *Separation and Purification Technology*, 276, 119356. https://doi.org/10.1016/j.seppur.2021.119356

ZVEREVA, E.L., TOIVONEN, E. and KOZLOV, M.V. (2008) Changes in species richness of vascular plants under the impact of air pollution: a global perspective. *Global Ecology and Biogeography*, 17 (3), 305-319. DOI: 10.1111/j.1466-8238.2007.00366.x

VISIONIAS INSPIRING INNOVATION (2025) *Clean coal technologies*. [Online] VISIONIAS. Available from: https://d19k0hz679a7ts.cloudfront.net/value_added_material/Clean-Coal-Technologies.pdf [Accessed 18/03/25].

WANG, X.M. (2018) Technology about dry desulfurization and semi-dry desulfurization. *Electric Power Environ Protect*, 34(01), pp. 45-48. CNKI:SUN:DLHB.0.2018-01-010.

WARD, C.R. (2013) *Coal Gasification*, Chapter Coal Gelogy, Reference Module in Earth Systems and Environmental Sciences. Elsevier. https://doi.org/10.1016/B978-0-12-409548-9.05437-3

UNDERGROUND MINING ENGINEERING 46 (2025) 139-152 UDK 62
UNIVERSITY OF BELGRADE - FACULTY OF MINING AND GEOLOGY EISSN 2560-3337

Original scientific paper

METHODOLOGY FOR DIMENSIONING THE HOISTING SHAFT USING MATHEMATICAL AND GRAPHICAL METHODS

Ognjen Popović[1], Saša Jovanović[2], Miloš Čolović[2], Luka Crnogorac[3], Rade Tokalić[3]

Received: May 28, 2025 **Accepted:** June 15, 2025

Abstract: The opening of deep ore bodies is most rapidly accomplished using vertical shafts. Shaft construction is the most economically demanding process, so despite providing the fastest access to deep ore bodies, the high capital costs involved in construction mean that determining the cross-sectional dimensions of the shaft is a complex and very important step in the design of the shaft and the entire underground mine. An inadequate cross-sectional area can have negative impacts: a small area limits the mine's capacity, while a large area increases construction costs and affects shaft stability. In modern mining practice, shafts are mostly constructed with a circular cross-section, whose area depends on a single parameter - shaft diameter. The choice of area, or more specifically the minimum shaft diameter, is generally determined empirically using mathematical or graphical methods. If there are indications that production capacity might increase or that greater volumes of air will be required, adjustments are made, and the shaft diameter is increased. This paper will present an extended mathematical model and calculations to accurately determine the dimensions of skips for ore hoisting, followed by a graphical method for determining the shaft diameter based on the mathematical calculation.

Keywords: underground exploitation, dimensioning, hoisting shaft, ore hoisting

1 INTRODUCTION

Shafts are vertical mining structures characterized by a relatively small cross-section compared to their length (depth). These structures may have a direct connection to the surface or not (blind shaft). The high cost of construction also necessitates the multifunctionality of underground spaces. In addition to their primary purpose—by which shafts are named (hoisting shaft, ventilation shaft, service shaft, drainage shaft, backfill shaft)—they are also used for air circulation, employee movement, transport,

[1] Golden Summit Engineering – ZiJin Mining, Belgrade, Serbia
[2] University of Priština, Kosovska Mitrovica, Serbia
[3] University of Belgrade - Faculty of Mining and Geology, Đušina 7, Belgrade, Serbia

E-mails: ognjen.popovic@zijinmining.com, ORCID: 0000-0001-9005-0092; sasa.m.jovanovic@pr.ac.rs, ORCID: 0009-0006-9728-0695; milos.colovic@pr.ac.rs, ORCID: 0000-0003-1621-7936; luka.crnogorac@rgf.bg.ac.rs, ORCID: 0000-0002-9897-270X; rade.tokalic@rgf.bg.ac.rs, ORCID: 0000-0001-9360-2892

maintenance, etc. Depending on their importance, shafts can be classified as main or auxiliary, central, or of lesser significance based on their location and purpose. (Antunović Kobliška, 1973; Hartman Howard, 1992; Torbica & Lapčević, 2020).

As the method of opening that provides the fastest access to deep ore bodies, the vertical shaft represents one of the most important elements of underground mine infrastructure, as it enables direct access to mineral deposits at great depths.

The shaft used for mine development is initially assigned to the primary purpose of ore hoisting and becomes a hoisting shaft. The hoisting shaft can be classified according to the type of hoisting vessel used (Musić, 2014):

- Skip shaft – This type may have a single skip with a counterweight or two/four coupled skips. These shafts are constructed in mines with high production rates, and therefore, one or more additional auxiliary shafts must be built alongside for transporting personnel, materials, etc.

- Skip-cage shaft – Constructed in mines with low to medium production. In addition to ore transportation, this shaft also takes on the role of an auxiliary shaft, serving for servicing the mine. This type of shaft comes in several combinations, such as two skips and a cage with a counterweight, two skips and two cages, etc.

- Cage shaft – Used in mines with low production. Ore is transported in mine carts, which are brought to the surface using cages. The shaft may have two coupled cages or one cage with a counterweight. Nowadays, this method of hoisting is rarely used, as very few mines still rely on shaft hoisting in combination with rail transport.

With skips and cages using counterweights, ore can be hoisted from multiple levels, whereas with coupled conveyances, ore can only be hoisted from a single level.

As previously mentioned, selecting the optimal dimensions of the shaft's cross-section is crucial, since these dimensions determine the scope of required work, capacity limitations, and the type of equipment that will be used throughout the entire lifespan of the mine. This means that the planned dimensions must meet operational requirements over decades of exploitation, so long-term production planning must be taken seriously and carried out for the entire life of mine to avoid unnecessary expenses.

2 DEFINING DIMENSIONS OF VERTICAL SHAFTS

When designing mining openings, the most important factor is the selection of the shape and size of the cross-section.

The shape of the shaft's cross-section is determined based on the physical and mechanical properties of the rock, the shaft's intended purpose, and its operational lifespan. In addition to these factors, the choice of cross-sectional shape is also influenced by construction costs, construction speed, and maintenance costs (Musić, 2014).

The type of rock and the expected lifespan of the shaft determine the type of support structure, while the support material affects the choice of cross-sectional shape.

The most common shaft cross-section shapes are circular and rectangular, with elliptical and combined shapes used less frequently (Jovanović, 1982).

The size of the shaft's cross-section depends on its purpose. For a hoisting shaft with a given capacity, the decisive factors are the dimensions of the hoisting vessels, their number, and arrangement (Jovanović, 1982).

In addition, consideration must be given to the auxiliary equipment installed in the shaft, as well as the requirements for a specific volume and velocity of air passing through the shaft.

In this paper, a calculation of the skip dimensions will be carried out, and based on that, the sizing of the shaft's cross-sectional area will be performed.

2.1 Calculation of skip dimensions

The size, or dimensions, of the skip are determined by the required payload per trip, which is influenced by the planned mine capacity. Achieving the required capacity and the shaft depth are the starting parameters for this calculation. Detailed calculations can be found in literature (Pavlović, 1963; Grujić, 1999).

Necessary hourly capacity (Q_h) on hoisting operations can be calculated as follows:

$$Q_h = \frac{k \cdot Q_{year}}{d \cdot h_d} \tag{1}$$

Where:

Q_{year} – yearly capacity (t per year),
k – coefficient of uneven production (1.1 – 1.3),
d – number of working days in a year,
h_d – effective working hours in a day.

To perform the calculation, it is necessary to know the number of effective working hours during one shift. This time is obtained by subtracting the time needed for transporting personnel and shaft inspection from the total duration of the shift (8 or 12 hours).

The time required for transporting personnel is calculated based on:

$$t_{per} = \frac{h}{v_n} \cdot \frac{N}{n} + \frac{N}{n} \cdot t_m \tag{2}$$

Where:

h – shaft depth (m),
N – number of workers in one shift,
n – number of workers in a skip,
t_m - the maneuvering time when workers enter the skip (approximately 3 seconds per worker),
v_n - the speed of the vessel during the transportation of workers (m/s).

The maximum allowed speed of travel (m/s) is calculated using the following formula:

$$v_{max} = k_i \cdot \sqrt{\frac{2 \cdot p \cdot q}{p+q} \cdot h}, \; m/s \tag{3}$$

Where:

k_i – speed utilization coefficient,
p - hoisting vessel acceleration (m/s^2),
q - hoisting vessel deceleration (m/s^2),
h – shaft depth (m).

According to (Službeni list SFRJ, 1992):

- The maximum allowed value of the speed utilization coefficient is 0.6,
- The maximum allowed acceleration and deceleration is 1 m/s^2,
- The maximum allowed speed for transporting people is 14 m/s, and the maximum allowed speed for transporting material is 20 m/s.

These parameters may vary in different countries legislatively.

Generally, when calculating the maximum speed, the values are adopted by considering the following relationships:

$$p \approx q \geq 0{,}6, \frac{m}{s^2} \tag{4}$$

$$k_i \cdot \sqrt{p} \geq 0{,}5 \tag{5}$$

It is recommended (or it can be adopted) that the travel speed be 20% lower than the maximum travel speed, i.e., $v_n = 0.8 \cdot v_{max}$.

The shaft revision must be carried out before the start of each shift. The duration of the shaft revision can be calculated using the following formula:

$$t_r = 2 \cdot (\frac{h}{0,5} + 800), \text{ s} \tag{6}$$

The number of trips per hour is calculated using the formula:

$$n_h = \frac{3600}{T} \tag{7}$$

Where T represents the total duration of one trip (s) and is calculated as the sum of the travel time (t) and the maneuvering time (t_m):

$$T = t + t_m, \text{ s} \tag{8}$$

The travel time is determined using the following formula:

$$t = \frac{h}{v} + 25, \text{ s} \tag{9}$$

The maneuvering time for ore hoisting using skips is approximately 10 seconds.

The payload of one trip is calculated for two cases:

- In the case of using two coupled hoisting vessels:

$$Q = \frac{Q_h}{n_h}, \text{ t} \tag{10}$$

- In the case of using hoisting vessels with a counterweight:

$$Q = 2\frac{Q_h}{n_h}, \text{ t} \tag{11}$$

The required volume of the skip is calculated:

$$V_S = \frac{Q}{\gamma}, m^3 \tag{12}$$

Where:

γ - bulk density of crushed ore (t/m³).

The dimensions of the shaft were adopted, from literature (Musić, 2014; Torbica, 2020), based on the volume of the skip (shown in Table 1).

Based on two conditions, or two equations, the exact dimensions of the skip can be calculated.

The first condition is the volume of the skip, which is equal to:

$$V_s = P_p \cdot h_s,\ m^3 \tag{13}$$

Where:

P_p - the cross-sectional area of the skip, m²,

h_s - the height of the skip, m.

Skips can have a rectangular (14) or square cross-section (15), so the areas are:

$$P_p = a \cdot b,\ m^2 \tag{14}$$

$$P_p = a^2,\ m^2 \tag{15}$$

For a rectangular (a, b) or square cross-section of the skip (a, a), the diagonal can be determined using the Pythagorean theorem.

$$d^2 = a^2 + a^2 = 2a^2 \tag{16}$$

$$d = a\sqrt{2},\ m \tag{17}$$

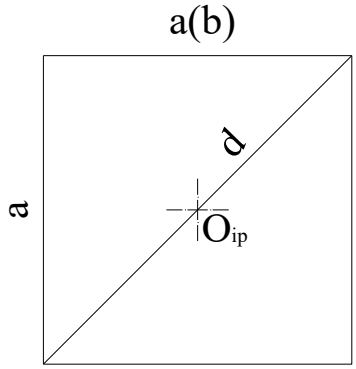

Figure 1 Diagram for determining the diagonal of the hoisting vessel with a rectangular cross-section (O_{ip} – center of gravity of the hoisting vessel)

The second condition, or the second equation, is that the height of the skip (h_s) is equal to twice the value of the diagonal of the skip's cross-section.

$$h_s = 2d,\ m \tag{18}$$

That is, based on formula (17), the value of the diagonal is

$$h_s = 2d = 2a\sqrt{2}\,,\ m \tag{19}$$

This value for the height of the skip can be substituted into the equation for the skip's volume, yielding:

$$V_s = a^2 \cdot h_s = a^2 \cdot 2a\sqrt{2} = 2a^3\sqrt{2}\,,\ m^3 \tag{20}$$

Considering that the volume of the skip is already known, the side length of the square cross-section of the skip can be calculated from this equation.

$$a = \sqrt[3]{\frac{0{,}5V_s}{\sqrt{2}}}\,,\ m \tag{21}$$

When this value is known, the cross-sectional area and the diagonal of the cross-section can be calculated:

$$\begin{gathered} P_p = a^2,\ m^2 \\ \mathrm{d} = a\sqrt{2},\ m. \end{gathered} \tag{22}$$

From these two equations, the dimensions of the rectangle (a, b) can be obtained if a rectangular cross-section of the skip is required:

$$P_p = a \cdot b,\ m^2$$
$$d = \sqrt{a^2 + b^2},\ m. \tag{23}$$

Where P_p and d are known values.

Therefore, even in the case of a required rectangular cross-section, the calculation is initially performed as if a square cross-section is used, and then the exact dimensions of the rectangle in the cross-section are retroactively calculated. From Table 1, the ratio of the longer to the shorter side of the rectangle is 1:0.9 to 1:0.8, so this should be considered when selecting the sides.

2.2 Graphical determination of the shaft dimensions

The dimensions of the cross-section are determined graphically by plotting (at a scale of 1:1) the selected hoisting vessels, considering the minimum required distances according to the relevant standards.

The mathematically and graphically determined elements are sufficient for constructing the appearance of the cross-section.

One of the possible cross-sections with two hoisting vessels is shown in Figure 2.

The labels from Figure 2 are:

- a – length of the hoisting vessel, m,
- b – width of the hoisting vessel, m,
- c – distance between hoisting vessels, m,
- d – eccentricity, m,
- e – distance from the outermost point of the hoisting vessel to the side of the structure (support), m,
- f – distance from the edge of the hoisting vessel to the support, m,
- m and n – dimensions of the guide, m,
- D – clear diameter of the shaft, m,
- C – center of the shaft.

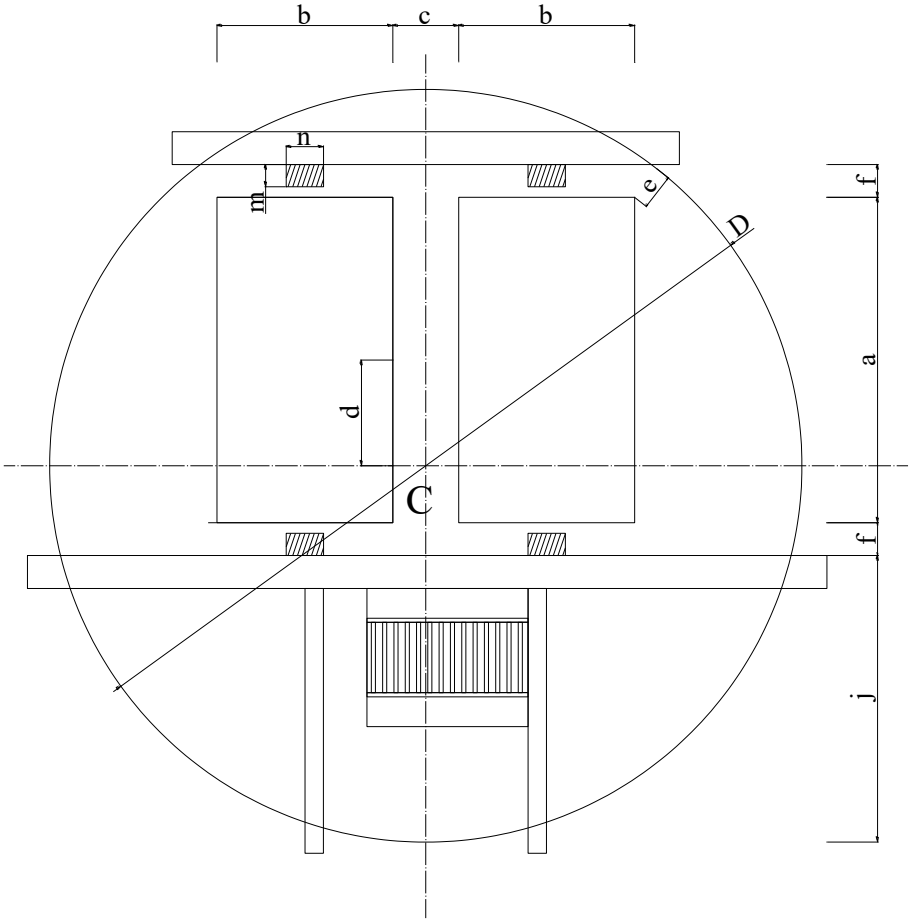

Figure 2 Shaft with a circular cross-section (two skips, pass-through section)

The listed values are variable and depend on the capacity and dimensions of the hoisting vessels. As an illustration of this statement, data is provided in Table 1, where the change in these values is shown depending on the skip's capacity.

Table 1 Adopted distances and dimensions for specific skip volumes (Musić, 2014

Skip (m^3)	D (m)	a (m)	b (m)	c (m)	d (m)	e (m)	f (m)
1	2,96	1	0,9	0,2	0,39	0,14	0,17
2	3,38	1,3	1,1	0,2	0,34	0,14	0,18
3	4,15	1,8	1,45	0,25	0,23	0,14	0,18

Since this paper presents the complete calculation up to the precise dimensions of the skips, the remaining dimensions (c, d, e, f, ...) are adopted from the corresponding tables.

Graphical determination is based on the same principle for both square and rectangular cross-sections of the skip. The design begins by drawing the skip with side a, as shown in Figure 3. In the cross-section, the diagonal contains the central point of the skip (the center of gravity), O_{ip}.

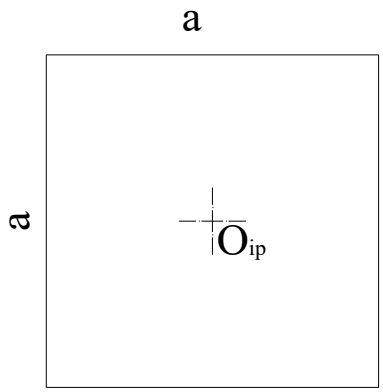

Figure 3 Skip with side a

From the right side of the skip, an auxiliary line is drawn at a distance of *c/2*, parallel to the right side of the skip. At a distance of *d* from the projection of point O_{ip} onto this line, the center of the shaft cross-section is located, as shown in Figure 4.

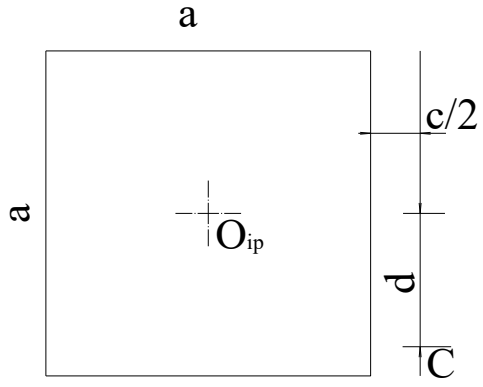

Figure 4 Determination of the shaft center

At a distance of *c* from the right side of the skip, a second skip/counterweight (usually of the same size) is drawn. Center *C* is connected to the upper left corner of the skip, and then extended by a distance e, which gives the radius of the shaft, as shown in Figure 5.

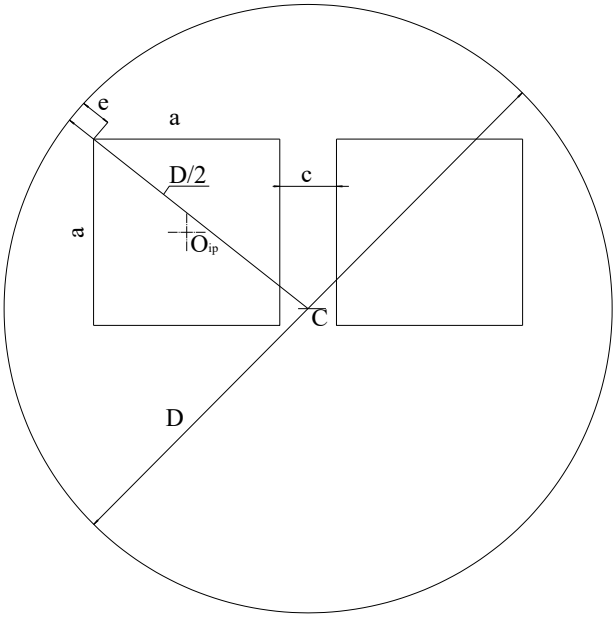

Figure 5 Determining the radius of the shaft

Finally, at a distance of *f* from the lower edge of the skip, the main and auxiliary transverse steel supports are projected. In the remaining part of the cross-section, the departments are organized: a passage section with a ladder and rest areas, as well as sections for necessary pipelines, cables, and other equipment (Figure 6).

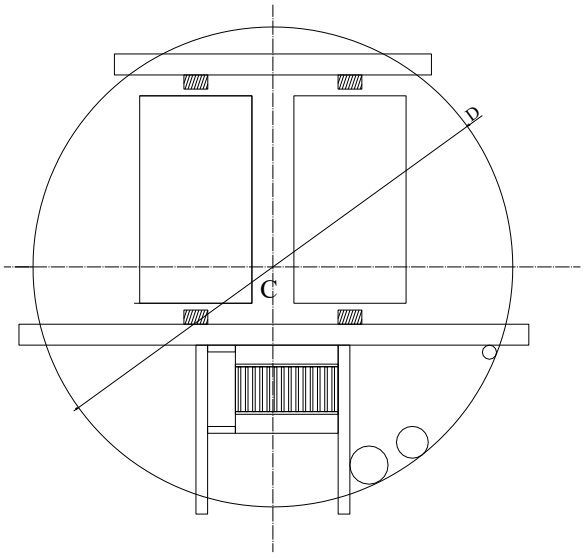

Figure 6 Construction of the entire shaft

As already mentioned, skips are custom-made. The dimensions of the shafts depend on the dimensions of the skips, which are determined by the capacity of the mine and the shaft depth. When constructing the shafts, it is also necessary to determine the thickness of the required support structure (lining) in order to calculate the sufficient area of the excavation cross-section, whose diameter (D_{isk}) is equal to the sum of the diameter of the clear cross-section (D_{sv}) (shown in Figure 6) and twice the thickness of the support structure (Dp), as shown in Figure 7.

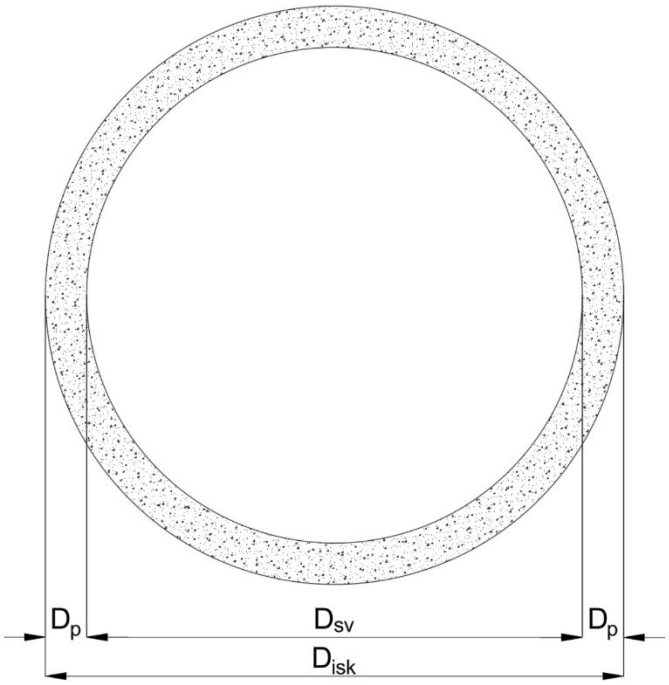

Figure 7 Diameters of different cross-sections

For the sake of unification, it is recommended that, based on the data obtained in this way, a standard cross-section be adopted according to the applicable standard (ISS, 1978), with dimensions no smaller than those calculated. The excavation diameter of the shaft will depend on the dimensions of the calculated and adopted support structure.

3 CONCLUSION

Modern mining science and practice face very complex problems related to the opening of new ore deposits at great depths. The opening of these deposits is typically done using shafts. It is always necessary to construct at least two shafts, one of which is the hoisting shaft.

In the field of hoisting shaft dimensioning, many decisions are still made based on experience. The choice of optimal shaft dimensions is crucial, with very little space for error, because in the case of a wrong decision, some of the most important conditions for exploitation will not be met. Often, the shaft is built with larger dimensions, with a certain safety factor. If the shaft dimensions are insufficient, it will conflict with the required mine capacity and will not meet the requirements in that regard. However, if the dimensions are too large, the costs and construction time exponentially increase. In addition to higher consumption of explosives, energy, and drilling elements, labor costs also increase because it takes longer to construct larger room profiles.

In this paper, the required volume of the skips was calculated, using the mine capacity and shaft depth as input data. Based on that, the required time for transporting the ore to the surface was calculated, and then the required skip volume to meet the capacity condition was determined. Unlike previous literature, where tabular values for distances and dimensions were adopted based on volume, this paper solves two equations with two unknowns to calculate the exact dimensions of the skips, from which the shaft diameter is graphically determined, and its cross-section is designed. This calculation can be used for multiple cases (two skips, skip with counterweight, etc.) and for different cross-sections (square, rectangular, or combined).

It should be noted that there are standards in this field that can help verify the calculated and graphically determined dimensions. There are also catalogs of designed, most used cross-sections.

ACKNOWLEDGEMENT

The research presented in this paper was conducted with the financial support of the Ministry of Science, Technology, and Innovation of the Republic of Serbia, within the framework of funding for scientific research at the University of Belgrade, Faculty of Mining and Geology in Belgrade, under contract number 451-03-136/2025-03/200126. The authors from Faculty of Technical Sciences in Kosovska Mitrovica would like to thank the Ministry of Science, Technological Development and Innovation of the Republic of Serbia for funding the scientific research work, contract no. 451-03-65/2024-03/200155, realized by the Faculty of Technical Sciences in Kosovska Mitrovica, University of Pristina.

REFERENCES

ANTUNOVIĆ KOBLIŠKA, M. (1973) *Opšti rudarski radovi*, Građevinska knjiga, Belgrade.

HARTMAN HOWARD L., *SME Mining Engineering Handbook*, Society of Mining, Metallurgy and Exploration, Inc. Littleton, Colorado, 1992.

TORBICA, S. & LAPČEVIĆ V. (2020) *Metode podzemnog otkopavanja*, Faculty of Mining and Geology - University of Belgrade.

MUSIĆ, O, (2014) *Projektovanje podzemnih rudnika – skripta*, Rudarsko-geološko-građevinski fakultet - Univerzitet u Tuzli, Tuzla, Bosna i Hercegovina.

JOVANOVIĆ, P. (1982) *Izrada jamskih prostorija*, Univerzitet u Beogradu – Rudarsko-geološki fakultet, Beograd.

PAVLOVIĆ, V. (1963) *Transport i izvoz u rudnicima*, Zavod za izdavanje udžbenika, Beograd.

GRUJIĆ, M. (1999) *Transport i izvoz u rudnicima*, Univerzitet u Beogradu – Rudarsko-geološki fakultet, Beograd.

Službeni list SFRJ (1992) Pravilnik o tehničkim normativima pri prevozu ljudi i materijala oknima rudnika, Beograd.

ISS – Institute for Standardization of Serbia (1978) Standard SRPS B.Z0.108:1978, Belgrade

UNDERGROUND MINING ENGINEERING 46 (2025) 153-160 UDK 62
UNIVERSITY OF BELGRADE - FACULTY OF MINING AND GEOLOGY EISSN 2560-3337

Review paper

APPLICATION OF SMALL SELF-PROPELLED DRILL RIGS

Nikola Simić[1], Stefan Milanović[1], Lazar Kričak[1], Milanka Negovanović[1], Nikola Đokić[2]

Received: May 13, 2025 **Accepted:** June 20, 2025

Abstract: Small-diameter drilling is used in many civil and mining engineering applications. In the past, it was mainly performed with hand-held hammer drills. However, the need for safer and more efficient work has led to the development of small self-propelled drilling machines that require fewer workers to achieve the same output while providing significantly safer working conditions.

Small-diameter boreholes are used in specialized blasting methods (e.g., blasting in urban areas, secondary boulder blasting), during the extraction of decorative stone blocks, for installing anchors in slope stabilization, in underground mining, in the application of expansive mortar for the disintegration of solid masses (stone, concrete), for creating protective screens, tunneling, and more.

Several manufacturers produce small self-propelled drill rigs, all equipped with remote controls. This eliminates the need for the operator to stand in potentially hazardous positions, as is required when using hand-held hammer drills. This paper presents the capabilities and application methods of these drill machines under various working conditions.

Keywords: drill rigs, drilling, mining, small diameter boreholes, excavation

1 INTRODUCTION

Boreholes are cylindrical holes drilled into rock for various purposes (Purtić, 1991). Throughout history, the drilling process has significantly evolved, from manual techniques using primitive tools to the fully automated, self-propelled machines used today.

Modern self-propelled drills operate using the principle of percussive-rotary drilling. This technique involves a chisel blade that is impacted by a piston. The blade penetrates the rock, and after each impact, it rotates by a specific angle to shear material at the borehole's bottom, shaping it into an oval. The rock is primarily fractured by the impact,

[1] University of Belgrade - Faculty of Mining and Geology, Belgrade, Serbia
[2] IGM Mladost, Leskovac, Serbia

E-mails: nikola.simic@rgf.bg.ac.rs; stefan.milanovic@rgf.bg.ac.rs, ORCID: 0000-0002-7823-5868; lazar.kricak@rgf.bg.ac.rs, ORCID: 0000-0003-4761-8716; milanka.negovanovic@rgf.bg.ac.rs, ORCID: 0000-0003-4761-8716; nikola.djokic@mladost.co.rs

so the striking force exceeds the rotational force. The chisel is simultaneously affected by static axial pressure, dynamic piston impact, and rotational torque (Purtić, 1991).

For the chisel blade to penetrate the rock, the specific pressure exerted must exceed the rock's compressive strength. Penetration is possible only when the combined static axial and dynamic impact forces meet or exceed the rock's compressive strength at the point of contact (Purtić, 1991).

A stable suspension system allows these machines to traverse uneven terrain. Their low noise and dust emissions make them ideal for urban environments. Their compact design ensures easy transportation between drilling sites and simplifies servicing, reducing maintenance downtime (Negovanović & Kričak, 2021).

2 CHARACTERISTICS OF SMALL SELF-PROPELLED DRILL RIGS

Several globally recognized manufacturers offer small self-propelled drill rigs that have proven to be reliable and cost-effective. The most notable manufacturers include Epiroc (formerly Atlas Copco) and Sandvik (Negovanović & Kričak, 2021).

Below are examples of specific drill rig models and their key characteristics.

2.1 FlexiROC T15 R surface top hammer drill rig

The FlexiRoc T15 R drill is a machine that has proven itself in demanding locations, providing easy transfer from location to location and excellent stability when moving. It has the possibility of additional anchoring for greater stability on uneven terrain, as well as support in the form of a "leg" when driving on slopes (Epiroc, 2024a). The technical characteristics of the FlexiROC T15 R small rotary drill are given in Table 1.

Figure 1 Small self-propelled drill machine FlexiRoc T15

Table 1 Technical specifications of FlexiRoc T15 R (Epiroc, 2024a)

Hole range					
Rock drill	Threads	Maximum hole length (m)	Drill diameter (mm)	Drill rod length (mm)	
COP 1022	HEX 22x108	9	Ø 27–45 mm	3 660 mm	
COP 1028	R28, SR28, R32, SR32	9	Ø 33–51 mm	3 660 mm	
Hydraulic rock drill					
Rock drill	Impact power	Hydraulic pressure, max	Impact rate	Torque at shank, max	Weight approx
COP 1022	4.5 kW	150 bar	70 Hz	126 Nm	50 kg
COP 1028	5.5 kW	185 bar	50 Hz	205 Nm	51 kg
Compressor- Atlas Copco C55 C106 GD, screw compressor					
Working pressure, max				2.5 bar	

2.2 Surface top hammer drill rig Command DC130Ri

The Commando DC130Ri is a remotely operated drill rig engineered for versatile applications such as road construction, demolition, and foundation work. Its modular design allows for upgradeability, making it a highly adaptable and multi-functional machine. Thanks to its compact dimensions and well-balanced structure, the DC130Ri offers excellent maneuverability, even in confined or uneven terrains. High-torque drive motors enhance mobility, while its lightweight frame facilitates easy transportation between job sites. Additionally, the modular layout simplifies maintenance, reducing downtime and operational costs.

Figure 2 Self-propelled drill for drilling small diameters Sandvik Command DC130Ri (Sandvik, 2024)

The drill's low noise and dust emissions make it ideal for use in urban environments. Its platform is easily adaptable for a range of applications, including secondary blasting, foundation drilling, and trenching.

Table 2 Technical characteristics of the drill machine Command DC130Ri (Sandvik, 2024)

Hole diameter	22–45 mm
Rock tools	H19, H22, H25, R23, R25, R28
Rock drill	RD106, 5.5 kW / 7.4 hp
Engine type	CAT C2.2 Tier 3
Engine output	36.3 kW / 48.7 hp
Flushing air	1.2 m^3/min, up to 8 bar
Control method	Radio remote
Total weight	3,250 kg
Transport length	5.1 m
Transport width	1.85 m
Transport height	2.3m

3 APPLICATION OF DRILLING MACHINES

Drilling small-diameter boreholes is widely used across various applications, making these machines valuable in numerous fields. The most common uses include underground exploitation of solid mineral resources, specialized blasting operations where environmental protection is a priority, the application of expansive mortars, tunnel construction, and slope stabilization through the installation of anchors and protective nets to prevent rockfalls.

3.1 Application of small self-propelled drill rigs for blastholes

To exploit solid mineral raw materials underground, small-diameter boreholes were mainly drilled with manual hammer drills. This method required a larger number of workers and made it much more difficult to achieve the desired number of drilled meters. Specialized machines are used for larger mines. These are boomer drilling machines with multiple drilling branches that can simultaneously drill a greater number of boreholes (>1).

Self-propelled drills for drilling small-diameter boreholes are primarily intended to replace manual hammer drills, of course, where possible. Also, in addition to the underground exploitation of solid mineral raw materials, the use of explosives in tunnel construction, special blasting for the excavation of foundation pits during the construction of facilities for various purposes, stabilization of slopes for road construction, secondary blasting of boulders, construction of channels, etc., is included. Figure 3 shows the Atlas Copco FlexiROC T15 self-propelled small-diameter borehole drill drilling a minefield in urban conditions.

Figure 3 Atlas Copco FlexiRoc T15 self-propelled drill machine on worksite

3.2 Application of small self-propelled drills for expansive mortar

Expansive mortar is increasingly being used; therefore, boreholes with small diameters are being drilled for these purposes. Boreholes for the application of expansive mixtures are made at close distances according to the manufacturer's scheme (Table 3). The application of these mixtures requires a much larger number of boreholes than is the case with the use of explosives, which is logical when comparing the characteristics of explosive and expansive mortars.

Table 3 Characteristics of boreholes depending on the rock in which expansive mortars are applied (Quaryingtools, 2024)

Materials & purpose	Borehole design		
	Diameter（mm）	Borehole spacing	Depth
Soft stone quarrying	28-38	200-300mm	105% of height
Hard stone quarrying	30-40	200-300mm	105% of height
Stone cutting	28-38	200-400mm	90% of height
Plain concrete demolition	30-40	300-500mm	80% of height
Reinforced concrete demolition	35-40	150-300mm	90% of height

The expansion mixture is mixed with water and poured into pre-drilled boreholes in rock or concrete. The resulting mixture swells and exerts considerable expansion pressure on the walls of the borehole, breaking the rock and separating it along the length of the borehole lines (Negovanović et al., 2024).

Drilling boreholes for the use of expansive mixtures is applied in the exploitation of decorative stone and in the creation of protective screens that serve to prevent the propagation of waves behind them (Negovanović et al., 2024).

3.3 Application of small self-propelled drill machines for slope stabilization

Self-propelled drills used for drilling small-diameter boreholes are employed to secure slopes by placing anchors for stabilization. They are also used when installing protective nets that prevent rockfalls.

Figure 4 Construction of boreholes to stabilize the slope (Epiroc, 2024b)

Figure 5 Protective net-protection against the rock fall (Geotech, 2024)

4 CONCLUSION

Small self-propelled drill rigs are equipped with surface hammers and have four-wheel drive, enabling easy movement on uneven terrain. Due to their low noise and dust levels, they have proven to be excellent for working in urban environments. They are also easy to service, reducing maintenance downtime.

These machines have significantly improved the drilling process in many areas, with the most notable advancements in mining and construction. The mobility of these machines and the use of remote control have increased worker safety because the drilling process is indirectly, i.e., passively, controlled through the operator's commands. In contrast, when using hand-held hammers, everything depends on the driller, who relies mostly on physical strength and is directly exposed to dust, water, and the risk of injury.

More and more drilling machine manufacturers are including small self-propelled drill rigs in their product lines as the range of applications expands. The small mass of these machines enables great mobility on construction sites, as they can be moved from one part of the site to another using cranes. These drills can be used for anchoring and slope stabilization, greatly increasing operator safety.

ACKNOWLEDGMENT

The authors thank the Serbian Ministry of Education, Science, and Technological Development for their support and the funds provided under contract no. 451-03-136/2025-03/200126.

REFERENCES

PURTIĆ, N. (1991). Drilling and blasting. Faculty of Mining and Geology, Belgrade, Serbia.

NEGOVANOVIĆ, M. & KRIČAK, L, (2021) Modern self-propelled surface drill rigs for drilling small diameter holes in mining and construction operations in *8th International Conference Mining And Environmental Protection*, Sokobanja, 22 – 25th September 2021 SERBIA, University of Belgrade, Faculty of Mining and Geology, Belgrade, Serbia (2021), ISBN: 978-86-7352-372-9

Epiroc (2024a) Epiroc FlexiROC T15 Surface drill rig for quarrying and construction [Online] Available from: https://pdf.directindustry.com/pdf/epiroc/flexiroc-t15-r/59040-772571.html [Accessed 20/10/2024].

Sandvik (2024) Self-propelled drill rig Sandvik Command DC130Ri. [Online] Available from: https://www.rocktechnology.sandvik/en/products/equipment/surface-drill-rigs/ [Accessed 25/11/2024].

QUARRYINGTOOLS (2024) Split star expansive mortar for rock cracking and reinforce concrete demolishing. [Online] Available from: https://www.quarryingtools.com/split-star-High-Range-Soundless-Cracking-Agent-Expansive-Mortar-Demolition-Powder-pd90861316.html [Accessed 28/11/2024].

NEGOVANOVIĆ, M., KRIČAK, L., MILANOVIĆ, S., SIMIĆ, N. AND MAJSTOROVIĆ, J. (2024) Application of Expansive Mortars for the Formation of Artificial Screens During Blasting in Urban Area“ in *31st International Conference Ecological Truth and Environmental Research*, Sokobanja, 18 – 21st June 2024 SERBIA, University of Belgrade, Faculty of Mining and Geology, Belgrade, Serbia (2024), ISBN: 978-86-6305-152-2

Epiroc (2024b) Epiroc FlexiROC T15 Surface drill rig [Online] Available from: https://epiroc.scene7.com/is/image/epiroc/FlexiROC+T15R+4?$landscape1600$ [Accessed 21/10/2024]

Geotech (2024) Fall protection net [Online] Available from: https://www.geotech.hr/wp-content/uploads/2018/03/zastita-od-odrona-9-min.jpg [Accessed 18/11/2024]

UNDERGROUND MINING ENGINEERING 46 (2025) 161-173 UDK 62
UNIVERSITY OF BELGRADE - FACULTY OF MINING AND GEOLOGY EISSN 2560-3337

Professional paper

PLANNING THE OPERATION OF Li-ION BATTERY-POWERED TRUCKS

Vladimir Milisavljević[1], Ognjen Popović[1], Dragana Savić[2], Alberto Martinetti[3]

Received: May 23, 2025 **Accepted:** June 03, 2025

Abstract: This paper analyses the planning of operation for underground mining trucks powered by lithium-ion batteries. Trucks supplied by the companies Epiroc and Sandvik are used as examples, comparing their characteristics with equivalent diesel-engine models. These trucks have similar payload capacities and dimensions, but significant differences in available energy, demonstrating that battery-powered trucks have substantially lower autonomy. The paper describes a method for estimating the autonomy of battery-powered trucks, considering motor efficiency, energy losses, and regenerative braking. A procedure is presented for determining the energy consumption for truck movement along a known route, considering the total resistance. It is demonstrated that the lower available energy of battery-powered trucks is a major factor necessitating a different approach to planning their operation in underground mining.

Keywords: transportation planning, batteries, available energy, trucks

1 INTRODUCTION

The development of battery-powered mobile mining machines has become increasingly evident in recent years, largely driven by advancements in Li-ion battery technology. Original equipment manufacturers (OEMs) of underground mining machinery have recently integrated several battery-powered mobile machines into their product lines. This shift reflects a broader trend towards more sustainable and efficient mining operations.

Lithium-ion (Li-ion) batteries were introduced in the late 20th century and have found widespread application in the consumer electronics industry (mobile phones, portable computers, etc.). In addition, the prevailing solutions for secondary sources of electrical energy for electric vehicles are also based on lithium-ion batteries. Consequently, research related to this type of battery has focused on various lithium compounds used for making the anode and electrolyte. So far, the most widely used batteries are those

[1] University of Belgrade - Faculty of Mining and Geology, Đušina 7, Belgrade, Serbia
[2] Mining Institute Ltd. Batajnički put 2, Zemun, Belgrade, Serbia
[3] University of Twente, Faculty of Engineering Technology, Enschede, Netherlands

E-mails: vladimir.milisavljevic@rgf.bg.ac.rs ORCID: 0000-0002-3713-0138; r705-21@rgf.bg.ac.rs: 0000-0001-9005-0092; dragana.savic@ribeograd.rs ORCID: 0009-0002-3396-9435; a.martinetti@utwente.nl 0000-0002-9633-1431

made from lithium compounds with nickel (Ni), cobalt (Co), and manganese (Mn), as well as lithium compounds with phosphate groups (PO4). However, advances in this field are being rapidly achieved (He F., 2016).

Leading European manufacturers of underground mining machinery have begun supplying users with mobile machinery powered by Li-ion batteries, as regularly reported on their websites. The reasons for this technological development include the improvement of working conditions and worker safety, reduction in ventilation requirements, lower operational costs, and more (Soofastaei et al, 2018; Energy Efficiency Opportunities, 2010). The Li-ion battery-powered machines currently offered by companies like Epiroc and Sandvik include underground loaders, trucks, and drill rigs.

Epiroc, a company involved in manufacturing machinery for the mining industry, has been producing battery-powered machines for some time now. In addition to several drill rigs, Epiroc produces two battery-powered loaders (ST14 Battery and ST18 Battery) as well as the MT42 SG Battery truck. The vehicles from this company use NMC lithium-ion batteries. Similarly, Sandvik is keeping pace with technology by producing and enhancing battery-powered vehicles. Alongside battery-powered drill rigs, Sandvik manufactures the LH518B loader and the TH550B truck. The electric vehicles from this manufacturer use lithium iron phosphate batteries ($LiFePO_4$ - LFP).

2 CONCEPT OF AVAILABLE ENERGY FOR MOBILE MACHINES

The fundamental approach of both Epiroc and Sandvik has been to adapt existing diesel-powered machines to the new technology, ensuring that the new Li-ion battery-powered machines have similar characteristics. Underground trucks can used as an example.

Epiroc produces the Minetruck MT42 and has utilized this platform to develop the battery-powered underground truck Minetruck MT42 SG Battery (Figure 1). These trucks have the same payload capacity, nearly identical engine power, and dimensions. The empty truck weight is also similar—34.5 tonnes for the MT42 and 37.7 tonnes for the MT42 SG.

Minetruck MT42 (diesel)

Payload: 42 t; Engine power: 399 kW;
LxWxH: 10945x2689x3050 mm

Minetruck MT42 SG (Li-ion battery)

Payload: 42 t; Engine power: 2x200 kW;
LxWxH: 10945x2689x3095 mm

Figure 1 Underground truck by Epiroc (www.epiroc.com)

Sandvik offers the diesel-powered underground truck Toro TH551i, on the basis of which the TH550B truck, powered by Li-ion batteries, was developed (Figure 2). These trucks also have similar payload capacities and dimensions, as well as comparable empty truck weights (46.9 tonnes for the TH551i versus 49.6 tonnes for the TH550B). The only significant difference is in the engine power, as the diesel engine power is 515 kW, while the TH550B truck has four motors located in wheel hubs, each with a power output of 180 kW (for a total of 720 kW).

It can be observed that the characteristics of trucks powered by Li-ion batteries are largely aligned with those of diesel-powered trucks.

Toro TH551i (diesel)

Payload: 51 t; Engine power: 515 kW;
LxWxH: 11500x3200x3200 mm

TH550B (Li-ion battery)

Payload: 50 t; Engine power: 4x180kW;
LxWxH: 11000x3350x2900 mm

Figure 2 Underground truck by Sandvik (www.sandvik.com)

The main difference between diesel-powered trucks and those powered by Li-ion batteries is the available energy to perform work. Epiroc's MT 42 truck has a diesel fuel tank capacity of 580 Liters, whereas Sandvik's Toro TH551i truck has a tank capacity of as much as 840 Liters. To determine the available energy from these quantities of fuel, the lower heating value of diesel, which is 35.9 MJ/l (Davis S.C., Boundy R.G., 2022), will be used. On the other hand, the mentioned companies have provided the following battery capacities for their battery-powered trucks: 375 kWh for the Epiroc Minetruck MT42 SG and 354 kWh for the Sandvik TH550B.

To compare the available energy of these machines accurately, it is necessary to consider the efficiency of the drive motors. The efficiency of internal combustion engines running on diesel fuel is about 30%, while the efficiency of AC synchronous electric motors is approximately 95% (Đajić, 1981; Aleksandrović, 2017). Table 1 lists the available energies (in GJ) for the trucks mentioned above, for both types of used energy, with and without accounting for motor efficiency.

Table 1 Comparison of Available Energy (in GJ) for Diesel-Powered and Battery-Powered Trucks

Available Energy (GJ)	**Epiroc MT 42**	**Sandvik Toro TH551i**
Diesel (overall)	20,822	30,156
Diesel (Engine efficiency – 30%)	6,247	9,047
	MT 42 SG	TH 550B
Li-ion batteries (overall)	1,350	1,274
Li-ion batteries (Engine efficiency – 95%)	1,283	1,211

Conversion: 1 kWh = 3,6 MJ

It can be observed that underground trucks powered by Li-ion batteries have significantly lower available energy compared to their diesel-powered counterparts. The MT 42 SG has approximately 20% of the available energy of the Epiroc MT42, while the TH 550B has only about 13% of the Toro TH551i's energy capacity. The lower available energy of the TH 550B is primarily due to the large fuel tank of the Toro TH551i. Additionally, Sandvik's batteries are based on LFP (lithium iron phosphate) Li-ion cells, which have lower energy density compared to the NMC cells used by Epiroc (a drawback compensated by greater stability and longer lifespan).

Additionally, the low efficiency of internal combustion engines has been mitigated by increasing the fuel tank capacity.

3 MINE TRUCKS PERFORMANCE PLANNING PROCEDURE

The standard procedure for calculating the movement of vehicles on pneumatic tires is based on the relationship between engine power (N_m), effective traction force (P_t), and vehicle speed (v).

$$N_m = \frac{P_t \cdot v}{\eta_p}\ [W] \ \rightarrow \ P_t = \frac{N_m \cdot \eta_p}{v}\ [N] \tag{1}$$

where:

η_p – power transmission efficiency coefficient from the engine to the traction wheels.

The traction force determined in this manner is parallel to the ground surface and directed in the rolling direction of the wheel. Moreover, its maximum value is constrained by the wheel-to-surface adhesion conditions and depends on the adhesive weight of the vehicle (L_a) and the adhesion coefficient (ϕ).

$$P_{t\,max} \leq L_a \cdot \varphi\ [N] \tag{2}$$

On the other hand, the traction force must be sufficient to overcome the total resistance (W_u) that opposes the movement of the vehicle.

$$P_t \geq W_u = W_o + W_v \pm W_n + W_r \pm W_i \tag{3}$$

The total resistance is the sum of primary and secondary resistances, where the primary resistances include rolling resistance (W_o) and aerodynamic drag/resistance (W_v), while the secondary resistances are grade resistance (W_n), curve resistance (W_r), and inertia resistance – accelerating/braking (W_i). The primary resistances act continuously during the motion of vehicle, whereas the secondary resistances vary depending on route characteristics (grade and curve resistance) and vehicle movement conditions (inertial mass resistance—acceleration or deceleration). These resistances are expressed in Newtons.

In practice, these resistances are calculated as the product of the total vehicle weight (L), expressed in kilonewtons, and the specific resistance values, expressed in N/kN, except for aerodynamic drag/resistance. An overview of the calculations for individual resistances is provided in Table 2.

Table 2 Overview of primary and secondary resistances for vehicle in motion (Simonović, 1972)

Item	Resistance [N]	Specific resistance [N/kN]	Remark
Rolling resistance	$W_o = L \cdot w_o$	w_o	Empirical value.
Aerodynamic drag	$W_v = \frac{1}{2} \cdot c \cdot \rho \cdot F \cdot v^2$	-	No specific value.
Grade resistance	$W_n = \pm L \cdot w_n$	$w_n = \pm i$	i is route grade in ‰.
Curve resistance	$W_r = L \cdot w_r$	$w_r = 30 \cdot \frac{200 - r}{200}$	r is curve radius.
Inertia resistance	$W_i = \pm L \cdot w_i$	$w_i = 102 \cdot (1 + \varepsilon) \cdot a$	ε is inertia coef. of rotating parts; a is acceleration/deceleration.

This approach allows us to divide the entire vehicle route into segments in which the sum of individual resistances remains constant. In other words, the route (S) consists of (n) segments where, on each segment, the sum of primary and secondary specific resistances is constant. This can be expressed as follows:

$$S = \sum_{j=1}^{n} s_j \ [m] \quad where\ for\ each\ s_j\ it\ follows \quad w_{uj} = const\ [N/kN] \tag{4}$$

Based on the assumption that the segment lengths are known, along with the specific conditions of the route (w_o, w_n, w_r, etc.), the fundamental problem in the analysis of truck transport is thus reduced to determining the speed of truck movement along individual segments, and consequently, the time required for this movement. The result of such an analysis is the time needed to complete one cycle of truck movement along the given route.

The procedure described is suitable for determining the haulage capacity of a single truck, which is then further used to determine the required number of trucks to achieve the designed overall haulage capacity. So far, this type of calculation has been primarily applied to trucks equipped with diesel IC engines.

4 LI-ION BATTERY POWERED TRUCKS OPERATION PLANNING

The above-described approach to haulage planning for trucks with Li-ion batteries will not provide valid results, as it does not account for the available energy for truck movement. In the case of diesel-powered trucks, the common practice is to refuel the tank with the necessary amount of fuel for a single shift or workday. Due to the high thermal value of diesel fuel and its substantial available energy, diesel trucks have significant autonomy, allowing them to adapt to technological requirements during operation, such as changes in the travel route.

The energy stored in truck batteries is significantly lower than the energy available in diesel-powered trucks and is evidently insufficient for autonomous operation of these machines during a single shift. Mentioned mining equipment manufacturers have developed battery-swapping systems, which allow the replacement of a discharged battery with a fully charged one. This process enables the truck to continue operations; however, it must be accounted for in planning, as additional time is required for the truck to deviate from its usual route, travel to the charging station, replace the battery, and return to regular operation.

However, the question remains: how much work can be done with the energy stored in the battery?

The following section will describe the procedure for evaluating the autonomy of Li-ion battery-powered trucks along a predefined route. This procedure is based on the aforementioned parameters and is a function of the available battery energy.

As shown in equation (3), the total resistance can also be viewed as the traction force—a force acting at the center of the wheel, directed along the direction of motion and parallel to the surface.

Equation (4) indicates that the truck's route can be divided into segments, with each individual segment having a constant value of total specific resistances. The following should be noted:

- Trucks designed for underground mining operations feature a two-part chassis, two axles, and are most commonly equipped with four-wheel drive (axle configuration 4x4, as shown in Figures 1 and 2). Loaded trucks experience a higher load on the rear axle, whereas empty trucks have a greater load on the front axle. In the following analysis, it is assumed that the load is evenly distributed across both axles and that the weight is uniformly distributed between the left and right wheels—resulting in an equal load on all wheels.
- The truck driving cycle essentially consists of hauling the load to the discharging site and returning the empty truck to the loading location. Therefore, when determining the total resistance during load hauling, both the

vehicle weight and the load weight must be considered, whereas for the return trip to the loading location, only the vehicle weight is taken into account (He et al., 2013).

Total resistance value is obtained by multiplying the specific resistances in equation (4) by the truck's weight. This resistance will be considered as the traction force exerted by the wheel on the vehicle, which remains constant along a single segment.

$$P_{t\,j} = L \cdot w_{uj} \ \ [N] \tag{5}$$

where:

P_{tj} – is a traction force along segment s_j (N).

L – is a weight of the truck (kN), where, depending on circumstances, this can be weight of loaded truck (weight of the truck combined with the weight of the load) – L_{pu} or just the weight of the truck – L_{pr};

w_{uj} – is sum of specific resistances along the segment s_j (N/kN);

The work (A_j) done by the traction force P_{tj} during movement along the segment s_j is the product of these two quantities, while the total work along the entire route is the sum of the work performed across individual segments. The work required for the movement of a loaded truck (L_{pu}) and an empty truck (L_{pr}) along the complete route can be determined as follows:

$$A_{pu} = \sum_{j=1}^{n} A_{j\,pu} = \sum_{j=1}^{n} s_j \cdot P_{tj} = \sum_{j=1}^{n} s_j \cdot L_{pu} \cdot w_{uj} \ [J] \tag{6a}$$

$$A_{pr} = \sum_{j=n}^{1} A_{j\,pr} = \sum_{j=n}^{1} s_j \cdot P_{tj} = \sum_{j=n}^{1} s_j \cdot L_{pr} \cdot w_{uj} \ [J] \tag{6b}$$

The total work, in mechanical context, during the truck's movement over one driving cycle along a predefined route, is obtained by summing equations (6a) and (6b):

$$A = A_{pu} + A_{pr} \ \ [J] \tag{7}$$

It should be emphasized that, on certain segments of the route, the sum of specific resistances (w_{uj}) may have a negative value. This can occur when the truck is moving downhill (due to a decrease in its potential energy) or during deceleration (due to a reduction in its kinetic energy). In both cases, the truck operates in a brake mode, resulting in the replacement of the traction force with a braking torque, i.e., a braking

force that also acts at the center of the wheels, is parallel to the surface, but is directed opposite to the vehicle's motion.

The truck's movement is not powered by battery energy on segments where $w_{uj} < 0$. Therefore, to accurately determine the autonomy of battery-powered trucks, these segments must be excluded from equations (6a) and (6b), and consequently from expression (7), leading to the derivation of expressions (8a), (8b), and (9):

$$A'_{pu} = \sum_{j=1}^{n} A_{j\,pu} = \sum_{j=1}^{n} s_j \cdot P_{tj} = \sum_{j=1}^{n} s_j \cdot L_{pu} \cdot w_{uj}\ [J] \qquad ,for\ w_{uj} > 0 \qquad (8a)$$

$$A'_{pr} = \sum_{j=n}^{1} A_{j\,pr} = \sum_{j=n}^{1} s_j \cdot P_{tj} = \sum_{j=n}^{1} s_j \cdot L_{pr} \cdot w_{uj}\ [J] \qquad ,for\ w_{uj} > 0 \qquad (8b)$$

$$A' = A'_{pu} + A'_{pr}\ [J] \qquad (9)$$

Work A' obtained from equation (9) represents the energy consumed for the truck's movement along the route during one cycle, which is supplied from the battery. This energy can be compared to the energy stored in the battery to assess the truck's autonomy. Similar energy analyses of vehicle movement is already common practice and is used for transport optimization (Energy Efficiency Opportunities, 2010).

It is essential to consider the limitations related to the amount of available energy that the battery can supply, as well as the losses incurred during transmission and conversion:

- Manufacturers of Li-ion batteries and researchers do not recommend their complete discharge, as it significantly reduces their lifespan (Han, 2019). In other words, when planning the operation of battery-powered trucks, the full battery capacity should not be assumed as available.
- Losses in electrical power transmission occur due to Joule heating and Ohmic resistance, both of which manifest as heat dissipation. These losses are present in all components of the electrical system, including the battery, inverters, and cables.
- Losses in the electric motor: Nearly all vehicles powered by Li-ion batteries use synchronous electric motors with permanent magnets, which have a high efficiency. The efficiency of these motors ranges from 92% to 97% (Dambrauskas, 2020).
- Losses in mechanical power transmission: These losses occur in the components of the mechanical power transmission system from the electric motor to the wheels.

The battery supplies energy to other consumers on the truck, meaning that energy is not solely used for vehicle propulsion. The largest consumer, aside from the traction motors,

is the auxiliary electric motor that powers the hydraulic pump. The power of the auxiliary motor on the trucks mentioned above is 160 kW (Epiroc) and 200 kW (Sandvik). Other consumers include the air conditioning system in operator cabin, lighting units, sensors, instruments, and similar.

One of the strategies for increasing the autonomy of electric-powered vehicles is the implementation of regenerative braking system, which is standard equipment on mining vehicles, including the trucks discussed in this study. This system enables the synchronous electric motor with permanent magnets to operate in generating mode during braking, producing electrical energy by reducing the truck's kinetic energy. The generated electrical energy is then converted and stored in the battery [Islameka M. et al., 2023].

Research on the impact of regenerative braking systems in electric vehicles indicates a possible increase in autonomy (range) of 11% to 22% (Wager et al., 2022; Berjoza, 2022), with system efficiency being higher at greater speeds, characteristic of passenger vehicles in public transportation. Mining trucks operate at relatively low speeds. In underground mining operations, vehicle speed is typically restricted (most often to 10–15 km/h), resulting in short braking and stopping times, thereby limiting the energy recovery potential from braking at a stop. Significant energy regeneration effects are only feasible on route segments where the vehicle moves downhill in braking mode.

Despite these advancements, friction brakes remain an indispensable component of underground mining trucks and other mobile mining machines as a safety measure.

Finally, the truck's autonomy or the number of cycles (n) that a battery-powered truck can complete on a predefined route can be determined using the following equation:

$$n = \frac{E_{bat}}{A' + E_{aux} - E_{rbs}} \; [cycles] \tag{10}$$

where:

E_{bat} – energy stored in the battery or battery capacity (J);

A' – energy supplied from battery for motion of the truck during a one cycle (J)

E_{aux} – energy supplied to the auxiliary motor and other consumers during a single cycle (J);

E_{rbs} – energy recovered with regenerative braking system and restored in the battery, during a one cycle (J);

Thus, after completing (n) cycles, the truck's battery will be nearly discharged and will need to be replaced to prevent excessive over discharge and potential damage. Due to possible circumstances that may cause delays or interruptions in truck movement within

an underground mine, it is expected that a battery replacement strategy will be adopted once its state of charge (SoC) drops to 25–30% to prevent degradation. While this approach would have a positive impact on battery lifespan, it would also negatively affect the realization of the designed haulage capacity due to more frequent battery replacements.

5 CONCLUSION

Battery-powered trucks are already a reality in the underground mining industry. Although significant differences from internal combustion engine trucks may not be immediately apparent, certain characteristics of this technology necessitate a different approach when planning their operation, with the most crucial one is the lower available energy of the vehicle. This underscores the importance of conducting a thorough energy analysis of truck movement.

Determining the energy required for vehicle movement is mechanically straightforward. However, a systematic approach to this task – aimed at assessing the haulage capacity of the truck along a predefined route – requires a structured energy analysis of all resistances, consumers, and losses.

This paper provides the methodology for determining the energy required for truck movement during a single driving cycle, based on primary and secondary resistances. It has been demonstrated that the energy analysis in this case includes only those segments of the route where the sum of all resistances is greater than zero, as battery energy is utilized on these segments. Additionally, constraints related to battery capacity, other energy consumers on the truck, and the regenerative braking system have been highlighted. Finally, an equation for determining truck autonomy, specifically the number of cycles a truck can complete with a fully charged battery, has been provided.

ACKNOWLEDGMENT

The research presented in this paper was conducted with the financial support of the Ministry of Science, Technology, and Innovation of the Republic of Serbia, within the framework of funding for scientific research at the University of Belgrade, Faculty of Mining and Geology in Belgrade, under contract number 451-03-65/2024-03/ 200126.

REFERENCES

SOOFASTAEI, A., KARIMPOUR, E., KNIGHTS, P., KIZIL, M. (2018), Energy-Efficient Loading and Hauling Operations. In: Awuah-Offei, K. (eds) Energy Efficiency in the Minerals Industry. Green Energy and Technology. Springer, Cham., DOI: 10.1007/978-3-319-54199-0_7

HE F. et all., (2013), Modelling of electric vehicles for underground mining personnel transport, Proceedings 8th Conference on Industrial Electronics and Applications, IEEE, Melbourne, Australia, ISBN: 978-1-4673-6321-1, DOI: 10.1109/ICIEA.2013.6566489

HE F., (2016), Energy management system for underground mine electric vehicles, Doctoral Thesis, Faculty od Science, Engineering and Technology, Swinburne University of Technology

Energy efficiency opportunities, Energy – mass balance: Transport, Version 1, (2010), National Framework for Energy Efficiency, Australian Government, Department of Resources, Energy and Tourism, ISBN: 978-1-921516-84-9

DAVIS, S.C., BOUNDY, R.G., (2022), Transportation energy data book: Edition 40, Office of Energy Efficiency and Renewable Energy, U.S. Department of Energy

ĐAJIĆ, N., (1981), Toplotni motori, Univerzitet u Beogradu, Rudarsko-geološki fakultet – udžbenik (in Serbian), prvo izdanje

ALEKSANDROVIĆ, S., (2017), Električne mašine i uređaji u rudarstvu, Univerzitet u Beogradu, Rudarsko-geološki fakultet – udžbenik (in Serbian), ISBN: 978-86-7352-292-0.

SIMONOVIĆ, M., (1972), Sredstva železničkog i automobilskog transporta na površinskim otkopima, IP Građevinska knjiga (in Serbian), Beograd.

HAN X., LU L., ZHENG Y., FENG X., LI Z., LI M., OUYANG M., (2019), A review on the key issues of the lithium ion battery degradation among the whole life cycle, eTransportation, 1, 100005, DOI: 10.1016/j.etran.2019.100005

DAMBRAUSKAS K., VANAGAS J., ZIMNICKAS T., KALVAITIS A., AZUBALIS M., (2020), A Method for Efficiency Determination of Permanent Magnet Synchronous Motor, Energies, 13, (4): 1004, DOI: 10.3390/en13041004

ISLAMEKA M., BUDIMAN B. A., JUANGSA F. B., AZIZ M., (2023), Energy management systems for battery electric vehicles, chapter in Emerging Trends in Energy Storage Systems and Industrial Applications, editors Prabhansu and Kumar N., Academic Press, Elsevier, ISBN: 978-0-323-90521-3

WAGER G., WHALE J., BRAUNL T., (2017), Performance evaluation of regenerative braking systems, Proc IMechE Part D: J Automobile Engineering, 1–14, DOI: 10.1177/0954407017728651

BERJOZA, D.; PIRS, V.; JURGENA, I., (2022), Research into the Regenerative Braking of an Electric Car in Urban Driving, World Electr. Veh. J. 2022, 13, 202, DOI: 10.3390/wevj1311020

UNDERGROUND MINING ENGINEERING 46 (2025) 175-188 UDK 62
UNIVERSITY OF BELGRADE - FACULTY OF MINING AND GEOLOGY EISSN 2560-3337

Original scientific paper

A-PRIORI ACCURACY ASSESSMENT OF TRACING THE CUT-TROUGH IN THE VERTICAL PLANE DURING THE CONSTRUCTION OF THE HAULAGE DRIFT IN THE "GROT" MINE

Aleksandar Ganić[1], Aleksandar Milutinović[1], Aleksandar Đorđević[2], Zoran Gojković[1], Nevena Đurđev[1]

Received: June 17, 2025 **Accepted:** June 28, 2025

Abstract: Mining projects for the exploitation of the grade ores encompass specific technical and technological solutions that are a consequence of the characteristic spatial position and geometry of the ore deposit, existing mining works, natural and artificial objects, and terrain relief. To realize the mining project, a series of mining and surveying tasks must be carried out in the pre-project and project phases of exploitation, as well as during the construction of mine facilities and the excavation of mineral materials. Among the various mining and surveying tasks that follow project implementation, the tracing of the cut-through or cross-cuts, between existing mine tasks is often a crucial step. For the successful execution of these tasks, it is necessary to perform an *a priori* assessment of the accuracy of the cut-through in order to define the required precision for the measurement/monitoring process, and based on that, determine the appropriate equipment and measurement method. This paper presents a *priori* assessment of the accuracy of marking the cut-through in the vertical plane during the construction of the haulage drift on the IX horizon of the "Grot" lead and zinc mine.

Keywords: underground exploitation, lead and zinc mine, mining measurements, a priori accuracy assessment

1 INTRODUCTION

The assessment of the accuracy of the marking of large and significant infrastructure facilities, as well as facilities that may pose potential risks to human health and safety, include an *a priori* evaluation. The purpose of *a priori* accuracy assessment is to define the necessary level of precision in measuring and marking angles, lengths, and height differences, which will ensure the accuracy of the marking of the designed points or object in accordance with project or previously established standards. The quality of the measured quantities can be *a priori* standardized based on the principle of equal or

[1] University of Belgrade - Faculty of Mining and Geology, Đušina 7, Belgrade, Serbia
[2] Aleko Mining Solutions, Kneževačka 19/18, 11000 Belgrade, Serbia

E-mails: aleksandar.ganic@rgf.bg.ac.rs ORCID: 0000-0002-3431-7909; aleksandar.milutinovic@rgf.bg.ac.rs: ORCID: 0000-0002-9450-2903; aleko.miningsolutions@gmail.com; zoran.gojkovic@rgf.bg.ac.rs; ORCID: 0009-0000-2642-1493; r53-24@student.rgf.bg.ac.rs

nonequal influence. An *a priori* accuracy assessment guided by the principle of equal influence ensures that each measured quantity has an equal impact on the overall standard deviation of the marking of the designed object. Conversely, in the case of nonequal influence, individual measured quantities may have a greater or lower influence on the standard deviation of the marking (Wolf and Ghilani, 1997).

On the other hand, *a priori* accuracy assessment can be performed in accordance with the projected or previously defined standard deviation of tracing, ensuring a 68.27% (1s) probability that the specified standard deviation will be achieved. However, for large and significant infrastructure facilities and works, the standard deviation of marking can be devided by 2, establishing more strict criteria for *a priori* accuracy assessment and necessitating greater precision in the measured/marked quantities. In this case, the probability of achieving the given standard deviation increases to 95.45% (2s). To attain even greater certainty in the realization of marking, the standard deviation of object marking can be reduced by a factor of three, which will ensure a 99.73% (3s) probability of tracing precision, but will also require a significantly higher accuracy of field measurements (Ganić, 2008; Schofield and Breach, 2007).

This study presents an *a priori* evaluation of the accuracy in the execution and tracing of cut-through in the vertical plane, using the construction of a haulage drift in the "Grot" mine as a case study. Given the relatively short length and simple geometry of the cut-through, for the *a priori* accuracy assessment was adopted to the 1s standard and the principle of equal influence of the measured variables on the overall error of the cut-through.

2 GEOGRAPHICAL SETTING OF THE "GROT" MINE

The "Grot" lead and zinc ore deposit is situated in the Pčinja district of southeastern Serbia, on the southeastern slope of Besna Kobila mountain (height k+1923 m). The "Grot" mine's ore field exhibits the characteristic features of a high-altitude region. It is bordered by the Vardenika mountain massif to the north, the Glok mountain to the east, the Dukat mountain to the southeast, the Patarice mountain and Srpska Čuka to the south, and the Borovik peak to the northwest (Figure 1).

Figure 1 Geographical setting of the "Grot" mine

The deposit is situated approximately 29 kilometres east of Vranje and 20 kilometres west of Bosilegrad. An 8 kilometer road leads to the "Grot" mine, branching off from the main Vranjska Banja-Bosilegrad road at the 28th kilometre, near the village of Kriva Feja. The mine's exploitation and exploration field falls under the jurisdiction of the city municipalities of Vranjska Banja and Bosilegrad, as well as the cadastral municipalities of Kriva Feja and Musulj.

3 "GROT" MINE

The first exploration activities in the "Blagodat" (nowaday "Grot") deposit commenced in 1903. These tasks were undertaken by Italian researchers in the eastern and southern parts of the deposit. The exploration continued until 1911, when excavation has been started. The Italian researchers primarily focused on extracting the richest sections of the ore bodies, which were accessible at the open levels of 1565 m, 1585 m, 1606 m, 1608 m, and 1621 m. During this period, a facility for ore preparation was also established. From 1948 to 1953, the research was reactivated, firstly by the "Mačkatica" molybdenum mine, and subsequently by the "Trepča" combine. In late 1956, following a comprehensive study by the Institute for Geological and Geophysical Research from Belgrade, a research program and project were developed, which have been implemented since 1958. Since 1963, the "Trepča" combine has overseen the research and financing. Notably, during the period of 1959-1964, more than 10 km of exploratory mining rooms and approximately 4 km of drill holes were created within the deposit. Regular exploitation started in September 1974.

Based on the limited resources remaining from the "Blagodat" mine, social company lead and zinc mine "Grot" was established on December 19, 2000. as a newly founded mining company, started exploitation in 2001. After the mine's establishment, the necessary production settings of the mining facilities and the establishing of conditions for the starting of preparation and excavation activities were carried out. During the

period from 2001 to 2007, a total of 612,850 tons of Pb-Zn ore was extracted, with an average content of 3.00% Pb and 3.84% Zn.

According to Decision BD 146657/2007 issued by the Agency for Business Registers on 07.12.2007, the official data for the business entity was changed to lead and zinc mine "Grot" a.d., which remains the name under which it currently operates.

The "Grot" lead and zinc mine exploits ore from the Grot deposit, which is situated within an area whose coordinates are presented in Table 1 and in Figure 2 (The primary mining project for the extraction of lead and zinc deposits "Grot" - Kriva Feja, 2011.).

Table 1 Coordinates of the boundary points of the mining area "Grot"

Point	Coordinates	
Number	Y [m]	X [m]
1	7 597 000	4 713 500
2	7 601 000	4 711 000
3	7 604 000	4 711 000
4	7 604 000	4 708 500
5	7 601 000	4 708 500
6	7 601 000	4 710 000
7	7 597 000	4 712 500

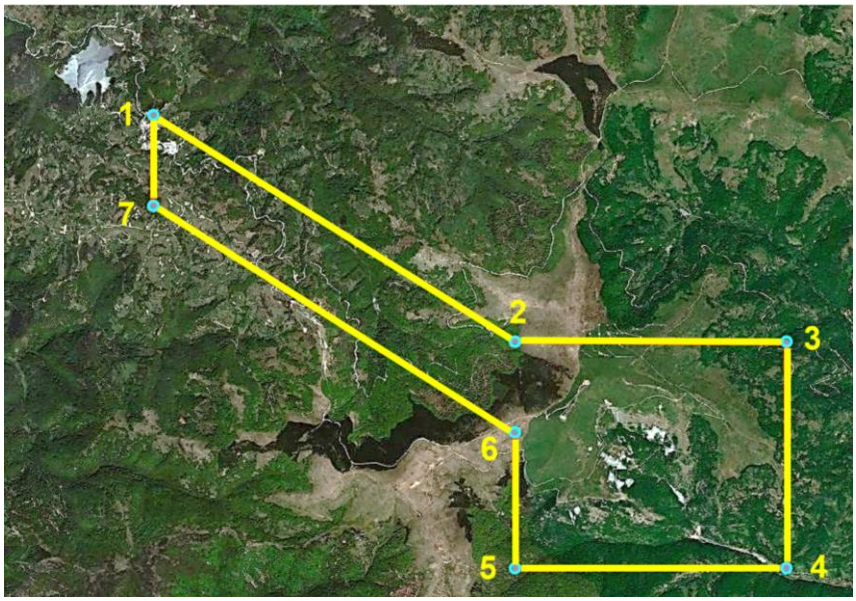

Figure 2 Exploitation field of the "Grot" mine

Until the 1960s, mining activities were confined to the extraction of exposed ore deposits through shallow adits and the declines directly from the terrain surface. Exploration efforts carried out until 1967 led to the identification of ore reserves categorized as A+B+C1 in the "Blagodat" (Table 2) deposit, which were certified by the Commission for Ore Reserves in same year.

Table 2 Certified deposit reserves from 1967.

Reserve category	Ore Reserves	The metal content	
	[t]	Pb [%]	Zn [%]
$A+B+C_1$	4 766,241	4.16	4.24

Within the mine drift, ore deposits are delineated into designated mining districts, which are then further subdivided into individual ore bodies:

- Mining district "Bare-Đavolja vodenica-Istočni revir I",
- Mining district "Vučkovo",
- East Mining district II, currently under exploration.

East Mining district I contains several notable ore bodies, including RT-10, RT-10a, and RT-11, which were formed at the contact between gneiss and schists (Technical mining project of the ore deposit extraction "Istočni revir I", 2016.). The physical characteristics and spatial distribution of these ore bodies are presented in Figures 3, 4, and 5. Additionally, the Vučkovo mine district hosts a primary lenticular ore body, RT-1, in the

form of an elongated lens situated along a steeply dipping ore structure (slope≈70°), within a sequence of biotite-sericite schists (Figure 6).

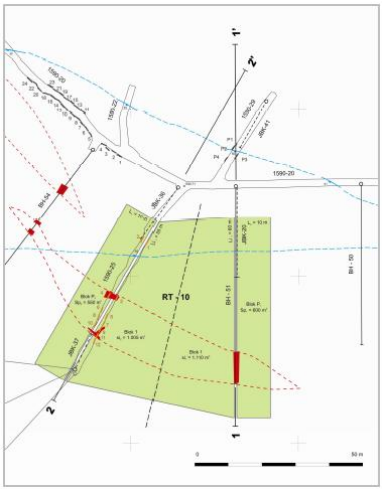

Figure 3 Ore body RT-10

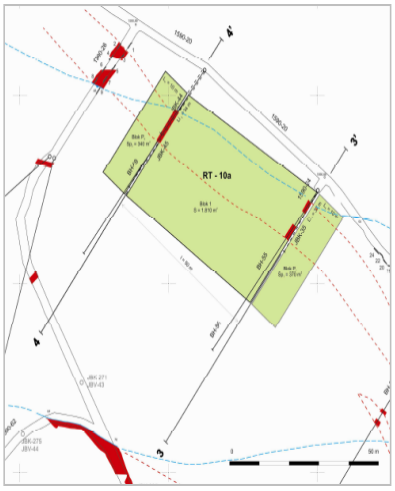

Figure 4 Ore body RT-10a

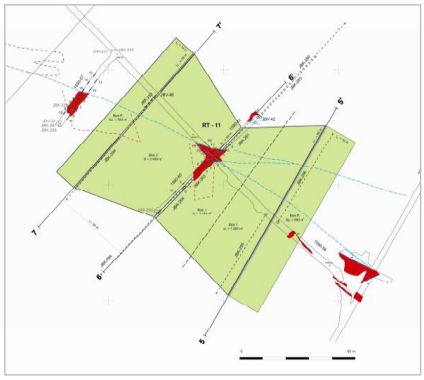

Figure 5 Ore body RT-11

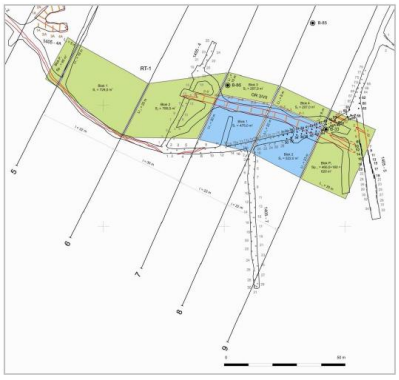

Figure 6 Ore body RT-1

Alongside the primary ore structure, a secondary wire ore deposit, designated as RT-2, was formed spanning approximately 30 meters, situated at the interface between gneissic and biotite-sericite schist lithologies, Figure 7.

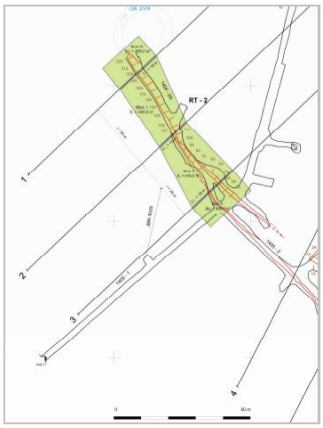

Figure 7 Ore body RT-2

The RT-3 ore deposit, unlike the preceding two previous deposits, exhibits a gentler inclination, typically up to 30 degrees, and originated at the interface between gneisses and biotite-sericite schists, Figure 8.

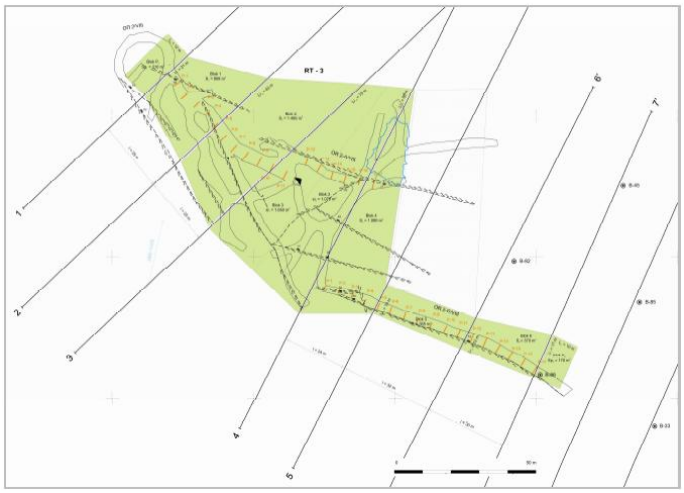

Figure 8 Ore body RT-3

Based on the contract for the development of project documentation between the Lead and Zinc Mine "Grot" a.d. (registration number 152-20-10, dated 04.12.2010) and the company "Geo Consulting Studio" in Belgrade, a study was conducted on the lead and zinc reserves in the ore bed Grot: encompassing the Bare - Đavolja Vodenica and Vučkovo deposits, as presented in Table 3.

Table 3 Ore reserves certified in the 2010 study

Mining district	Category	Deposit reserves	Average content [%]		Ore reserves [t]	
		[t]	Pb	Zn	Pb	Zn
Bare - Đavola Vodenica	C_1	133,492.80	2.98	4.40	3,983.48	5,867.83
Vučkovo	$B+C_1$	344,739.82	3.99	5.42	13,764.25	18,689.35

4 PROJECT ASSIGNMENT FOR THE DEVELOPMENT OF THE CUT-THROUGH AT THE IX HORIZON LEVEL IN THE EXPLOITATION FIELD OF THE LEAD AND ZINC MINE "GROT"

The project assignment involves constructing a haulage drift (TH) parallel to the existing main haulage drift (GTH), extending from the surface to the IX horizon level (Figure 9). Designed haulage drift TH is 494.54 meters (horizontal distance) long and primarily intended for the transport of dirt and deposit materials. By creating this additional haulage drift, the length of exporting and transporting dirt and deposit materials will be reduced. Furthermore, the establishment of this new haulage drift will facilitate more detailed exploration of the zone at the IX horizon level and the levels below, potentially leading to an increase in the exploitation field's deposit reserves and the formation of new mining works.

The dimensions of the cross-section of the current GTH system, measuring 2.5 m x 2.5 m, constrain the utilization of mechanized equipment for loading and transportation. Consequently, the designed TH haulage drift will be constructed through a single access point, directly from the surface.

Construction of the TH is planned to commence at point 1 on the field's surface and proceed towards the designated breakthrough site at point 11. The haulage drift will be built with an incline ($\boldsymbol{\delta = 0°49'42''}$) and a specific bearing ($\boldsymbol{\nu = 15°}$). The overall, actual length of the TH is 494.59 meters, with a cross section measuring 3.5 meters by 3.0 meters.

The initial point 1 on the field's surface will be marked from the existing trigonometric point T4, known as Orlov kamen. The table 4 provides the coordinates and heights of the trigonometric point, as well as the start point 1 and end point 11 of the haulage drift (Đorđević, 2020).

Table 4 Coordinates and heights of the important points

Point	Y [m]	X [m]	H [m]
T4 – Orlov kamen	7 602 866.97	4 709 281.68	1,354.38
1	7 602 730.15	4 709 415.23	1,298.84
11	7 602 861.88	4 709 891.90	1,305.99

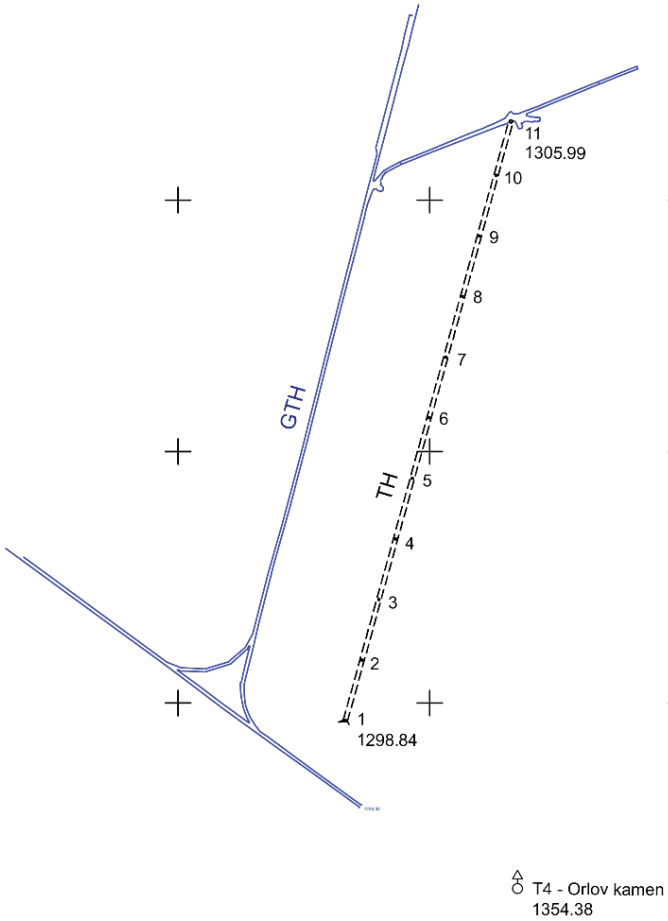

Figure 9 Designed haulage drift TH

4.1. *A priori* accuracy assessment of the cut-through in the vertical plane

To establish the cut-through in acordance with the project and within the maximum adopted error, it is necessary to make a *a priori* accuracy assessment before starting of the cut-through. The *a priori* accuracy assessment determines the standard deviations of all measured parameters, including the method and precision of marking, as well as the class of instruments that will achieve required cut-through accuracy. This paper will present *a priori* accuracy assessment of the specified cut-through on level of the IX horizon of the "Grot" mine in the vertical plane.

The project assignment does not specify the permitted error for the vertical alignment of the haulage drift markings. Following the construction of the haulage drift at the level of the IX horizon, mining operations will continue, and the permitted error for vertical plane markings is adopted as the acceptable margin of error for measuring height differences within the underground mine rooms. This error was adopted based on the Rulebook on the methodology for conducting mining surveyings (Službeni glasnik RS, 1997), and for the leveling on the primary horizon calculates the error according to the equation:

$$\Delta = 25\sqrt{L} \tag{1}$$

Where, L - the overall distance of the traverse in kilometers, and error Δ in milimeters.

In this case, the vertical plane markings during the projected haulage drift construction will start from the existing trigonometric point T4 - Orlov kamen. This will enable the marking of point 1 at the future haulage drift entrance, followed by the demarcation of the breakthrough as per the design specifications. The vertical plane cut-through markings should be executed with a total standard deviation of

$$\Delta = \sigma_{max} = 25\sqrt{(0.49454 + 0.19120)} = 20.7\ mm \tag{2}$$

From the trigonometric point T4 - Orlov kamen to the cut-through point, a total of 11 height differences are planned to be staked out: one to determine the height of point 1 on the terrain surface, and 10 height differences during the construction of the cut-through, i.e., the haulage drift. Assuming all elevation measurements will be taken with the same standard deviations, the following can be inferred:

$$11 \cdot \sigma_{\Delta h}^2 = 20.7\ mm \tag{3}$$

regarding:

$$11 \cdot \sigma_{\Delta h}^2 = 428.29 \rightarrow \sigma_{\Delta h}^2 = 38.95 \rightarrow \sigma_{\Delta h} = \pm 6.2\ mm \tag{4}$$

The method of trigonometric leveling will be employed to stakeout height differences in accordance with the following equation:

$$\Delta h = d_k \cdot cosz \pm i \mp l \tag{5}$$

whereas:

$\boldsymbol{d_k}$ - slope distance between end points;

$\boldsymbol{z}$ - zenith angle;

$\boldsymbol{i}$ - instrument height;

$\boldsymbol{l}$ - marker height.

The mathematical operations of addition or subtraction indicated in the equation are

dependent on the vertical positioning of the marked points, whether they are situated on the floor or roof of the haulage drift.

In the *a priori* evaluation of accuracy, the principle of equal influence of the measured variables is commonly applied. This implies, in this case, each of the four measured variables when determining height differences, must have an equivalent impact on the standard deviation of the height difference from $\pm 6.2mm$. According to the law of error propagation, the error of the function (height differences determined by method of the trigonometric levelling) is:

$$\sigma_{\Delta h}^2 = k_d^2 \cdot \sigma_d^2 + k_z^2 \cdot \sigma_z^2 + k_i^2 \cdot \sigma_i^2 + k_l^2 \cdot \sigma_l^2 \tag{6}$$

whereas:
k_d, k_z, k_i, k_l - partial derivatives of the function with respect to the corresponding measured parameters;
$\sigma_d, \sigma_z, \sigma_i, \sigma_l$ - standard deviations of the measured parameters.

Assuming the principle of equal influence has been adopted, it is then:

$$k_d^2 \cdot \sigma_d^2 = k_z^2 \cdot \sigma_z^2 = k_i^2 \cdot \sigma_i^2 = k_l^2 \cdot \sigma_l^2 = k^2 \cdot \sigma^2 \tag{7}$$

follows:

$$\sigma_{\Delta h}^2 = 4k^2\sigma^2 \rightarrow 38.95 = 4k^2\sigma^2 \rightarrow k\sigma = 3.1\ mm \tag{8}$$

Partial derivatives of the function with respect to the corresponding measured parameters are:

$$k_d = \frac{\partial \Delta h}{\partial d_k} = cos\, z \tag{9a}$$

$$k_z = \frac{\partial \Delta h}{\partial z} = -d_k \cdot sin\, z \tag{9b}$$

$$k_i = \frac{\partial \Delta h}{\partial i} = \pm 1 \tag{9c}$$

$$k_l = \frac{\partial \Delta h}{\partial l} = \mp 1 \tag{9d}$$

For the first height difference between T4 and 1 values for the slope distance and zenith angle are: $d_k = 199.10\ m$ i $z = 106°11'51''$. Values of the partial derivatives are: $k_d = -0.278949$, respectively, $k_z = -191.196893\ m$.

Standard deviation of the measuring slope distance between points T4 and 1 is:

$$k_d\sigma_d = 3.1\ \text{mm} \quad \rightarrow \quad 0.278949\sigma_d = 3.1\ \text{mm} \quad \rightarrow \quad \sigma_d = \pm 11.1\ \text{mm}$$

Standard deviation of the measuring zenith angle between points T4 and 1 is:

$$k_z\sigma_z = 3.1 \text{ mm} \rightarrow 191.196893\ m \cdot \frac{\sigma_z}{\rho''} = 0.0031\ m \rightarrow \sigma_z = \pm 3.3''$$

Standard deviation of the measuring instrument height and marker during surveying between points T4 and 1 is:

$$k_i\sigma_i = k_l\sigma_l = 3.1 \text{ mm} \quad \rightarrow \quad 1 \cdot \sigma_i = 1 \cdot \sigma_l = 3.1 \text{ mm} \quad \rightarrow \quad \sigma_i = \sigma_l = \pm 3.1 \text{ mm}$$

When marking the cut-through the vertical plane, equidistant slope distances between the points were adopted, $d_k = 49.46\ m$ and zenith angle from the designed cut-through, $z = 89°10'18''$. In that case, the partial derivative values are: $k_d = +0.014457$ and $k_z = -49.454831\ m$.

Standard deviation of the measuring slope distances when marking the cut-through the vertical plane correspond to:

$$k_d\sigma_d = 3.1 \text{ mm} \quad \rightarrow \quad 0.014457\sigma_d = 3.1 \text{ mm} \quad \rightarrow \quad \sigma_d = \pm 214.4 \text{ mm}$$

Standard deviation of the measuring zenith angles when marking the cut-through the vertical plane correspond to:

$$k_z\sigma_z = 3.1 \text{ mm} \quad \rightarrow \quad 49.454831\ m \cdot \frac{\sigma_z}{\rho''} = 0.0031\ m \quad \rightarrow \quad \sigma_z = \pm 12.9''$$

5 CONCLUSION

An *a priori* accuracy assessment in measuring and marking the cut-through in the vertical plane during construction of the haulage drift on the IX horizon level of the "Grot" mine, following data has been obtained:

- The project specifications for the construction of the haulage drift does not define the acceptable error in the vertical plane. Therefore, the standard deviation of the height differences within the underground mine was adopted, which in this case is $\sigma_{max} = 20.7$ mm
- Measuring and marking height differences
- When employing the trigonometric levelling technique to determine the height differences between points T4 and 1 on the terrain surface, the length must be measured with the standard deviation $\sigma_d = \pm 11.1$ mm, zenith angle sa $\sigma_z = \pm 3.3''$, instrument height and marker height $\sigma_i = \sigma_l = \pm 3.1$ mm. These standard deviations require the lengths to be measured through three to four repeated trials with re-sighting, and the angle in the vertical plane to be assessed in two faces and by sighting with all three horizontal reticle lines.
- When employing the trigonometric technique to determine the distance between points T4 and 1 on the terrain surface, the length must be measured with the standard deviation $\sigma_d = \pm 214.4$ mm, zenith angle $\sigma_z = \pm 12.9''$, instrument height and marker height $\sigma_i = \sigma_l = \pm 3.1$ mm. These standard deviations are relatively straightforward to achieve, allowing the measurement and marking of angles to be performed using a simple method. This involves positioning in a single orientation and aligning the reticle's central thread. It is advisable that the instrument be thoroughly tested and calibrated before use. Additionally, lengths

can be measured with a standard steel tape, given the known standard deviation.

A priori accuracy assesment has shown that the measurements and markings can be achieved using the total station equipment operated by the surveying service of the "Grot" mine.

Standard devation of the height of the starting trigonometric point T4 - Orlov kamen is $\sigma_{H_{T4}} = \pm 15.0$ mm, the standard deviation of the height of the point is 11, with regard to the adopted standard deviation of the measurement and marking of the height differences is: $\sigma_{H_{11}} = \pm 25.4$ mm with the reliability of 68%. The reliability and standard deviation of the height at point 11 provide the quality execution of all future mining activities in the vertical plane at the IX horizon level of the mine.

A priori accuracy assessment was conducted using the principle of equitable influeces of all measured values on the standard deviation of height differences. The standard deviation of measurement or marking of slope distances within the projected haulage drift was evaluated from $\sigma_d = \pm 214.4$ mm is extremely large. It is reasonable to expect when measuring or marking lengths, the standard deviation would be notably low, abouth ± 50 mm, representing a relative standard deviation of $\sigma_{rel} = 1:1000$, and therefore the standard deviation of the height of point 11 will be lower than the values previously reported$\sigma_{H_{11}} = \pm 25.4$ mm.

ACKNOWLEDGMENT

The research presented in this paper was conducted with the financial support of the Ministry of Science, Technology, and Innovation of the Republic of Serbia, within the framework of funding for scientific research at the University of Belgrade, Faculty of Mining and Geology in Belgrade, under contract number 451-03- 65/2024-03/ 200126.

REFERENCES

ĐORĐEVIĆ, A. (2020) Dopunski rudarski projekat apriori ocene tačnosti proboja u vertikalnoj ravni primenom trigonometrijskog nivelmana na nivou IX horizonta u eksploatacionom polju rudnika olovo i cinka Grot (Stručni rad), Beograd: Savez inženjera i tehničara Srbije

GANIĆ, A. (2008) Račun izravnanja, Beograd: Rudarsko-geološki fakultet

SCHOFIELD W., BREACH, M. (2007) Engineering Surveying, Butterworth-Heinemann is an imprint of Elsevier, Oxford, UK

WOLF, P.R., GHILANI, C.D. (1997) Adjustment computations - Statistic and least squares in surveying and GIS, John Wiley & Sons, Inc. USA

Glavni rudarski projekat eksploatacije rude olova i cinka "Grot" - Kriva Feja. Vranje:

Rudnik olova i cinka "Grot" - Kriva Feja, Vranje, Jemadra, Despotovac, 2011. godine.

Službeni glasnik RS (1997) Pravilnik o načinu vršenja rudarskih merenja, Beograd 40/97

Tehnički rudarski projekat otkopavanja rudne zone "Istočni revir I". Vranje: Rudnik olova i cinka "Grot" - Kriva Feja, 2016. godina.

УНИВЕРЗИТЕТ У БЕОГРАДУ
РУДАРСКО-ГЕОЛОШКИ ФАКУЛТЕТ
11120 Београд 35, Ђушина 7, п.п. 35-62
Тел: (011) 3219-100, Факс: (011) 3235-539

UNIVERSITY OF BELGRADE,
FACULTY OF MINING AND GEOLOGY
Republic of Serbia, Belgrade, Djusina 7
Phone:(381 11) 3219-100, Fax:(381 11) 3235-539

РУДАРСКИ ОДСЕК

Студијски програм
РУДАРСКО ИНЖЕЊЕРСТВО

Модули:

Површинска експолатација лежишта минералних сировина
Подземна експолатација лежишта минералних сировина
Подземна градња
Рударска мерења
Механизација у рударству
Припрема минералних сировина

Студијски програм
ИНЖЕЊЕРСТВО НАФТЕ И ГАСА

Студијски програм
ИНЖЕЊЕРСТВО ЗАШТИТЕ ЖИВОТНЕ СРЕДИНЕ

Деканат

- Тел.: +381 11 3219 101
- Факс.: +381 11 3235 539
- E-mail: dekan@rgf.bg.ac.rs

Рударски одсек

- Секретар: Томашевић Александра
- Тел.: +381 11 3219 102
- E-mail: ro@rgf.bg.ac.rs

Секретар факултета

- Ђокановић Слађана
- Тел.: +381 11 3219 105
- E-mail: sladja@rgf.bg.ac.rs

Геолошки одсек

- Секретар: Јевтовић Бошко
- Тел.: +381 11 3219 103
- E-mail: gorgf@rgf.bg.ac.rs